Assessment, Analysis and Correction of MT data acquired on the Raglan property in Zones 2-3

for

Glencore Canada Corporation

Dr. Alan G. Jones, P.Geo.

20th May, 2026

Table of Contents

Executive Summary

ManoTick GeoSolutions Ltd. (MTGS) was retained by Glencore Canada Corporation to perform an independent technical assessment and analysis of magnetotelluric (MT) data acquired over Zones 2 and 3 of the Raglan property. The data were collected by Quantec Geoscience Ltd. in September 2017.

This assessment is limited to evaluation of the data characteristics, internal consistency, and suitability for geophysical interpretation and inversion. It does not constitute an audit of field procedures, nor a determination of compliance with contractual specifications or industry standards.

The field conditions for the survey were severe, and Quantec is congratulated for the successful completion of the survey yielding quality interpretable data.

The review identified several features within the dataset that may influence interpretation:

High-frequency / low-frequency (HF-LF) discrepancies
Differences between HF and LF responses are observed at multiple sites. These differences are consistent with effects associated with the magnetic field measurements; however, the underlying mechanism cannot be uniquely determined based on the available data.

Repeatability variability
Differences between repeat site measurements exceed typical expectations for MT surveys. These differences may reflect variations in acquisition conditions, sensor placement, or other operational factors.

Apparent resistivity asymmetry
A systematic high-frequency offset between RhoXY and RhoYX responses is observed. This is consistent with a potential scaling difference in electric field measurements, though alternative explanations cannot be excluded.

To facilitate continued analysis, a data conditioning approach was applied to improve internal consistency between frequency bands. This approach is mathematical and interpretive in

nature, and does not imply correction of a known physical cause. Results derived from conditioned data should therefore be interpreted within this context.

Despite the above considerations, the dataset is considered usable for regional interpretation, subject to appropriate uncertainty bounds.

1. Introduction

ManoTick GeoSolutions (MTGS) was contracted by Glencore Canada Corporation ("Glencore" or "client") to undertake assessment, analyses, and 3-D inversions of magnetotelluric data at 168 locations over Zones 2 and 3 of the Raglan deposit held by the client as shown in Figure 1.

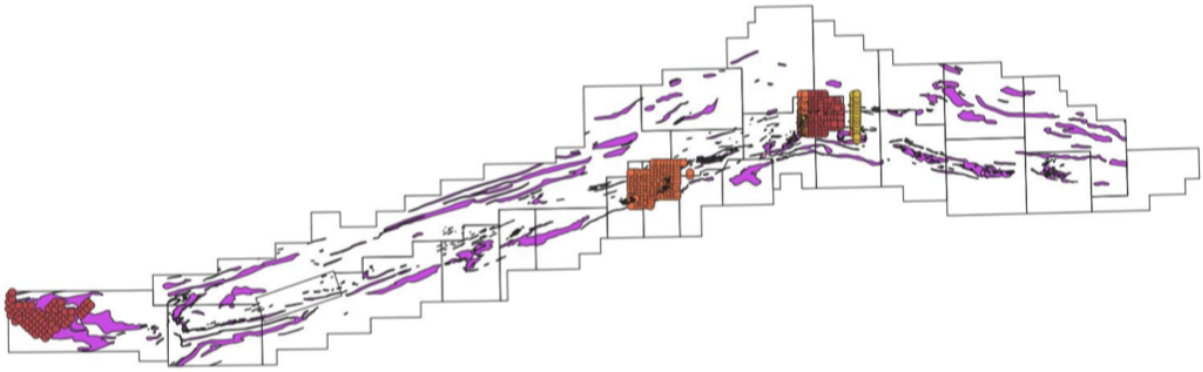

Figure 1: MT data locations (yellow and red blocks) at the Raglan Mine. Purple shows Ultramafic belts.

2. Zones 2-3 assessment

The dataset to be examined is from Zones 2-3 on the Raglan property (Figure 2 and Figure 3). The data were acquired over 17 days in September, 2017 by Quantec Geoscience Ltd. ("Quantec" or "contractor") at 168 sites, 14 of which were repeated with 10 of them having both EDI files provided, for a total of 178 data files.

Both the data and the contractor's report, CA01113S dated March 1, 2018, are publicly available at https://gq.mines.gouv.qc.ca/documents/EXAMINE/GM71363/. The report describes the data acquisition and will be referred to herein.

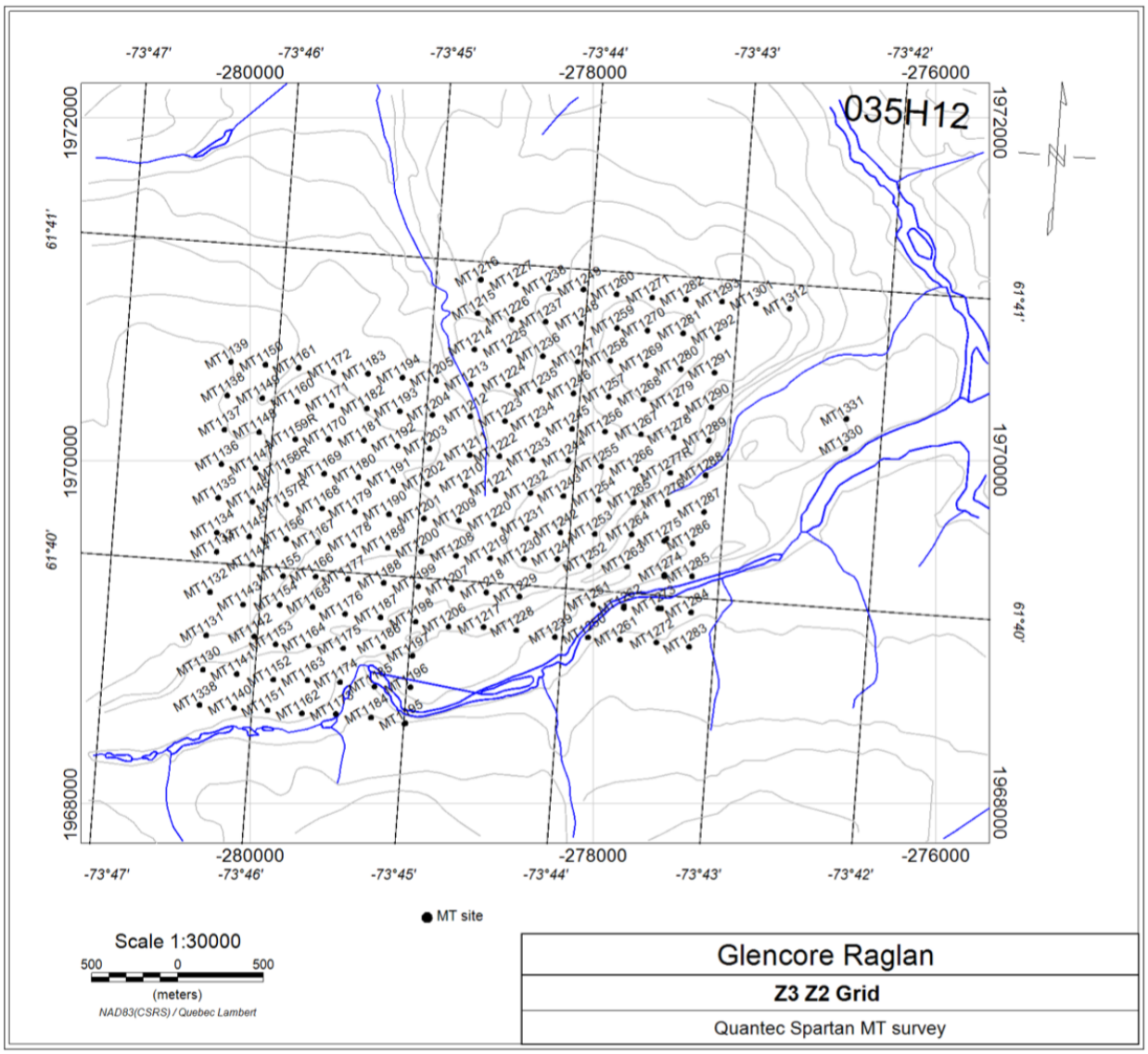

Figure 2: Locations of MT sites for the 2017 Quantec survey in zones Z3 and Z2.

Figure 3: 2017 Quantec MT sites on Zones 2-3

3. 2017 Survey

3.1. Field conditions

The field conditions in the survey area were severe; the ground consists of broken rock with little to no vegetation and soil (Figure 4). This makes burying the coils to protect them from high winds a difficult task. The other related issue is contact resistance of the electrodes, which is also negatively impacted by ground conditions.

Quantec report the following adverse field conditions:

1. *Winter conditions during the late September / early October survey period*
2. *Frozen ground*
3. *High impedance geomorphology*
4. *Difficulty with navigation and alignment due to proximity to the north magnetic pole*
5. *Significant and unexpected environmental noise*
6. *Deadband and signal issues due to daytime measurement*

Quantec is congratulated for acquiring the data they did in this very challenging environment.

Figure 4: Typical site in Raglan project area (provided by Daryl Ball, 9th April, 2026).

3.2. Recorders

All data acquired by Quantec in 2017 used their Spartan MT systems. These are 6-channel seismic recorders (Ref Tek) to which Quantec attaches MT sensors. Stated input impedance of the Ref Tek boxes is very high at 100 MΩ. Input impedance becomes important when contact resistance is high, as discussed below.

The least significant bit (lsb) for the Ref Tek 160 recorders with a gain of 1 is stated as 3.81 μV. The Phoenix systems have a maximum output voltage of ± 5 V and a dynamic range of "better than 130 dB", giving an lsb for a gain of 1 less than 3 μV. So the two systems are comparable in their sensitivity.

Typical gain settings for the 2017 Survey are not given, but at many sites there is a comment that "Gains adjusted to 4" or "Gains reduced to 4" or "Gains dropped to 4". A gain of 4 means a least significant bit (lsb) of 954 nV. Presumably the gain is typically set to 8 or 16, so lsb's of 477 nV or 238 nV.

There is the Observation (E.3) noted in the publicly-available contractor's report, CA01113S, that "*Numerous overscales in all channels. May reduce gains in next days.*" MTGS was unable to determine from the deliverables whether overscales actually clipped the recorded time series; confirmation by the contractor would resolve this question.

3.3. Magnetic sensors

Two types of magnetic sensors were used on this 2017 survey; namely low frequency (LF) coils from Phoenix (MTC-50) and high frequency (HF) coils from Geometrics (G100K). Comparison of their sensor noise levels is shown in Figure 5.

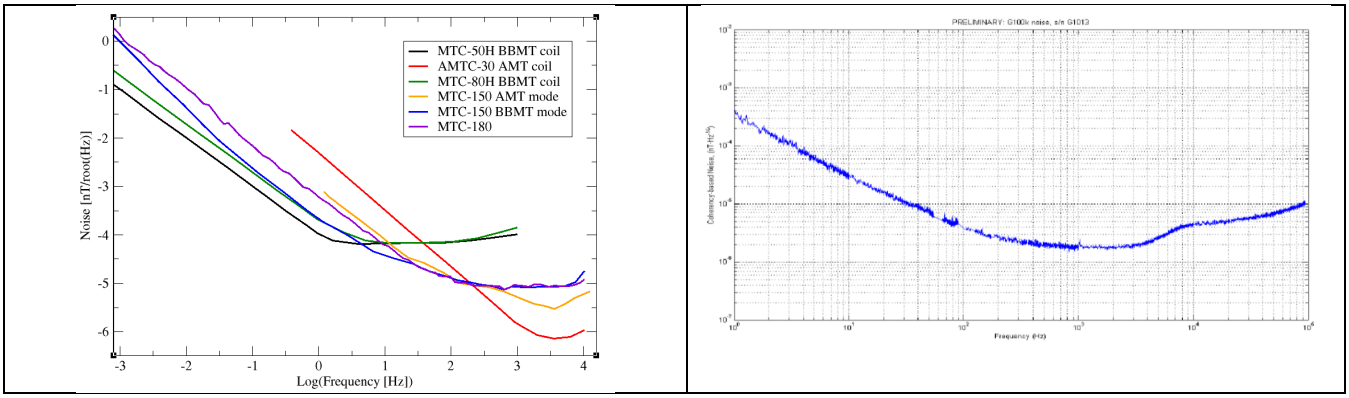

Figure 5: Coil sensor noise levels. Left: Phoenix sensors (MTC-50 in black). Right: Geometrisc G100K sensor.

3.3.1. *AMT deadband*

The sensitivity of the available coils is important for assessing the likely quality of the time series, especially in the AMT deadband [(1)]. Tests by *Garcia and Jones* [2002] analysing data acquired with the Phoenix AMTC-30 sensors showed that typically signal was estimated to be one to two orders of magnitude less than sensor noise, at about $5x10^{-8}$ nT/sqrt(Hz) at 1 kHz (based on the electric field amplitudes), during the daytime.

For the 2017 survey, 2 out of every 3 sites were acquired during the daytime. Daytime sites had ~2 h of data (AMT impedance estimates from 10 kHz – 1 Hz), and overnight sites ~12 h of data (AMT/BBMT estimates from 10 kHz – 0.001 Hz). One can expect poorer AMT deadband estimates at those daytime sites.

[1] The AMT deadband is the band of frequencies from around 5 kHz to around 800 Hz, and is caused by a natural low in the signal spectrum from the two different sources of lightning energy. High frequency cloud-to-ground energy is at frequencies from 5 kHz and above, and low frequency cloud-to-ionosphere energy is from around 800 Hz to the Schumann resonance (7.8 Hz).

Figure 4-2 in the Logistics Report CA01113S (Rev 1), repeated here as Figure 6, plots the daytime sites in blue and overnight sites in red.

Acquisition start and end times are not reported in either the 2018 Logistics Report or the 2018 EDI files; including these in the EDI files as metadata would have been beneficial.

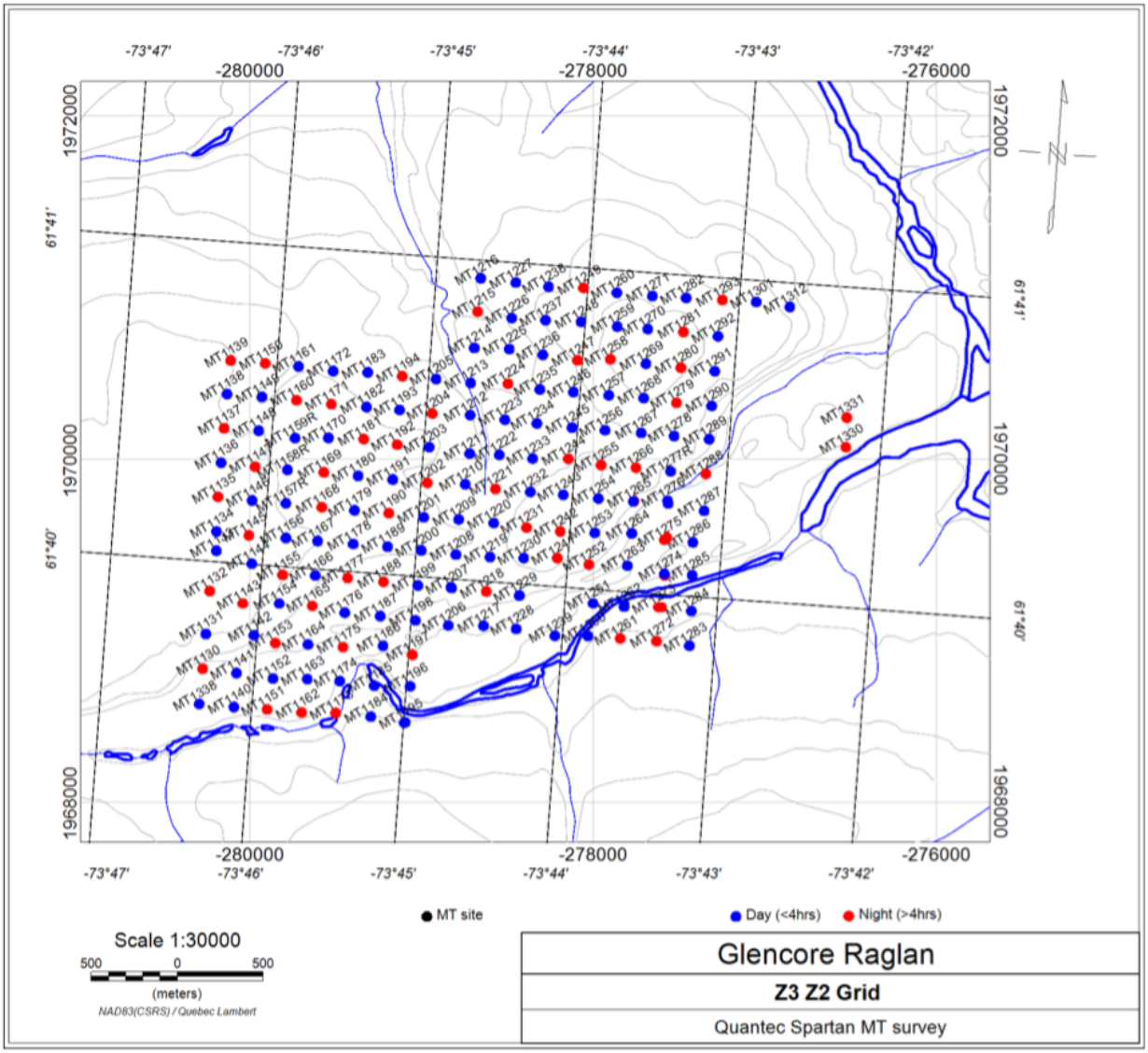

Figure 6: Day-time and night-time sites. Figure 4-2 in the 2017 Logistics Report CA01113S (Rev 1).

3.4. Electric field acquisition

Metal-plate electrodes were used for the survey, which is consistent with the elevated noise observed at low frequencies below 10 Hz. It should be noted that the field conditions were severe for acquiring e-field data, as the ground consists of broken rock with little to no vegetation and soil.

3.4.1. *Contact impedance*

The issue with contact impedance is the circuit between the electrodes, the ground, and the receiver, such that if the contact impedance approaches the input impedance of the receiver, then there are *RL* inductive effects on the data due to attenuation (and phase advances) of the electric field amplitudes at high frequencies. The most egregious example in the literature is that from a site on Baffin Island acquired by *Evans et al.* [2005] with a measured contact resistance of 2 MΩ. No data at high frequencies >5 Hz (periods <0.2 s) are usable (Figure 7).

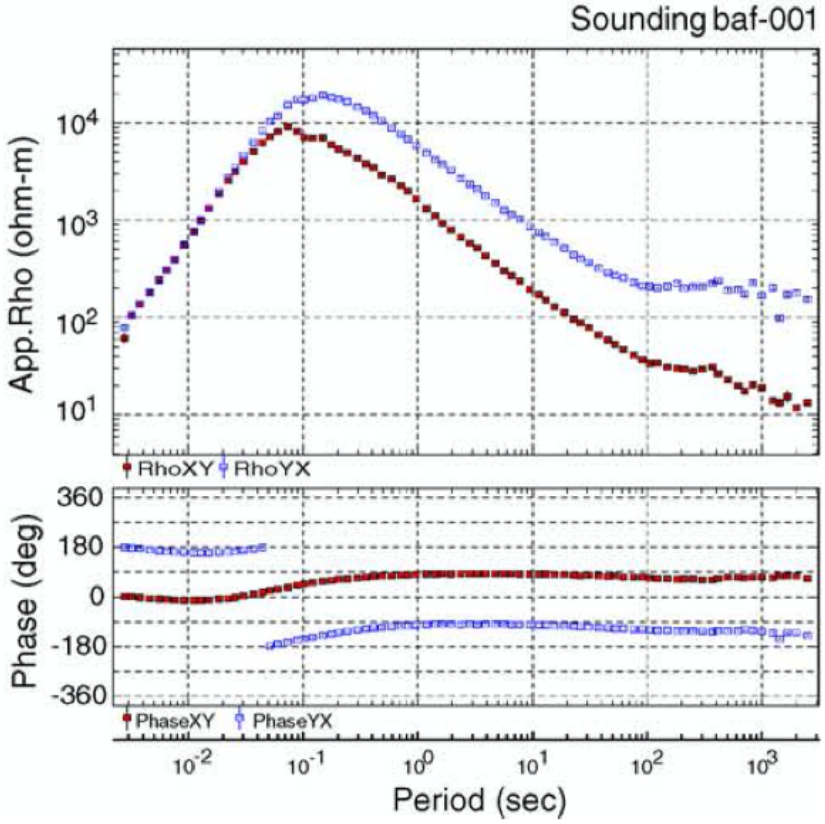

Figure 7: Site baf001 of Evans et al. *[2005] .*

Contact impedance at a number of sites on the 2017 survey is notably elevated, with values in excess of 50,000 Ω (dark grey in Figure 8, reproduced from Fig. 4-4 in Logistics Report), and even in excess of 100,000 Ω (black in Figure 8).

➔ AMT data at sites with high contact resistance are likely to show elevated noise and may be subject to some bias.

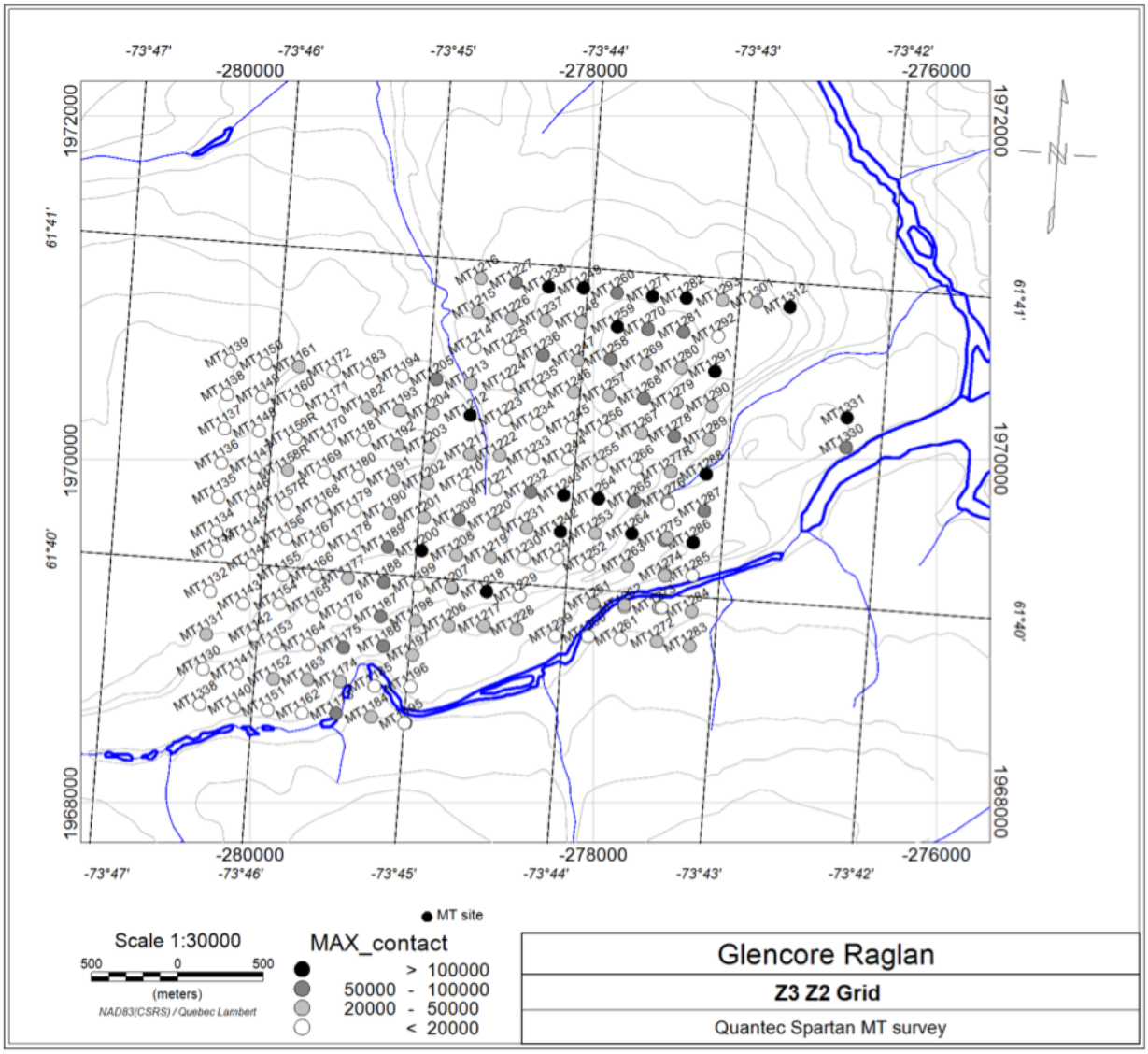

Figure 8: Distribution of the maximum (one value per site) of the contact impedance measured for sites on grids Z2-Z3. Fig. 4-4 in 2017 Logistics Report CA01113S (Rev 1).

This issue was recognised by the contractor – see below in Section "Comments on Measured Data".

In the site description, for example for site MT1033 is written "*app-res and phase pull on the HF due to very large contact impedance- valid data here is may be only for f<1khz; I would recommend to repeat the site*."

Examples of the problem are shown for sites MT1331 and MT0820R in their Fig. 4-6, reproduced here in Figure 9.

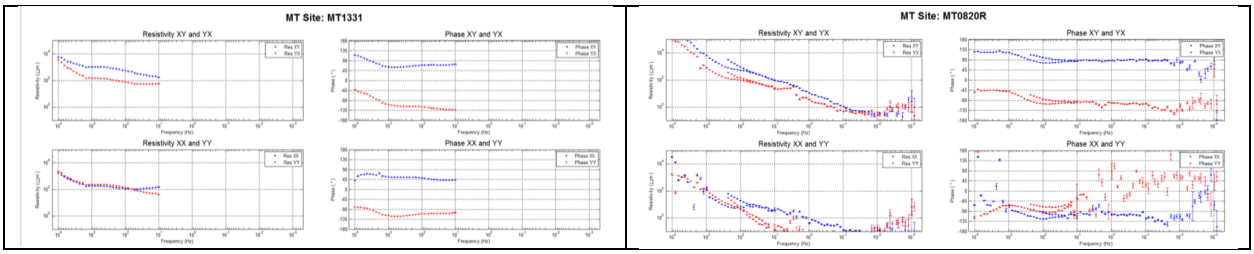

Figure 9: Examples of pull-up on the MT sounding curves due to high impedance contact (sites 1331 and 0820R). Taken from 2017 Logistics Report CA01113S, Fig. 4-6.

➔ Including the measured contact resistances in the report and as EDI metadata would assist downstream users.

3.4.2. *Remote reference*

The remote reference location was at UTM location 550803 E, 6863541 N (NAD83 – 18NH).

3.5. Quantec Processing

As per the contractor's Logistics Report CA01113S (GM71363, Quebec EXAMINE):

Quantec proprietary QuickLay software (ver.5.1.8.2) coupled with Egbert MT processing code:

1) Coherent noise rejection using remote reference

2) Proprietary digital filtering (scrubbing)

3) Coherency sorting

4) Impedance estimate stacking

Default configuration set to output 12pts per decade;

Data processed to output X at 00° True.

3.6. Contractor comments on Measured Data

The contractor makes comments about the Measured Data, and they are reproduced below for completeness of this report (from Quantec Geoscience Ltd., Logistics Report CA01113S (GM71363, Quebec EXAMINE)) under fair dealing for purposes of research and review.

Comments on Measured Data

The magnetotelluric survey was planned so data can be measured during the day and overnight. Each team tried whenever possible to measure with each data logger two AMT sites during the day (~2hrs reading; processing output from 10kHz to 1Hz) and one MT site overnight (~10-12 hrs reading; processing output from 10kHz to 0.001Hz). The distribution of the sites with Day-

time and Night-time acquisition is illustrated on Figure 4-2 for grids Z3-Z2 and on Figure 4-3 for grids Z58-ZT.

The first Spartan-MT sites surveyed were located over pre-existing MT-TITAN24 lines on the grids Z58-ZT so a comparison of data can be completed. A site to site comparison of the sounding plots was presented to Glencore representative, and a copy of the document is provided in APPENDIX F Comparison of Spartan and Titan24 MT data. From the review, it was clear that the 2017 MT data are presenting similar characteristics to those measured previously with the TITAN24 system.

Some extra processing was completed following the loss of some time series data from the remote site (data recorded on September 15th). The objective was to demonstrate to Glencore representatives that a local site can be used as a remote site in the processing. This could be helpful in case other issues arise at the remote site. Results of the processing was presented to Glencore representatives on September the 21st. A copy of the document is presented in APPENDIX G – Memo #1 (2017/09/21): Comparison of data processed using the remote and Cross-Reference (i.e., site as remote). The result of the test shows that effectively a MT site could be used as the remote site if necessary.

A few important notes regarding the overall data quality:

High Frequency (HF) Dead Band

MT sites measured during the day-time are generally presenting strong noise in the HF-dead band due to weak signal for those frequencies during day-time. Review of the data was completed and most of the observed noise has been removed on the 'edited' EDI files.

Contact Impedance:

We noticed after the deployment of the first sites (especially on the Z3-Z2 area) that it will be difficult to obtain good contact for the electrodes as the ground is very rocky with little or no soil to bury the plates (i.e., electrodes). The crew were carrying extra mud and water for the electrodes for use in these situations. This did help to reduce the impedance contact for most of the sites; however, for some sites, the contact impedance remained extremely high (over 100,000 ohms; maximum measured is 900,000 ohms). Such high (extreme) contact impedances impact the data by presenting an artificial 'pull-up' on the sounding curve at high frequency (see example on Figure 4-6). To better characterise this 'noise', and to provide a future reference on the quality of the measured data, maps of the contact impedance at these sites have then been created. Figure 4-4 and Figure 4-5 present the maximum measured contact impedance for each site classified into one of four groups; two groups (dark grey and black) are mapping measured values greater than 50,000 ohms over the survey area. The group represented by the black dots is mapping the extreme values (>100,000 ohms) and should map 'critical' sites.

HF/LF Band shift

The critical point over the acquisition and processing of the data is the band shift between the high-frequency and the low-frequency measured data. This band shift appears occasionally on the apparent resistivity XY or YX data (see example on Figure 4-7), but may occur only on the XX and YY data (see example on Figure 4-8). The later may then introduce a band shift on the XY and YX sounding after rotation of the data (see example on Figure 4-8). This will occur because the data of the two modes XX and YY are of the same 'amplitude' as the XY and YX modes, that are observed for 3D geology and/or potentially strong distortion of the MT data. The band shift in the XX and YY modes will be then transferred to the XY-YX sounding curves after rotation of the data. This band shift (either in the XY-YX or in the XX-YY modes) may introduce a 'false' variation on the sounding curves that could or will impact the result of a 2D or 3D inversion by potentially introducing 'false' anomalies.

The following comments are related to this band shift. Quantec uses two sets of coils for the MT acquisition, one set for the HF and one for the LF. As the electric fields for the HF and LF are measured using the same dipoles, the band shift is assumed to be from the magnetic coil data, possibly due to misalignment or 'local' distortion (see below) of the coils. The field crew did everything possible to align the sensors correctly, however:

1. There was some high-wind during the survey acquisition; the coils couldn't be dug into the ground as normal due to the very rocky/no soil conditions. This could result in some motion or disturbance of the magnetic sensors after site was set up;

2. The amplitude of the magnetic field in the survey area (see regional magnetic field over the Raglan area, see Figure 4-1) is very high and that had an un-expected impact on the field acquisition. The compasses were strongly affected, and the crew reported difficulties to obtain a proper measurement of the azimuth for the sensors ("north arrow of the compasses spinning").

3. The crew also noticed some magnetic rocks on the ground and one cannot remove the possibility that the measurements from one coil at a site (either the HF or LF, X or Y) can be 'locally' affected by one high-magnetic rock located below or just next of the coil (i.e. acting like a magnet distorting of the magnetic field on that coil).

The MT data have been reviewed and editing was focused to minimize the aforementioned effects. Unfortunately, this resulted in only the HF part of the sounding at the MT sites being kept, i.e. data from 10k to 10hz (HF frequencies processed – limit of 10Hz is from the magnetic sensors).

Following the observation at several sites of the band shift and therefore the loss of LF data for these sites (i.e. the data of the site is edited to keep only the HF part of the frequencies), we have evaluated the impact on the data and on the depth of resolution for a 10kHz-10Hz limited

frequency band at sites. The analysis has been presented to Glencore and copy of the document is provided as APPENDIX H Memo #2 (2017/09/24): Frequency of the MT sites: 10Hz versus 1hz.

On MTGS's reading of the data, the proposed mechanisms would be expected to produce matching shifts in XY and YX (which share the same coils) and in XX and YY. The data examined here do not appear to display this matching pattern. The contractor may hold additional information that bears on this observation.

4. Inspection of EDI files

Three EDI files for each site were provided by the client for assessment. The folders are named and contain:

1. "*00spectra*": These are EDI files in SPECTRA format.
2. "*01sp2z_edit*": These are EDI files in IMPEDANCE format that have been "edited", which means have had some data removed at some frequencies.
3. "*02imp_interpolated*": These are EDI files also in IMPEDANCE format that have been smoothed through applying an undescribed interpolation routine used in CGG's Geotools package.

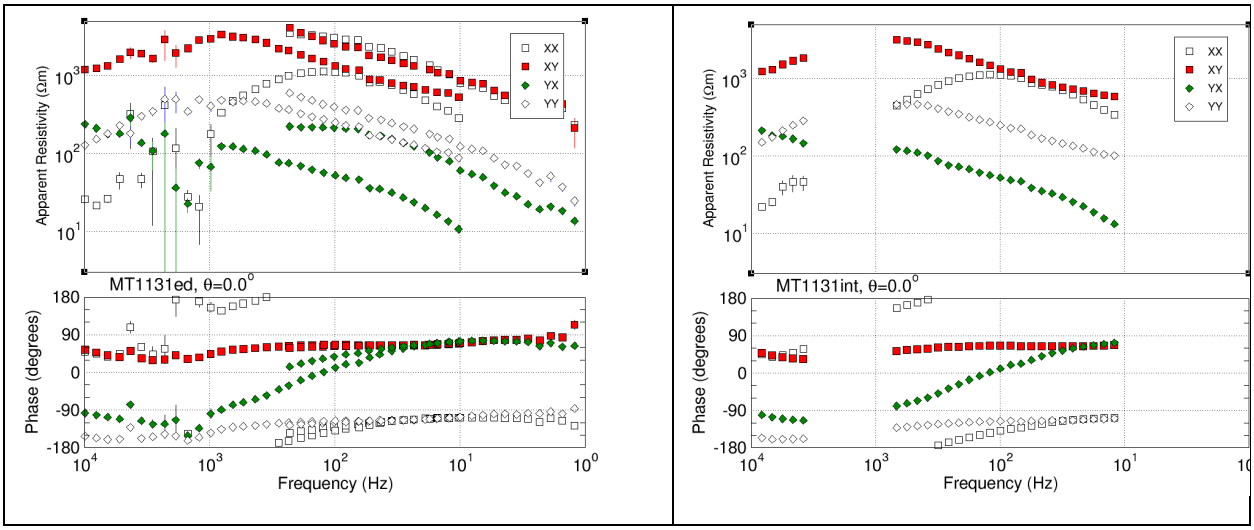

Figure 10: Edited (left) and Interpolated (right) data for site MT1131.

An example of the differences between the three sets of estimates is site MT1131 shown in (Figure 10). The "edited" version of MT1131 in folder *01sp2z_edit* looks exactly like the original (Figure 10, left). The "interpolated" version in folder *02imp_interpolated* has had all of the LF data removed, and the HF data in the AMT deadband removed (Figure 10, right).

The INFO block in these EDI files does not include any metadata. Here is the INFO block from 2018 file MT0844.edi in folder *00spectra*:

```
>INFO   MAXLINES=1000

QGLN001: Spectra are in RH-positive down co-ordinate system

DATUM: NAD83(CSRS98)  (1m) Canada
```

The INFO block in the *01sp2z_edit* folder file and the *02imp_interpolated* folder file contains still less information:

```
>INFO

MAXINFO=2
```

5. Band shift

Most sites showed a significant difference in RhoA estimates between the HF and LF estimates, which used Geometrics G100K and Phoenix MTC-50 coils respectively.

One example of this band shift is shown for site MT1131 (Figure 11, note: the response estimates at this site only go down to 1 Hz). The band shift is in all four components. The separation between the two branches of the RhoXY curves (red squares) is visually the same as the separation between the two branches of the RhoYY curves (unfilled diamonds), about 0.25 of a decade. Similarly, the larger separation between the two branches of the RhoYX curves (green diamonds) is visually the same as the separation between the two branches of the RhoXX curves (unfilled diamonds), about 0.75 of a decade.

Inspecting the phases, there is very good agreement at frequencies below about 30 Hz, but at higher frequencies there is some discrepancy in the PhaYX and PhaXX phases (Hx coils), presumably because of the different coil responses.

Quantec proposes several candidate explanations for the band shift, but none fully accounts for the observed signature. For instance, a rotation error in the coils would cause the LF RhoA curves to move in opposite directions. If RhoXY-LF were greater than RhoXY-HF then RhoYX-LF would be less than RhoYX-HF.

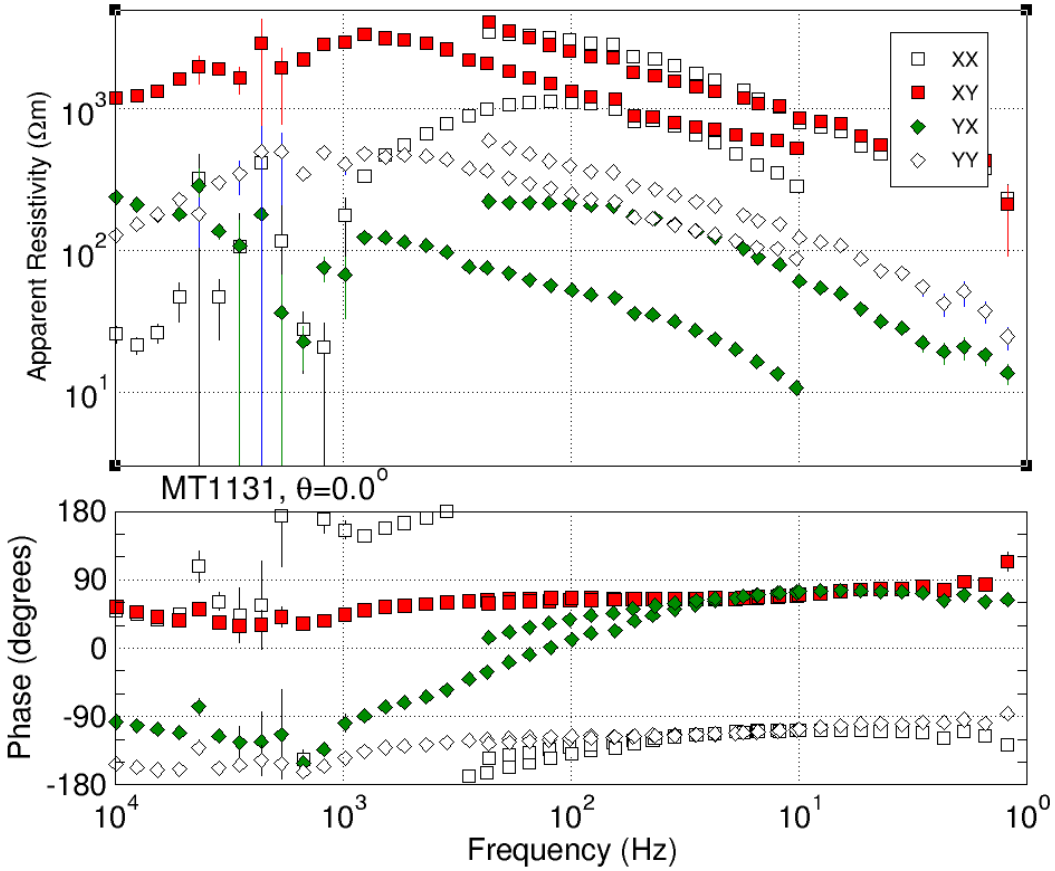

Figure 11: Site MT1131 exhibiting band shift in all components.

Another example is the data for site MT1232 (Figure 12, left), which shows band shift for the right column RhoXY and RhoYY components. (Note: the response estimates at this site also only go down to 1 Hz.) One problem with this site is that the RhoXX and RhoYX HF and LF curves line up, but the separation of the RhoXY HF and LF curves is not mirrored in the separation of the RhoYY HF and LF curves. Indeed, it is of opposite sign – the HF RhoXY curve needs to be increased to match the LF RhoXY curve, but the HF RhoYY curve needs to be significantly decreased, by more than an order of magnitude, to match the LF RhoYY curve.

Other sites show this band shift to greater or lesser extent. The daytime sites seem to have this problem more than the overnight sites, but even some overnight sites have this band shift, such as site MT1272 (see Figure 12, right). Even though the effect is visually more minor at many sites, even a shift of that shown for site MT1272 is 18% in (XY,YY) and 15% in (XX,YX), which will result in depth estimation errors of almost 10% (depth bias goes as the square root of the static shift).

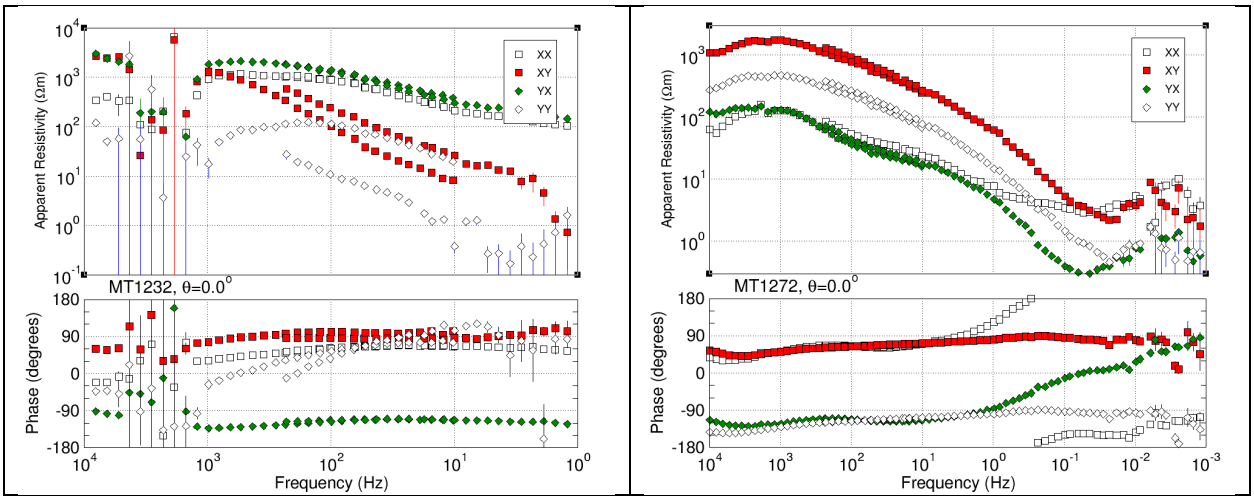

Figure 12: Left: Site MT1232 exhibiting band shift in the Hy components, RhoXY and RhoYY. Right: Overnight site MT1272 exhibiting band shift in all four components.

The HF and LF data are merged into one file, so to correct the problem formally requires a code that will sift through the data and separate the HF and LF estimates, and apply a shift factor to the LF estimates so that they mesh with the HF estimates.

To correct for this band shift requires separating the HF and LF estimates, this can be done by

1) EITHER determining the average geometric factors between two pairs of them, (XX,YX) and (XY,YY), at overlapping frequencies using a robust statistical approach,
2) OR using the geometric factors for the first or last two or three overlapping values,

then applying that factor to the LF estimates and re-merging them.

Fortunately, the sequence of frequencies for HF and LF is identical for all of the files, and are:

HF Freqs: 1-19, 21, 23, 26, 28, 29, 32, 34, 35, 37, 39, 41, 43, 45, 47, 49

LF Freqs: 20, 22, 24, 25, 27, 30, 31, 33, 36, 38, 40, 42, 44, 46, 48, 50 → ■

where n is the total number of frequencies in the file. n is typically 61 for the daytime sites and 95 for the overnight sites, although not for all sites. Note that the sequences are not alternating in the overlap band.

Separating the LF from HF data for site MT1131, we can more clearly see the band shift.

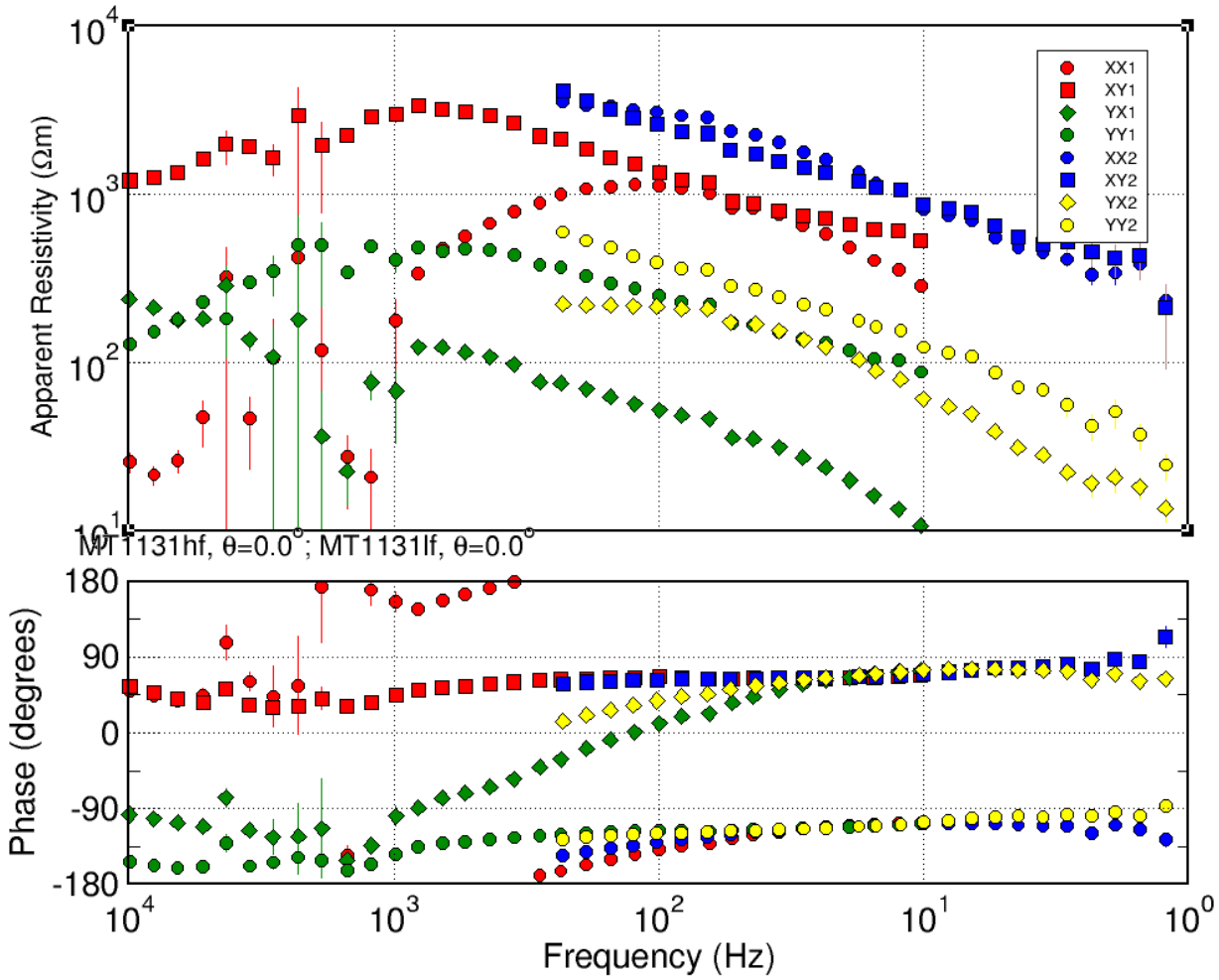

Figure 13: Site MT1131 plotted in terms of HF ("1") and LF ("2") estimates.

5.1. Rotation of Z

We can examine the rotation of **Z** for two neighbouring frequencies for the data from site MT1131. Frequency numbers 19 and 20 are selected:

Table 1: Impedance estimates from site MT1131 at frequencies 19 and 20.

Freq no.	Freq. (Hz)	Zxx	Zxy	Zyx	Zyy
HF 19	234.40	-1.3045, 0.3757	0.8888, 1.7620	0.3180, -0.1953	-0.4181, -0.7077
LF 20	230.47	-2.0791, -1.4469	1.4203, 2.3265	0.6186, 0.1476	-0.06158, -0.83819

Rotating the two impedance tensors through 360° and plotting |Zxy| and |Zxx| shows the significant differences between the two HF and LF impedance estimates at neighbouring frequencies. There is not only a very large amplitude difference, there is also a major phase difference, as expressed by the different maxima and minima directions.

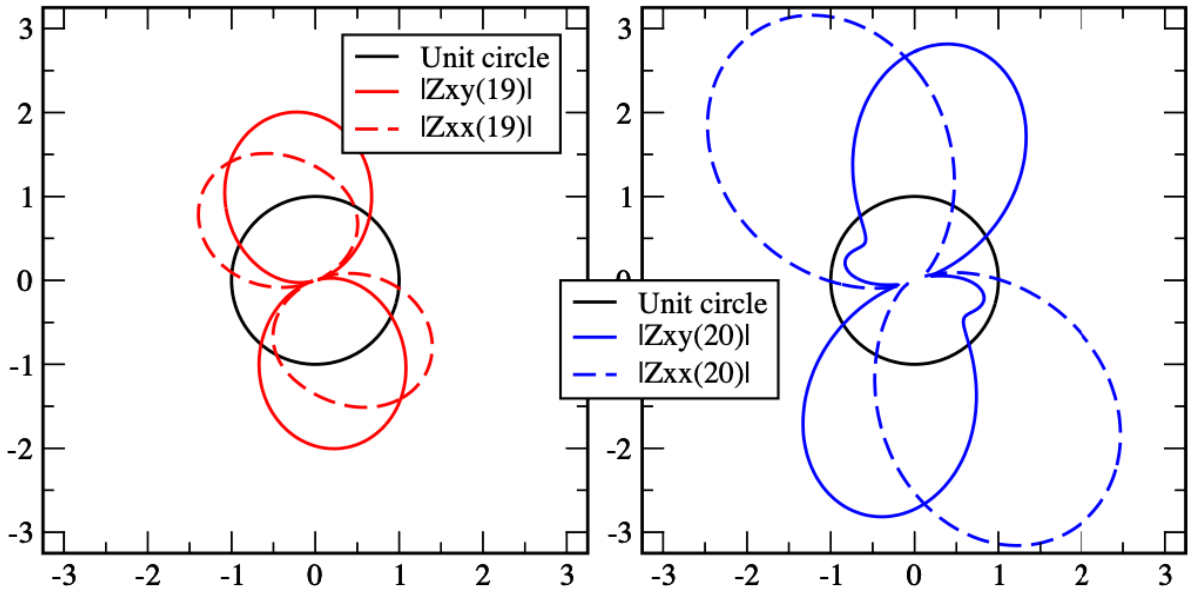

Figure 14: Rotation of |Zxy| and |Zxx| around 360° for HF frequency 234.40 Hz (freq 19) and LF frequency 230.47 Hz (freq 20).

5.2. Apparent resistivity curves not parallel

For some sites, the HF and LF RhoA curves are not parallel in the overlap range of frequencies. An example is shown in Figure 15 for site MT1173 for the RhoYX component.

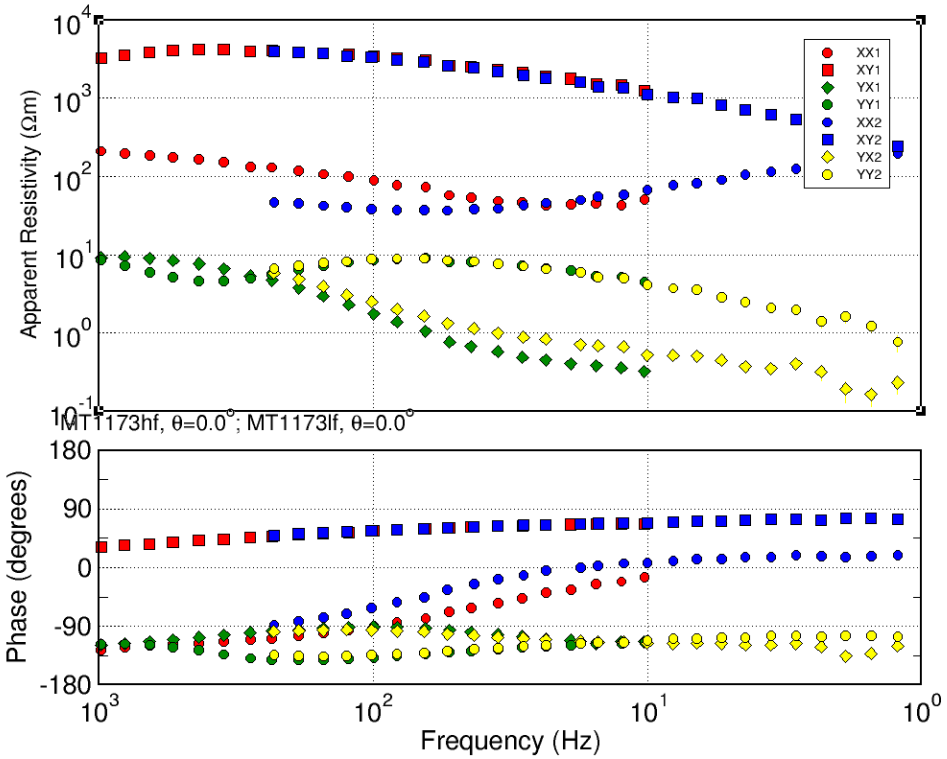

Figure 15: Site MT1173 exhibiting non-parallel HF ("1", green diamonds) and LF ("2", yellow diamonds) RhoYX curves. (Data for this site only plotted in the overlap decades of 1 kHz – 1 Hz).

The cause of this behaviour is not yet established. The most consistent explanation is a calibration issue affecting one of the Hx coils used. A coil-by-site listing is not provided in the deliverables, which prevents cross-referencing across sites to determine whether the issue is generic.

Given this issue, taking the averages does not make sense to derive the multiplicative correction factors.

5.3. Phases not in agreement

Of arguably more concern than the amplitude displacements between the HF and LF estimates, which can be treated as a static shift problem, is the significant differences in phases. Examples are shown already above for sites MT1131 (Figure 11, Figure 13) and MT1173 (Figure 15), and also below for site MT1162 in Figure 16. These sites show different effects – for MT1131 the HF and LF PhaYX phases come into agreement at the lowest overlap frequency, but for MT1162 they are never in agreement, but show the least disagreement at the highest overlap frequency. For site MT1173 the PhaXY HF (red circles) and LF (blue circles) are parallel and offset from each other.

MTGS has extensive operational experience with Phoenix MTC-50 coils, and accordingly the LF estimates are taken as the more reliable of the two branches at this site. The HF PhaYX estimates are noted to converge towards −90°, which is unusual and would warrant further investigation.

On the basis of the analyses presented above, the LF phases are taken as the more reliable estimates at this site, and the merge is performed at the first LF frequency (230.47 Hz). The same approach is applied to similar sites.

Another site with strange amplitude and phase response for one element is site MT1143.

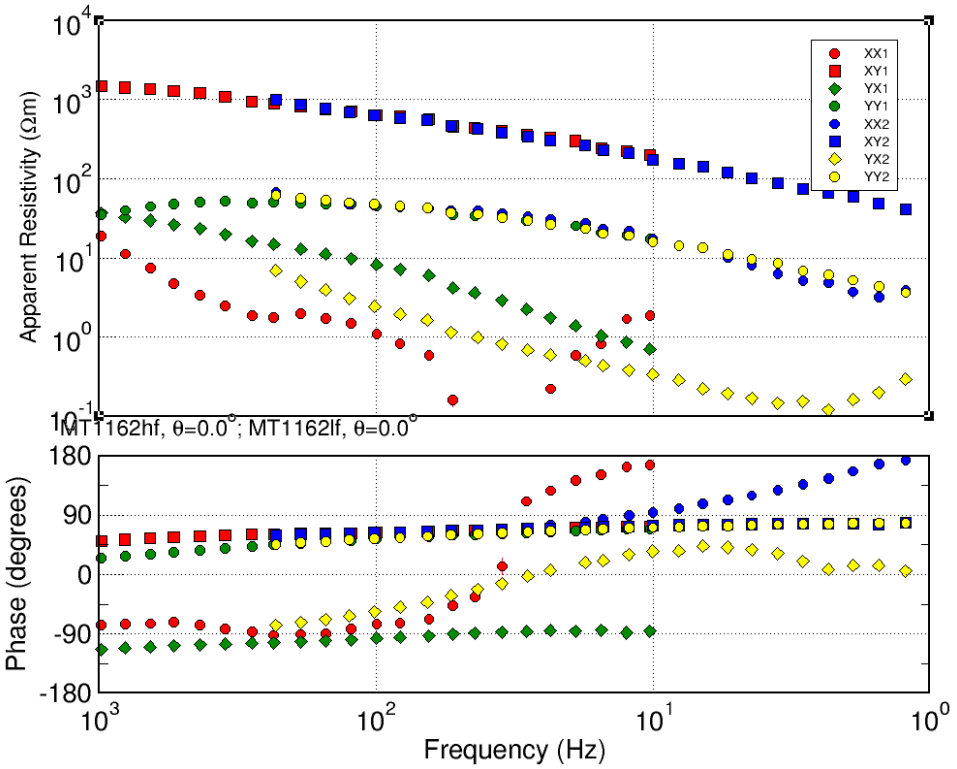

Figure 16: MT1162 data showing phase mismatch for PhaYX (green diamonds are HF and yellow diamonds are LF).

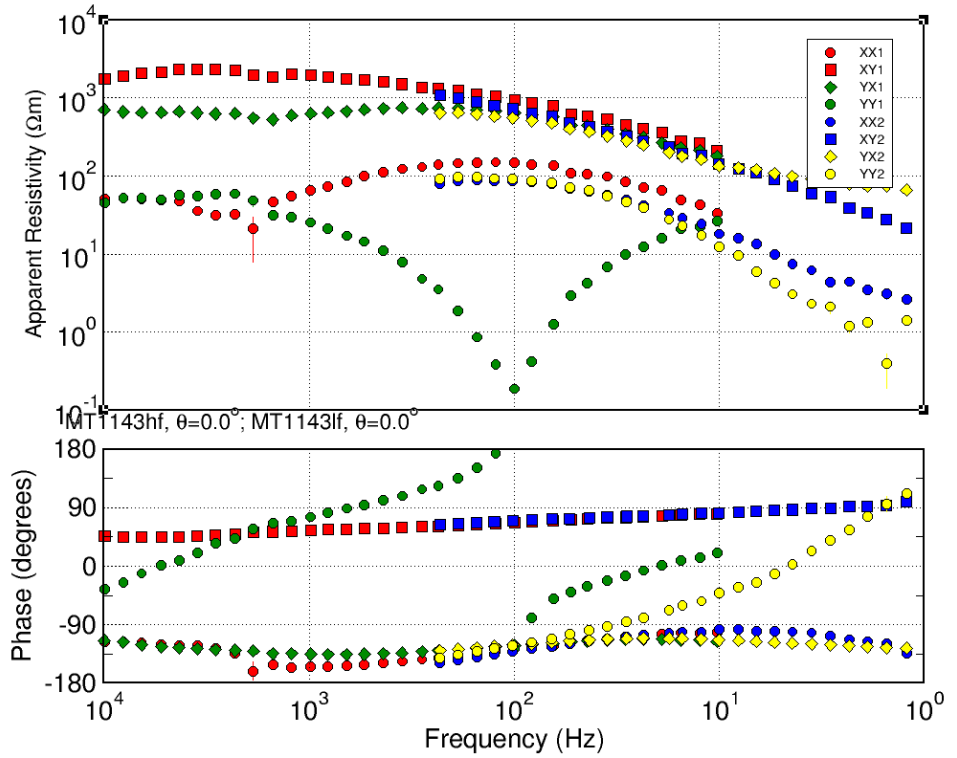

Figure 17: MT1143 data showing RhoYY and PhaYY mismatch for PhaYX (green circles are HF and yellow circles are LF).

6. First correction approach

Given the above issues, one correction approach to attempt was:

1) to derive the shift factors between the HF and LF RhoA curves in pairs, (XX, YX) for the Hx coil, (XY, YY) for the Hy coil, based on the first two of three overlap points, i.e., frequency pairs 19 (HF 234.40 Hz) & 20 (LF 230.47 Hz), 21 (HF 187.52 Hz) & 22 (LF 187.50 Hz), and 23 (HF 152.36 Hz) & 24 (LF 152.34 Hz).
2) Take the XY shift factor for (XY and YY) and the YX shift factor for (XX and YX), and apply those shift factors to the HIGH FREQUENCY RhoA data for frequencies 1 – 19.
3) Discard the HF data at the 15 lower freqs (21, 23, 26, 28, 29, 32, 34, 35, 37, 39, 41, 43, 45, 47, 49)
4) Match those shifted HF data from freqs 1-19 to the LF data from 20-n.

Note the implicit assumption being made with this approach is that the correct RhoA levels, and correct Phases, are from the Phoenix coils.

6.1. Examples of application of RhoA shifting

A code was written to perform the four steps outlined above. Examples of its application for the above considered sites are shown in Figure 18.

However, although the XY and YX curves now line up correctly, the diagonal curves do not line up correctly at three of them. The mismatch for YX should be the same as for XX as both use the Hx coil, and the mismatch for XY should be the same as for YY as both use the Hy coil. These data were all acquired at zero azimuth, and were processed and delivered at zero azimuth, so there should not be any rotational mixing effects.

The residual mismatch is difficult to reconcile and indicates that this particular correction method is not the right approach for these data.

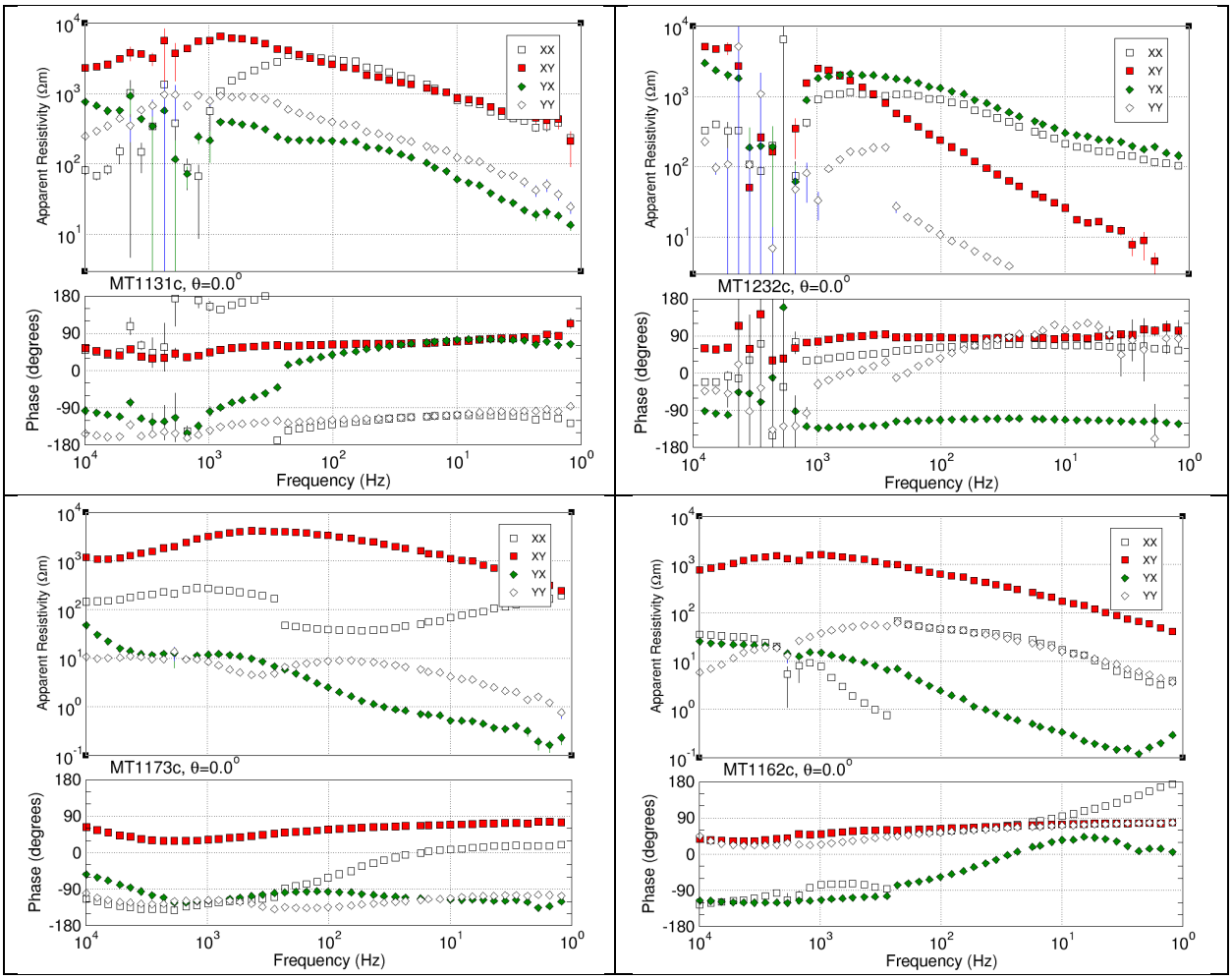

Figure 18: Application of the correction code to sites MT1131 (top left), MT1232 (top right), MT1173 (bottom left) and MT1162 (bottom right).

6.2. Impedance plots

Greater clarity could come from considering impedance plots rather than RhoA/Pha plots.

Also, the impedances differences between the LF and HF estimates at 16 pairs of overlap frequencies can be analysed to try to determine the root cause of the Band Shift. These differences are scaled by:

1. 1/freq,
2. 1/sqrt(freq),
3. 1/|HF|, i.e., normalize by the magnitude of the HF data at the HF freq and
4. 1/|LF|, i.e., normalize by the magnitude of the LF data at the LF freq.

6.2.1. *Site MT1162*

The impedances from 1 kHz to 1 Hz are plotted in Figure 19 for the four MT tensor elements in an Argand diagram (Real part on the abscissa, Imaginary part on the ordinate). Black points are the HF ones and red points are the LF ones, and the blue lines connect neighbouring HF-LF pairs.

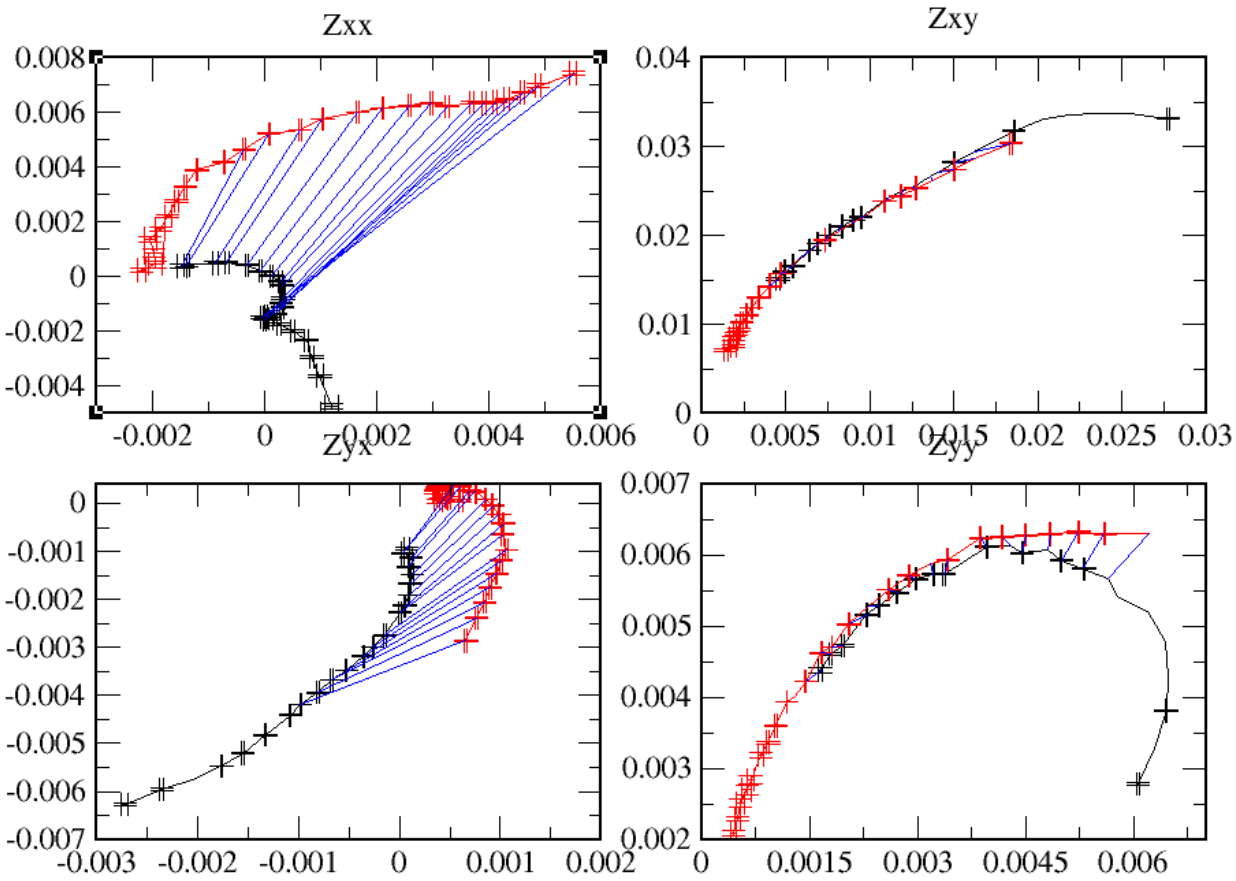

Figure 19: Data from 1 kHz to 1 Hz for site MT1162 plotted in terms of impedances on an Argand diagram. HF in black and LF in red. Overlap points are joined by blue lines.

For this site the XY and YY (right column) HF and LF data match within statistical errors, apart from the overlap at the first few freqs in YY. However, the HF and LF XX and YX differences (left column) are obvious. The issue is clearly not a simple amplitude effect, but is also a phase effect. An amplitude-only effect would not shift the data out of its quadrant.

If we plot the impedance differences for the 16 pairs of frequencies, we see that there clearly is an apparent linear frequency dependence for the differences (to within errors) (Figure 20, top right). Scaling these differences by dividing by frequency, we see that most of them become flat, certainly in the range 250 Hz to around 50 Hz (Figure 20, middle left). Note that the real and imaginary parts are different for each impedance element.

However, this apparent linear dependence may come from the data themselves. We scale the data instead not by 1/*f* but by one over the magnitude of the HF estimates (Figure 20, bottom left) and also by one over the magnitude of the LF estimates (Figure 20, bottom right).

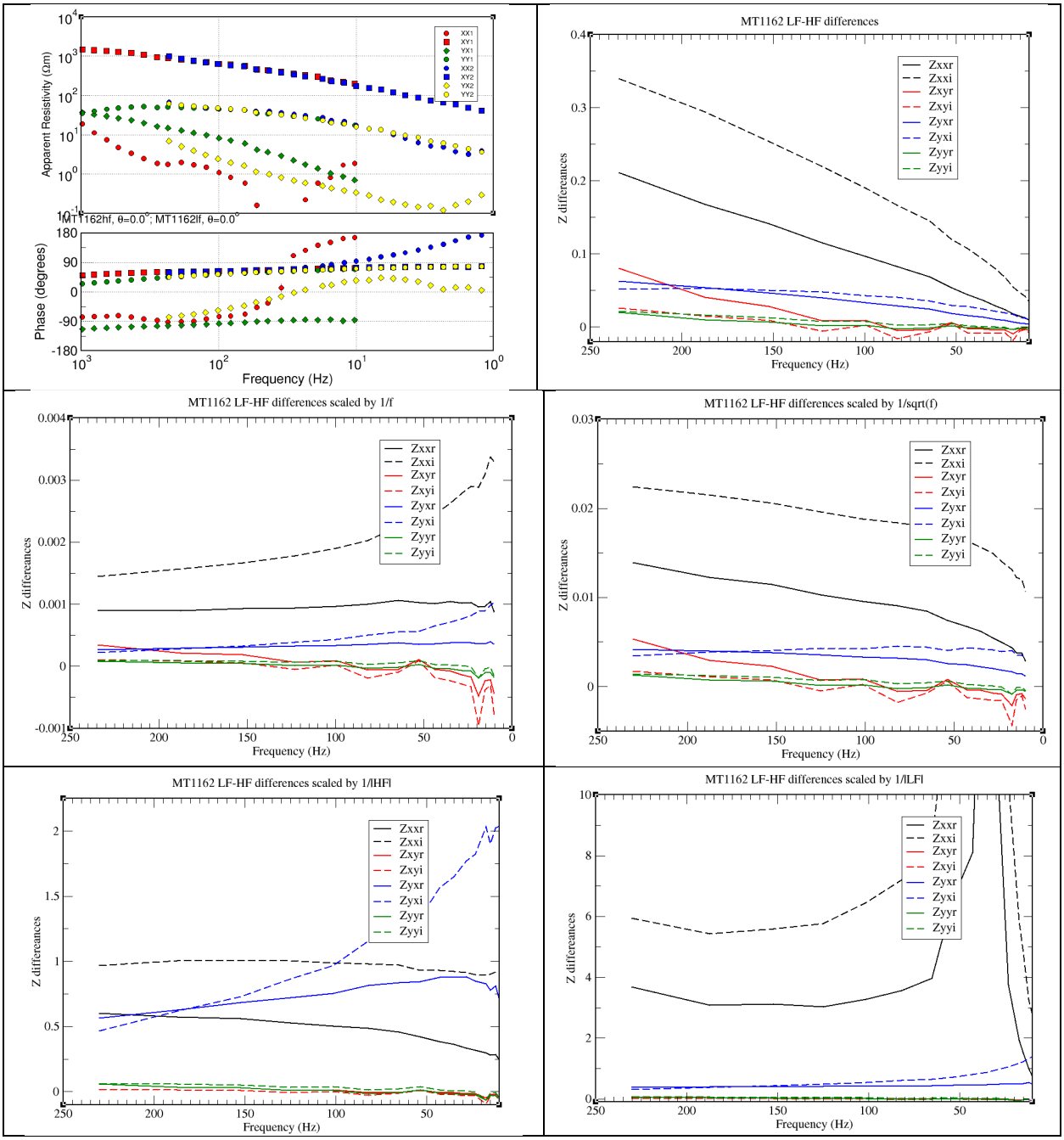

Figure 20: Impedance differences between the LF and HF estimates for the 16 pairs of overlap frequencies for site MT1162. Top are the unscaled, differences, middle left are the differences scaled by 1/frequency, middle right are the differences scaled by 1/sqrt(frequency), bottom left are the differences scaled by the magnitude of the HF data, and bottom right are the differences scaled by the magnitude of the LF data.

Of these four plots, the one where the XX and YX most agree with each other is when the data are scaled by the magnitude of the HF estimates (Figure 20, bottom left). This is approximately a scaled value of 0.5. The differences in scaled XY and YY are close to zero.

6.2.2. *Site MT1131*

Applying the same approach for the HF and LF data from site MT1131, we see in the Argand diagrams that the Zxy and Zyy are reasonably in agreement, but are shifted along their curves, whereas the Zxx and Zyx show significant disagreement.

The difference plots (Figure 22) show that indeed it IS a frequency effect, as once frequency is taken into account then the differences are almost equal with frequency (Figure 22, bottom right).

There is no apparent consistency between the XX and YX differences, or between the YX and YY differences, and the cause has not been determined.

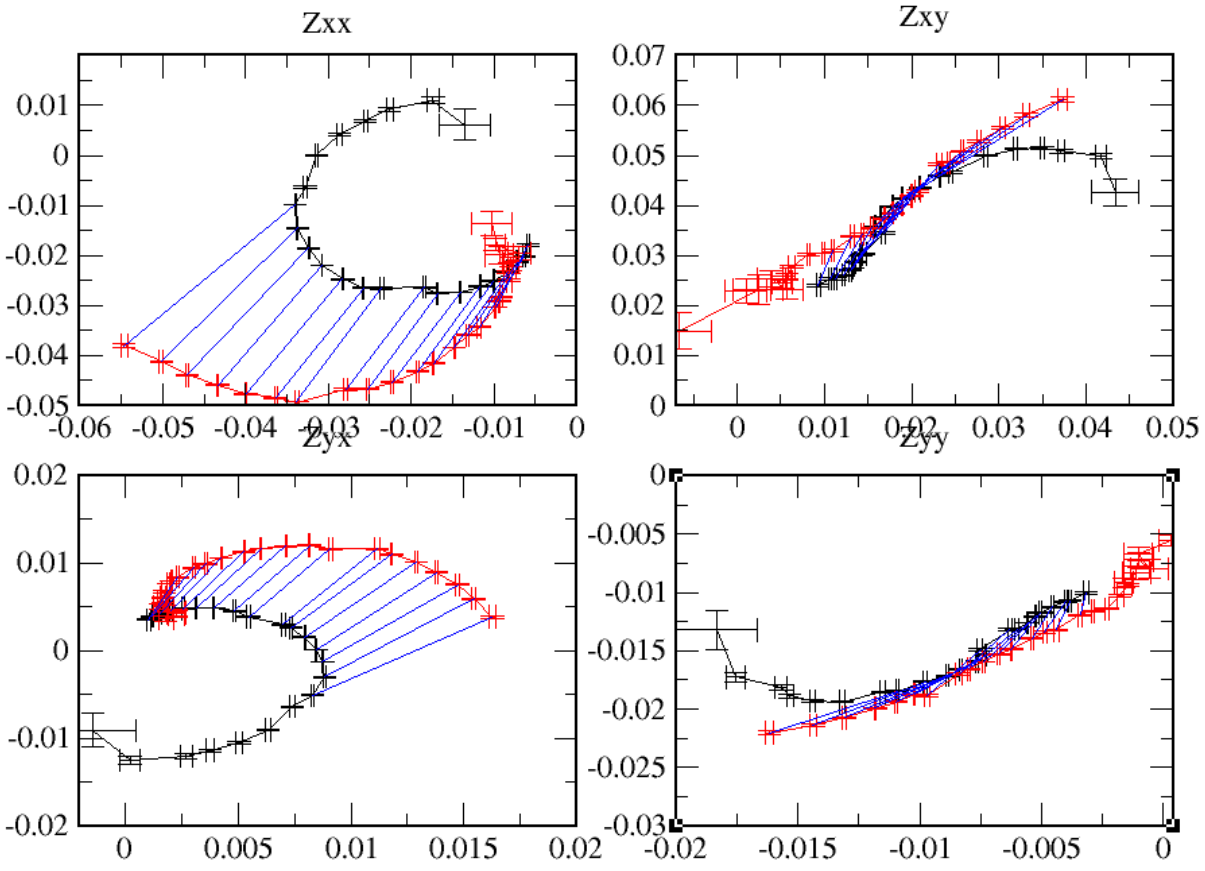

Figure 21: Data from 1 kHz to 1 Hz for site MT1131 plotted in terms of impedances on an Argand diagram. HF in black and LF in red. Overlap points are joined by blue lines.

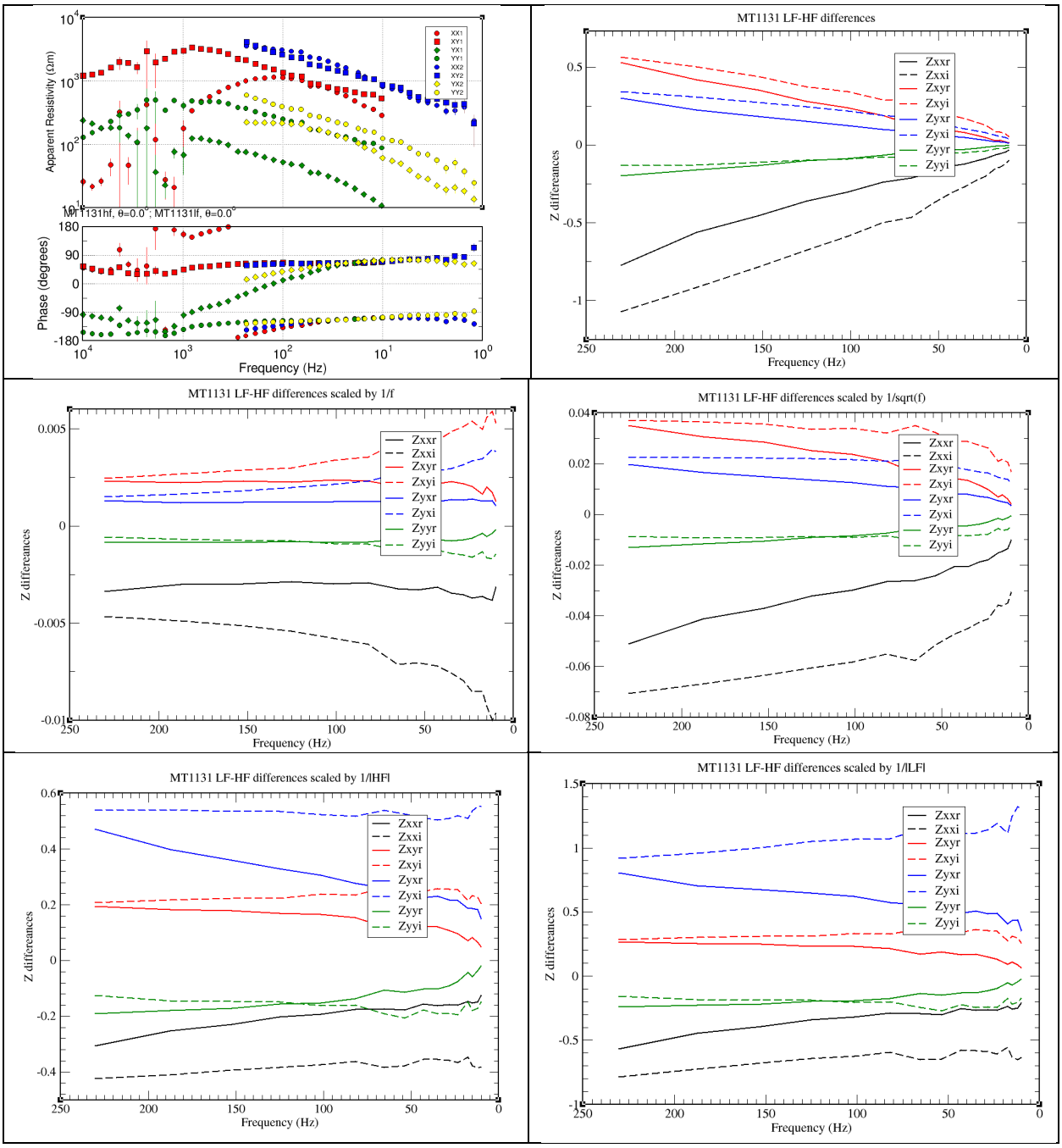

Figure 22: Impedance differences between the LF and HF estimates for the 16 pairs of overlap frequencies for site MT1131. Top are the unscaled, differences, middle left are the differences scaled by 1/frequency, middle right are the differences scaled by 1/sqrt(frequency), bottom left are the differences scaled by 1/the magnitude of the HF data, and bottom right are the differences scaled by 1/the magnitude of the LF data.

6.2.3. *Site MT1232*

A third site examined is MT1232 – see Figure 23 and Figure 24. Again, the frequency sensitivity of the differences is obvious.

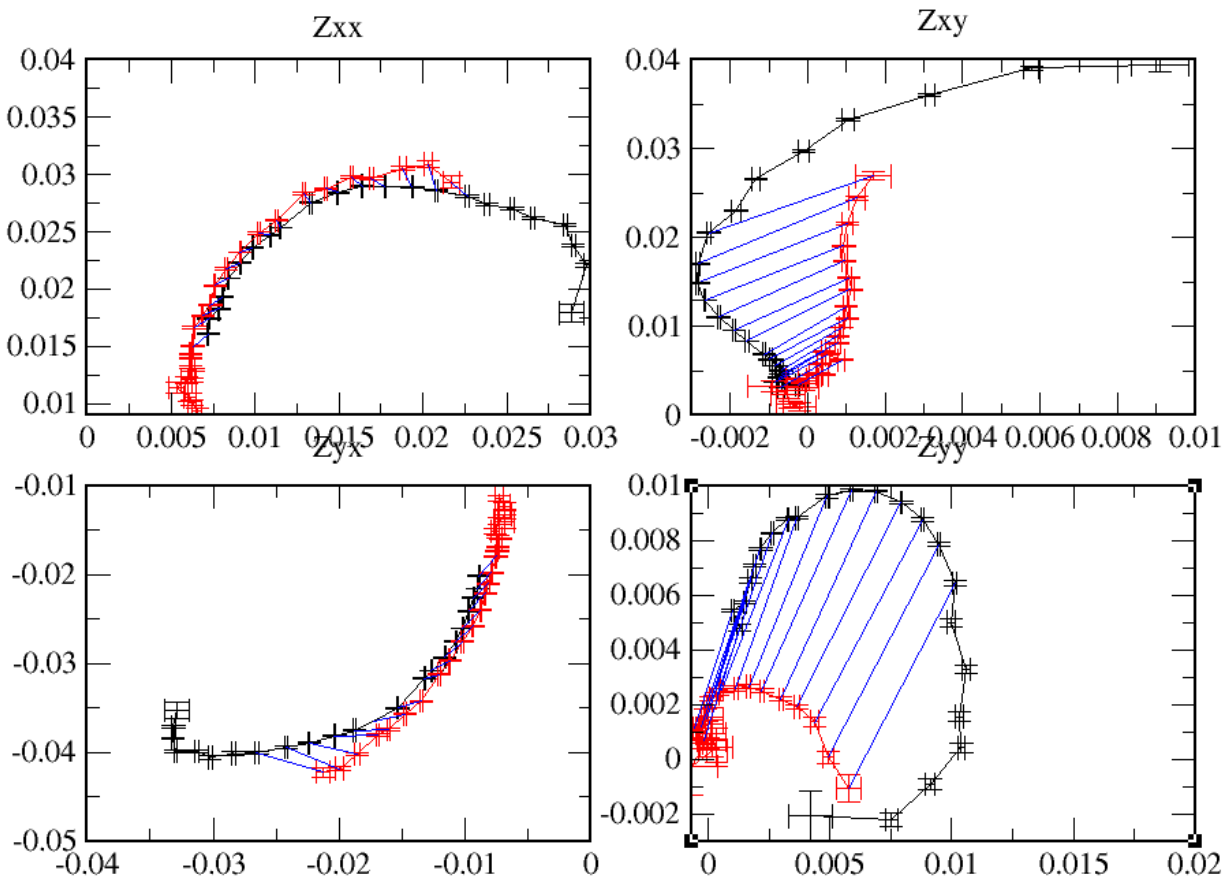

Figure 23: Data from 1 kHz to 1 Hz for site MT1232 plotted in terms of impedances on an Argand diagram. HF in black and LF in red. Overlap points are joined by blue lines.

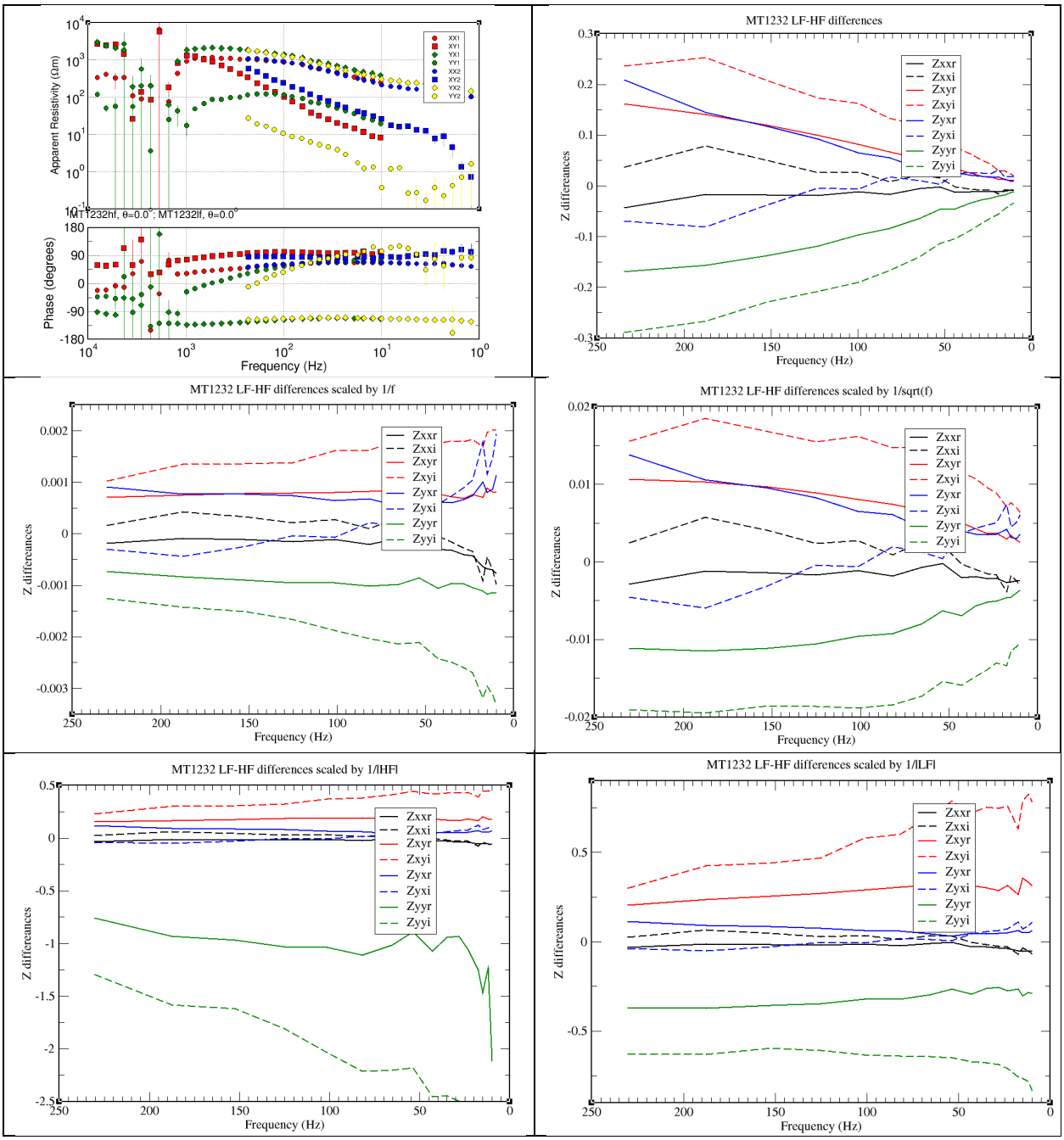

Figure 24: Impedance differences between the LF and HF estimates for the 16 pairs of overlap frequencies for site MT1232. Top right are the unscaled, differences, middle left are the differences scaled by 1/frequency, middle right are the differences scaled by 1/sqrt(frequency), bottom left are the differences scaled by 1/the magnitude of the HF data, and bottom right are the differences scaled by 1/the magnitude of the LF data.

6.2.4. *Site MT1143*

We can examine the data at site MT1143 to try to understand the significant difference between the HF YY responses and the LF YY responses (see Figure 17).

The Argand plots of the impedances are shown in Figure 25, and the differences can be seen as a shift in complex space to the “NE” for the (ZXX,ZYX) pair with the common Hx coils, and to the “SW” for the (ZXY,ZYY) pair with the common Hy coils.

Plotting the absolute impedance differences (Figure 26, left) and the scaled differences (Figure 26, right), we see again that there is a 1/freq dependence.

Note that the curious “V-shaped” HF RhoYY curve is due to the impedance crossing quadrants, from the 1st to the 4th then the 3rd and back to the 1st. This is seen as the PhaYY phase rotating through a full 360° cycle. This is not the case for the LF data, start in the 3rd quadrant and rotate through the 4th quadrant to the 1st quadrant. So what is needed to correct the HF data is a SW translation.

However, the frequency dependence is not precise – there still is some, albeit minor, frequency sensitivity in the 1/f plots.

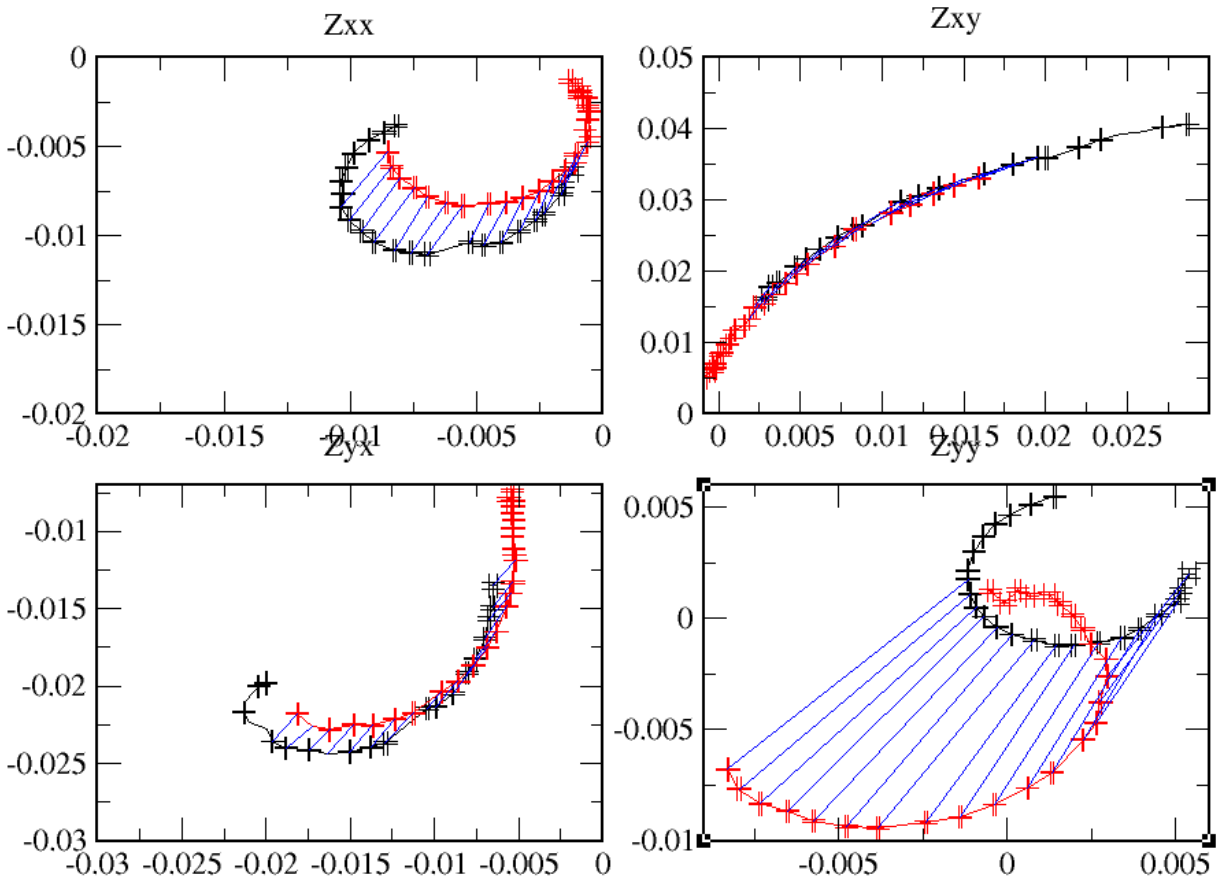

Figure 25: Data from 1 kHz to 1 Hz for site MT1143 plotted in terms of impedances on an Argand diagram. HF in black and LF in red. Overlap points are joined by blue lines.

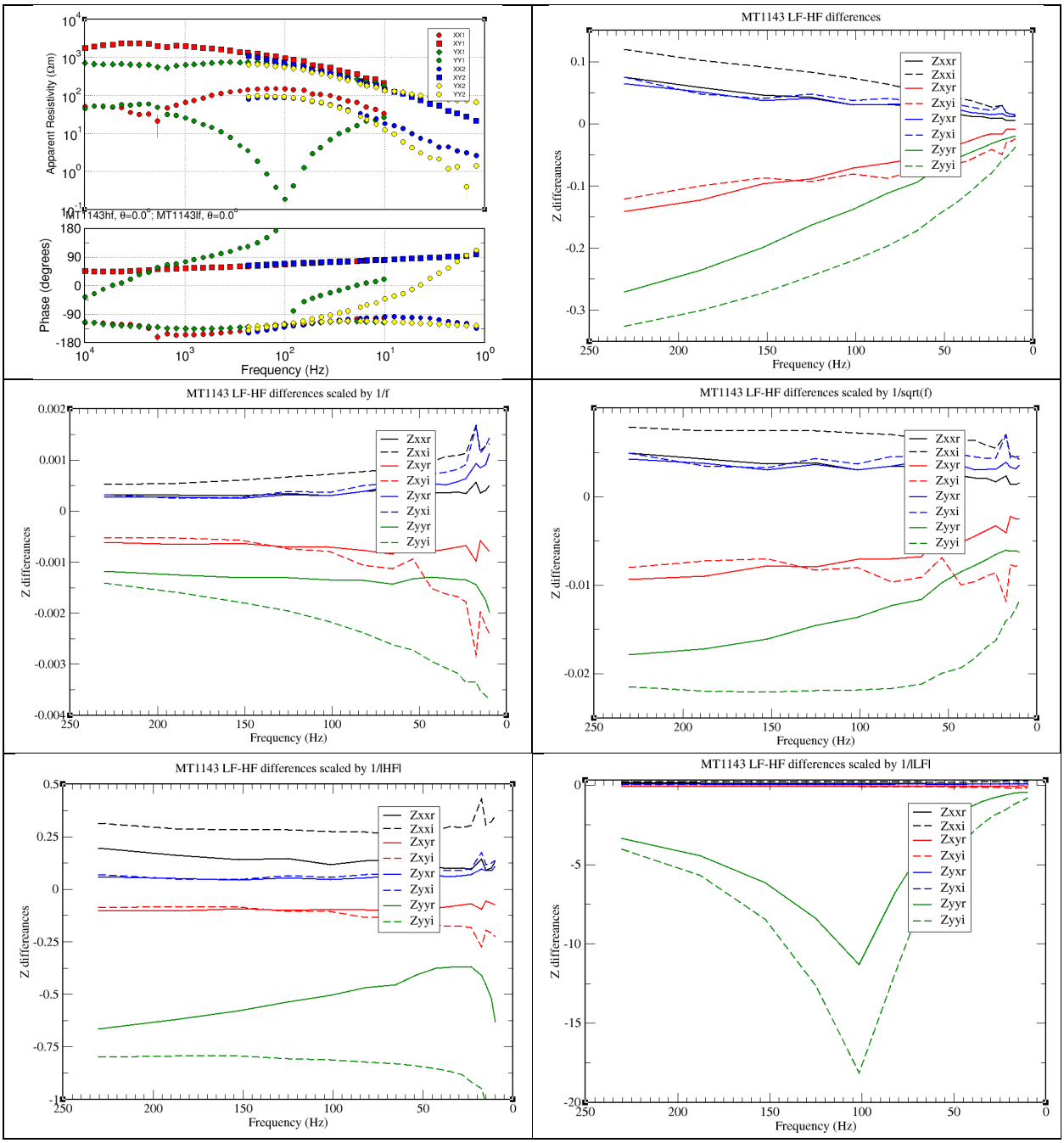

Figure 26: Impedance differences between the LF and HF estimates for the 16 pairs of overlap frequencies for site MT1143. Top are the unscaled, differences, middle left are the differences scaled by 1/frequency, middle right scaled by 1/sqrt(freq), bottom left are the differences scaled by 1/the magnitude of the HF data, and bottom right are the differences scaled by 1/the magnitude of the LF data.

6.2.5. *Site MT1173*

Site MT1173 was recognised as having non-parallel HF and LF RhoYX curves.

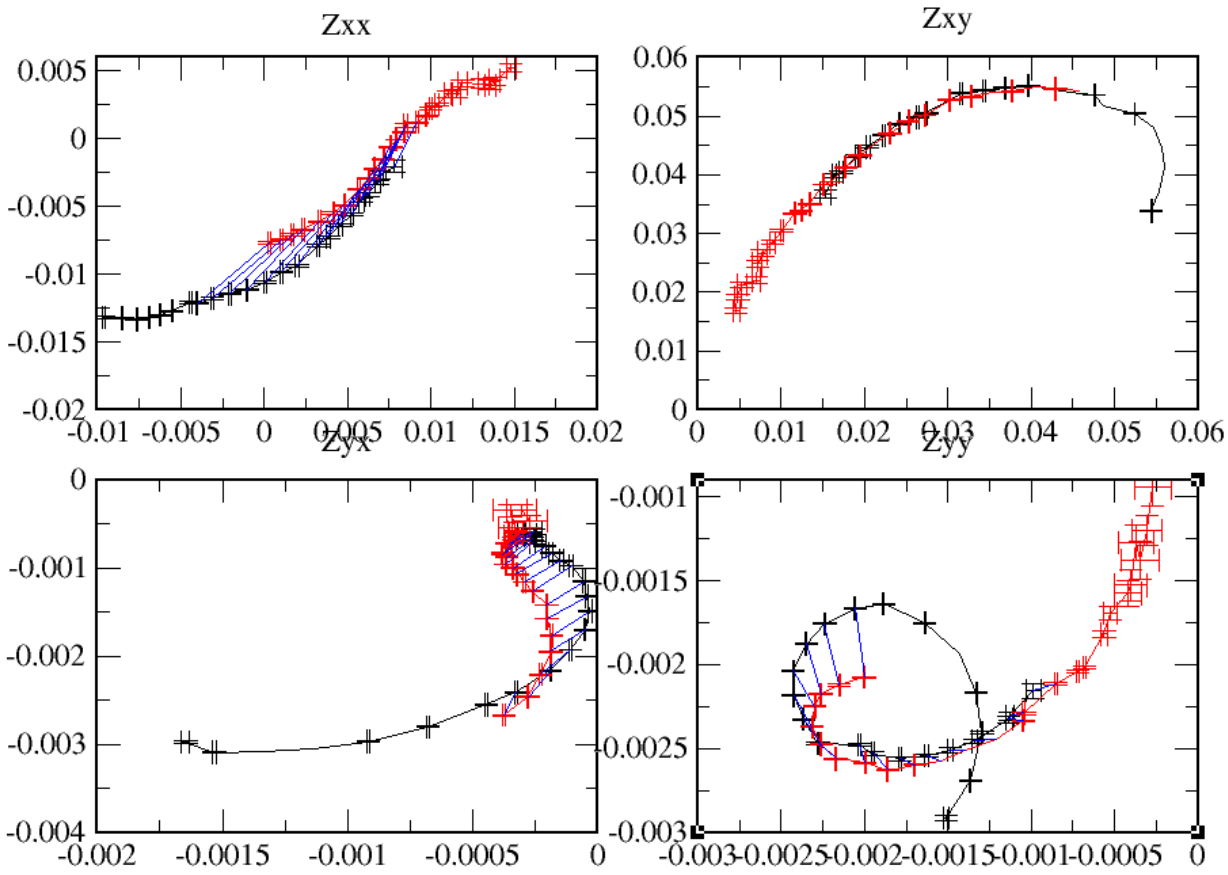

Figure 27: Data from 1 kHz to 1 Hz for site MT1173 plotted in terms of impedances on an Argand diagram. HF in black and LF in red. Overlap points are joined by blue lines.

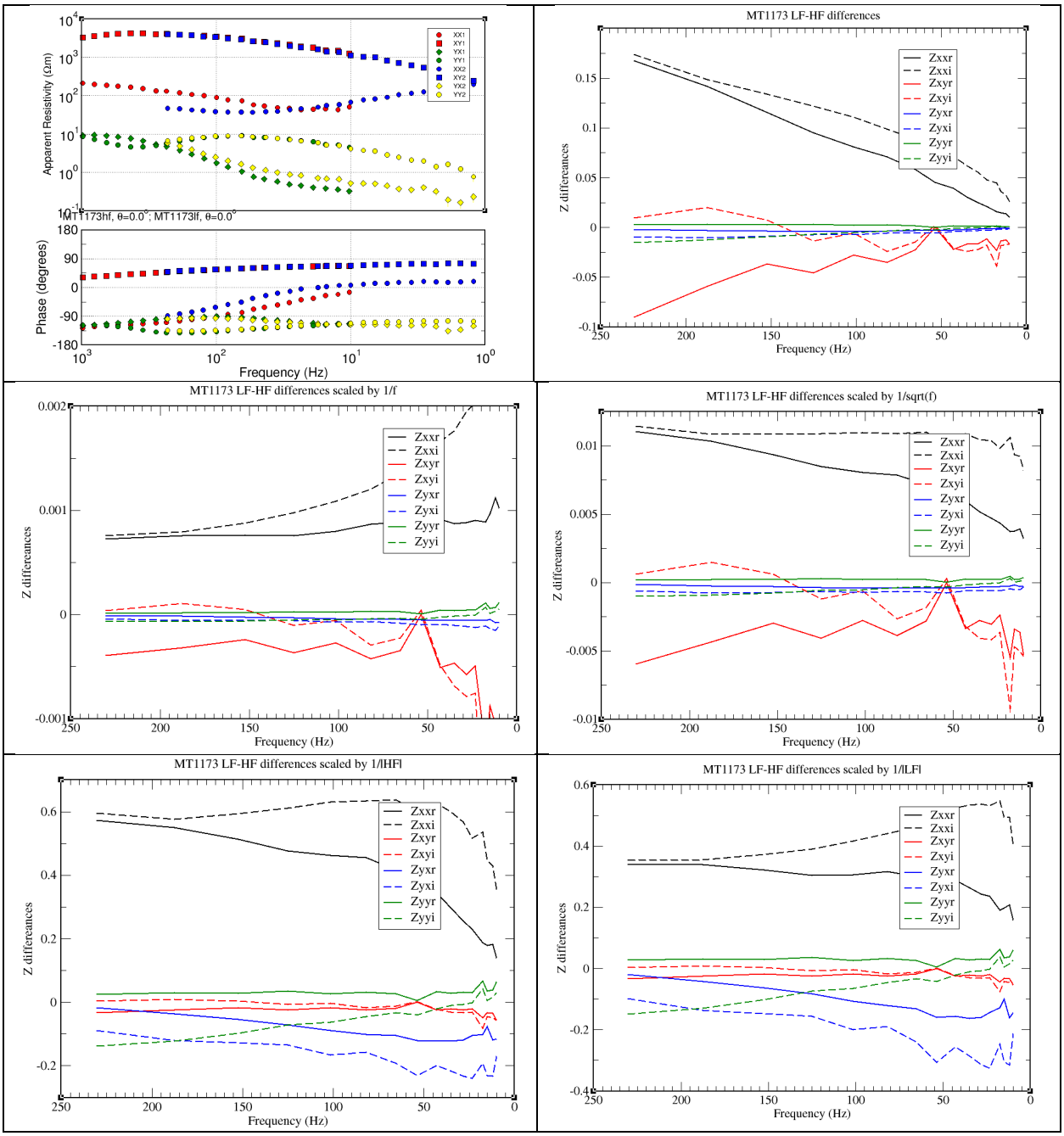

Figure 28: Impedance differences between the LF and HF estimates for the 16 pairs of overlap frequencies for site MT1173. Top right are the unscaled, differences, middle left are the differences scaled by 1/frequency, middle right scaled by 1/sqrt(freq), bottom left are the differences scaled by 1/the magnitude of the HF data, and bottom right are the differences scaled by 1/the magnitude of the LF data.

6.3. Coils used at examined sites

The coils used at the examined sites, plus some others with strong Band Shift, are listed in Table 2. The channels that show marked mismatch are coloured in red.

Table 2: Listing of coils used at examined sites.

	Hx coils		Hy coils	
Site	HF Hx	LF Hx	HF Hy	LF Hy
MT1131	GHF-1054	P50-2387	GHF-1055	P50-2456
MT1143	GHF-1103	P50-3100	GHF-1113	P50-3101
MT1162	GHF-1054	P50-2387	GHF-1055	P50-2456
MT1173	GHF-1045	P50-3098	GHF-1061	P50-3117
MT1232	GHF-1054	P50-2387	GHF-1055	P50-2456
MT1272	GHF-1103	P50-3100	GHF-1113	P50-3101

The table shows that there is no discernible pattern, coil pairs used at one site give some to significant Band Shift, and at another site given little to no Band Shift.

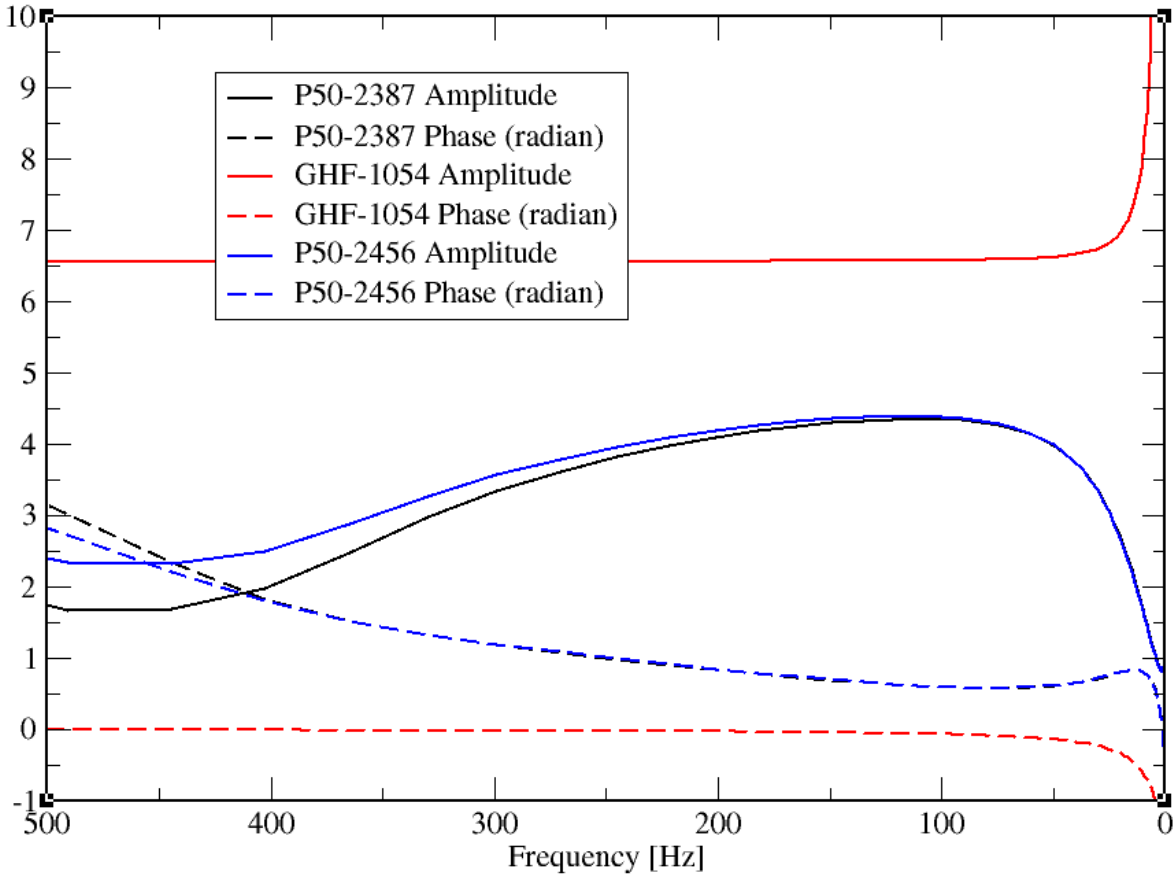

Figure 29: Calibration factors for the Geometrics G100K coil GHF-1054 (red) compared to two Phoenix MTC-50H coils, P50-2387 (black) and P50-2456 (blue). Amplitude factors are solid lines and phase factors (in radian) are dashed lines.

Plotting the calibration factors given by the contractor for GHF-1054 and P50-2387, and also P50-2456 for comparison, we see that the Geometrics G100K coil has a flat response in the overlap band of frequencies from 250 – 10 Hz, so that coil calibration file cannot be contributing to the Band Shift.

For the Phoenix coils, as these are long period coils there is some amplitude and frequency variation in the overlap band. However, the two coils examined are virtually identical.

6.4. Test of misaligned HF and/or LF coils

Two of the suggestions made by the contractor to explain Band Shift imply misalignment of the HF and/or LF coils, i.e., that the HF-Hx coil was not parallel to LF-Hx coil, and/or the HF-Hy coil was not parallel to LF-Hy coil. Misalignment between the Z_{hf} and Z_{lf} data can be described by a rotation of the Z_{hf}, viz.:

$$Z_{LF} = Z_{HF}\ R_h^T$$

where R_h^T (transpose of $\boldsymbol{R}_h$) is the transposed Cartesian rotation matrices for the magnetic channels, given by

$$R_h^T = \begin{bmatrix} cos\theta_{Hx} & sin\theta_{Hx} \\ -sin\theta_{Hy} & cos\theta_{Hy} \end{bmatrix} ,$$

and *Hx* and *Hy* are the azimuth differences of those respective channels with respect to their HF directions. Multiplying these matrices out for the impedance elements we get:

$$Z_{xx,LF} = cos\theta_{Hx} Z_{xx,HF} - sin\theta_{Hy} Z_{xy,HF} ,$$

$$Z_{xy,LF} = sin\theta_{Hx} Z_{xx,HF} + cos\theta_{Hy} Z_{xy,HF} ,$$

$$Z_{yx,LF} = cos\theta_{Hx} Z_{yx,HF} - sin\theta_{Hy} Z_{yy,HF} ,$$

$$Z_{yy,LF} = sin\theta_{Hx} Z_{yx,HF} + cos\theta_{Hy} Z_{yy,HF} .$$

For site MT1311, RhoXY-LF >> RhoXY-HF at the same frequencies, and that can only come from a significant θ_{Hx} that has rotated Z_{xx} into the Z_{xy}, as any error in θ_{Hy} will result in a <u>reduction</u> of Z_{xy}.

Taking the impedance values for frequencies 19 and 20 listed in Table 1, and assuming the misalignment error is solely in Hx (i.e., θ_{Hy}=0), then for Zxy we have:

$$Z_{xy,LF} = sin\theta_{Hx} Z_{xx,HF} + Z_{xy,HF} ,$$

➔ (1.4203, 2.32365) = $\sin\theta_{Hx}$ (-1.3045,0.3757) + (0.8888,1.7620) .

Real part gives: $sin\theta_{Hx}$ = (1.4203 – 0.8888)/(-1.3045) = -0.4074 ∴ θ_{Hx} ≅ -24°

Imag part gives: $sin\theta_{Hx}$ = (2.32365 – 1.7620)/(0.3757) = 1.495 ∴ θ_{Hx} impossible

Alternatively, we can consider Zyx, and there we need to assume, the opposite in order to derive the smallest angle θ_{Hy} as any θ_{Hx} will reduce the amplitude of $Z_{yx,LF}$.

$$Z_{yx,LF}=cos\theta_{Hx}Z_{yx,HF}- sin\theta_{Hy}Z_{yy,HF}$$

(0.6186, 0.1474) = (0.3180, -0.1953) - $sin\theta_{Hy}$ (-0.4181, -0.7077)

Real part gives: $sin\theta_{Hy}$ = (0.6186 – 0.3180)/(-0.4181) = -0.7190 ∴ θ_{Hy} ≅ -46°

Imag part gives: $sin\theta_{Hy}$ = (0.1474 + 0.1953)/(-0.7077) = -0.4842 ∴ θ_{Hy} ≅ -29°

We can perform the same exercise for all four elements and for all 16 pairs of frequencies, to see if there is a common pair of angles that suit all the data.

Instead, I set this up as a minimization problem, with a simple line search over [-45°, 45°] for both θ_{Hx} and θ_{Hy} to find the nRMS misfit between Z_{LF} and rotated Z_{HF} scaled by the error in Z_{LF} for all 16 pairs. The misfit surface is shown in Figure 30. The nRMS misfit for θ_{Hx}= 0 and θ_{Hy}=0 is 22.71, and the minimum nRMS found is 18.52 for θ_{Hx} = +14 and θ_{Hy} = +45 .

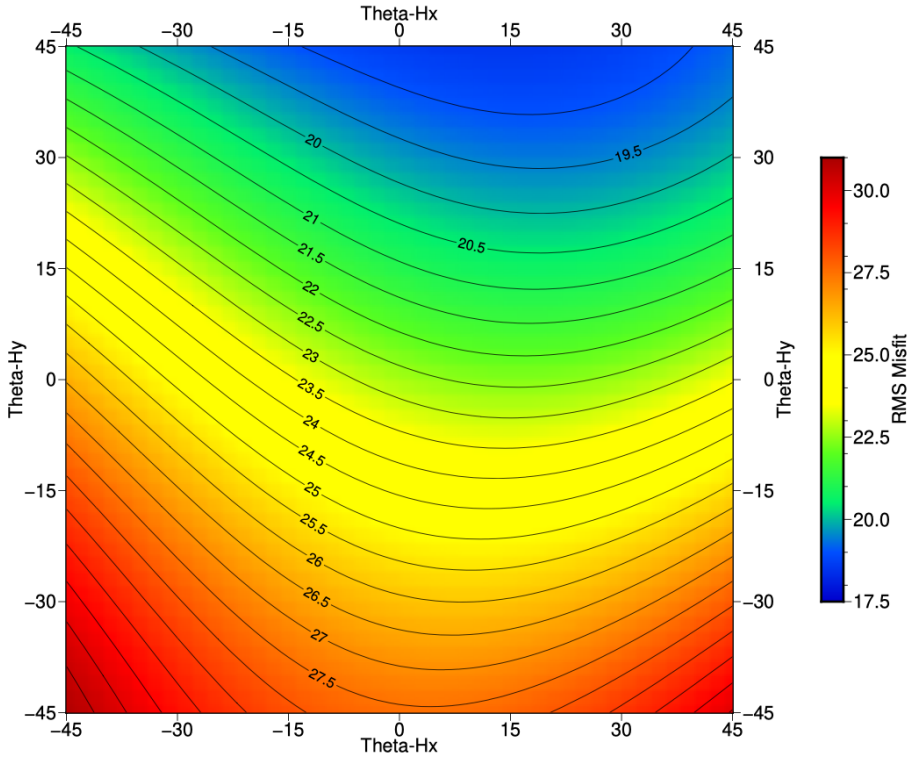

Figure 30: RMS Misfit surface of (Z_{LF} - rotated(Z_{HF})) over all four elements and all 16 pairs of frequencies.

For the data examined here, sensor misalignment of the magnitude required to produce the observed Band Shift would exceed the range expected under normal field practice. MTGS therefore considers misalignment between the HF and LF sensors to be an unlikely sole cause of the Band Shift.

6.5. Comparison of sites MT1131, MT1162, MT1232

We might gain some insight from comparing the impedance differences in detail for three sites that all used the same coil combinations in the same channels, namely sites MT1131, MT1162 and MT1232 that used GHF-1054+P50-2387 for Hx and GHF-1055+P50-2456 for Hy.

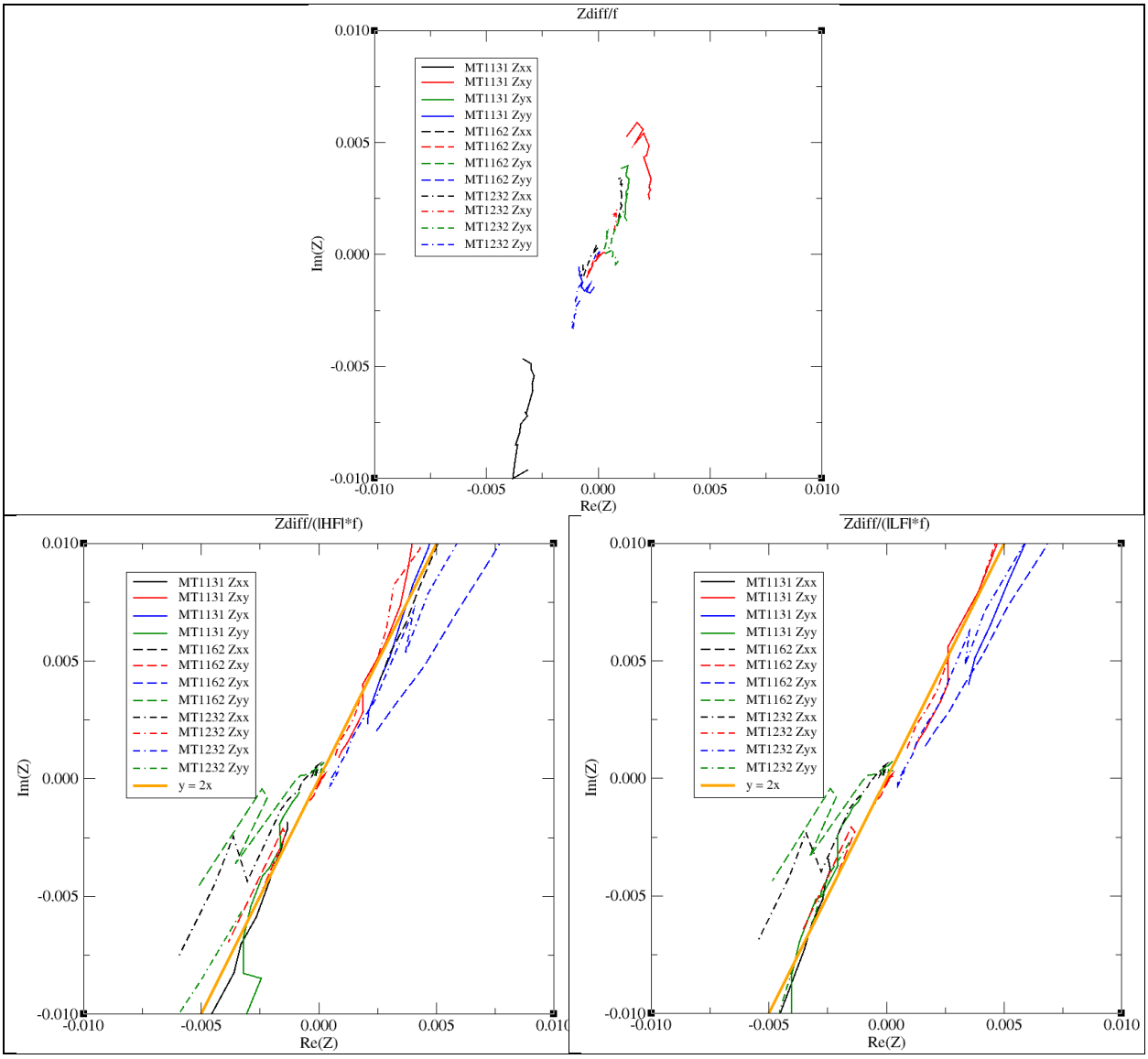

*Figure 31: Argand diagrams of the LF-HF impedance differences for the four elements for three sites scaled by 1/frequency (left) and by 1/(LF magnitude * frequency) (right).*

First we plot the differences scaled by 1/*f* for the three sites and four impedance element differences in Figure 31 (left) and then also scaled by 1/(HF magnitude * *f*) (bottom left) and 1/(LF magnitude * *f*) (bottom right).

Scaling by 1/(|HF or LF| magnitude × *f*) leads to consistency between the three sites, with the scaled differences all lying along a line of approx. *Im = 2*Re* from (-0.005,-0.010) to (0.005,0.010) (orange line on Figure 31).

➔ This observation does not identify the underlying physical mechanism, but it offers a tractable empirical conditioning approach.

Note that if it was an amplitude effect only, then the alignment of the differences would be vertical without any imaginary component. That it is not vertical shows that the effect is both amplitude and phase related.

Also note that the correction is not the same for the two elements in each column of the impedance tensor, i.e., the correction is different for XX than for YX, and is different for XY than for YY.

To confirm we are on the right track, we compare two other sites that use the same coils as each other, but different from the above three. These two are MT1143 and MT1272, using GHF-1103+P50-3100 for Hx and GHF-1113+P50-3101 for Hy. Certainly for MT1143 the impedance differences are consistent with the orange line (Figure 32). For MT1272 the differences do seem to be systematically somewhat more vertical than the orange line.

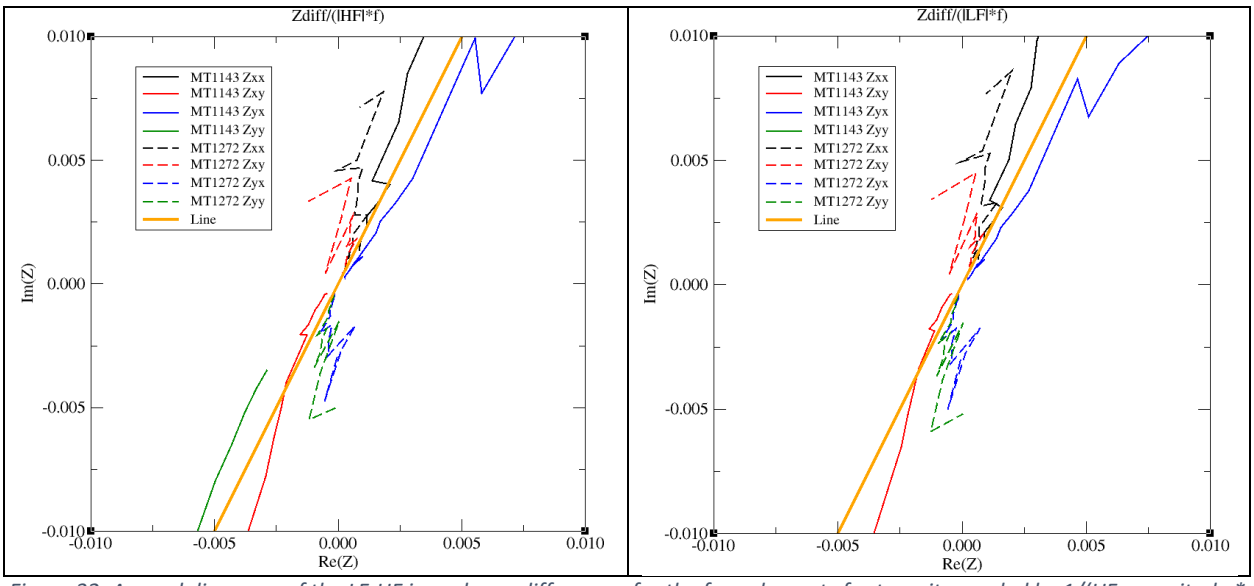

*Figure 32: Argand diagrams of the LF-HF impedance differences for the four elements for two sites scaled by 1/(HF magnitude * frequency) (left) and 1/(LF magnitude * frequency) (right).*

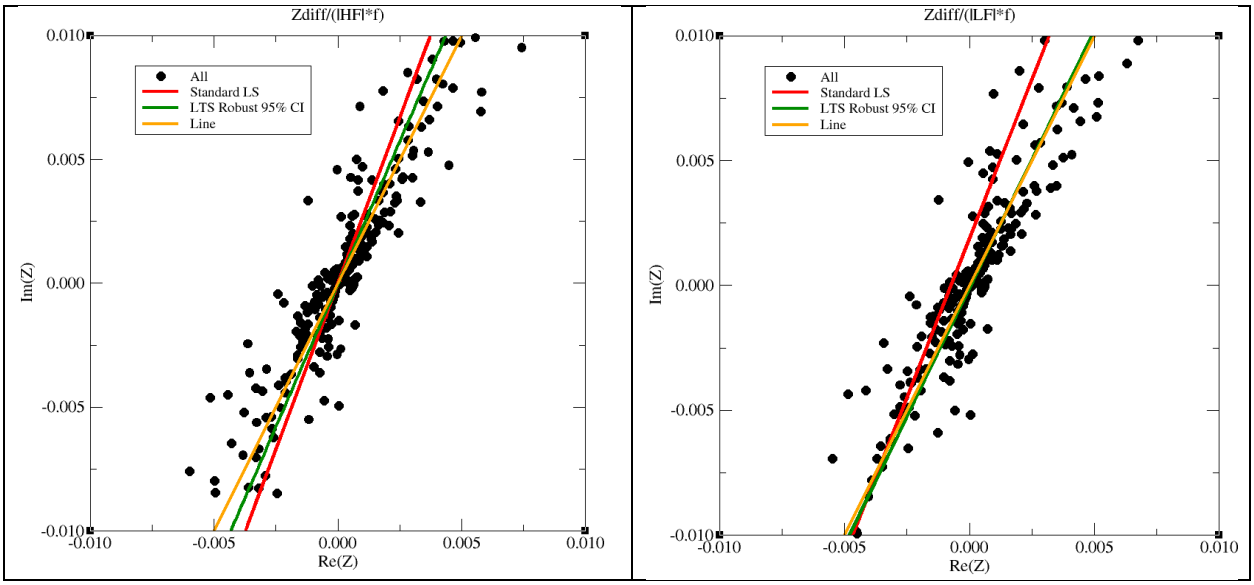

*Figure 33: Linear regression fits to the data of the LF-HF impedance differences for the four elements for two sites scaled by 1/(HF magnitude * frequency) (left) and 1/(LF magnitude * frequency) (right). The red lines are the Standard LS regressions, the green lines are the 95% confidence intervals of the robust Fasano-Vio regressions, and the orange line is a y = 2x line for reference.*

We can take all of the data from the above 1./(HFmag*f) and 1./(LFmag*f) normalized differences and fit a least-squares regression model to it. The standard regression is not appropriate, as it assumes there is no error in the (usually) x variable and the error is only in the y variable. (The standard regressions are shown in red lines on Figure 33.) As there is error in both variables, we fit a regression using an updated version of the York method *York* [1966; 1969] by *Fasano and Vio* [1988]. This gives regression lines of:

Normalized by 1./(HFmag*f): Im(scaled Zdiff) = 0.00003 + 2.71 * Re(scaled Zdiff),

Normalized by 1./(LFmag*f): Im(scaled Zdiff) = -0.017 + 2.58 * Re(scaled Zdiff).

The problem with standard least-squares is that it is highly susceptible to bias from outliers and leverage points, and is not robust. There are a number of ways of performing robust LS, and I choose a Least Trimmed Squares (LTS) approach of *P. J. Rousseeuw* [1984]. (This is the same approach used by Jones and Joedicke in robust processing that is part of the Phoenix time series processing code.) Applying an LTS-based LS regression yields intercepts and gradients of:

Normalized by 1./(HFmag*f): Im(scaled Zdiff) = -0.00002 + 2.30 * Re(scaled Zdiff),

Normalized by 1./(LFmag*f): Im(scaled Zdiff) = -0.00001 + 2.06 * Re(scaled Zdiff).

after 160 iterations, i.e., 50% of the data were iteratively discarded. The 95% confidence intervals of these regressions are shown on Figure 33 (green lines).

MTGS concludes that, to within experimental error:

$$Im(LF(f2)) - Im(HF(f1)) = 2 * Re(LF(f2)) - Re(HF(f1))$$

➔ This is somewhat visible in the difference plots, but now it is statistically established as robust and reliable.

7. Revised correction approach

Given the above observations, the revised correction approach was:

1) Derive the differences between the HF and LF frequency pairs for the Real and Imaginary parts of the impedance elements separately, scaled by 1./frequency.
2) Divide the scaled Imag differences by two.
3) Derive the robust average of the 32 scaled differences (16 real and 16 imag), "*Av*"
4) Derive the correction factor, "*Corr*" at each frequency *f*, given by (*Av***f*)
5) Derive the corrected ZHF impedances by ZHFcorr(f) = ZHForig(f) + cmplx(*Corr*, 2**Corr*).

Note that the implicit assumption made is that the correct RhoA levels, and correct Phases, are from the LF Phoenix coils.

7.1. Examples of application

A code was written to perform the five steps outlined above, and is presented for site MT1131.

First the 32 scaled differences were derived, and these are shown in Figure 34 (left). The alternating sawtooth form is because the 32 data are presented as 16 Real and Imaginary pairs (this plot is the same data as in Figure 22, top right, with the Real and Imaginary curves intermixed). There is clearly some scatter, especially at the low frequencies, and some residual frequency effects in the Zxx component.

The sample means and sample standard deviations were derived from all 32 points, then the LTS algorithm was applied removing successively the point that contributed most to the sample variance. The variation of the sample means with LTS iteration is shown in Figure 34 (right), and clearly all but the Zxx sample mean asymptotes to stable values with rejection of less than half of the values.

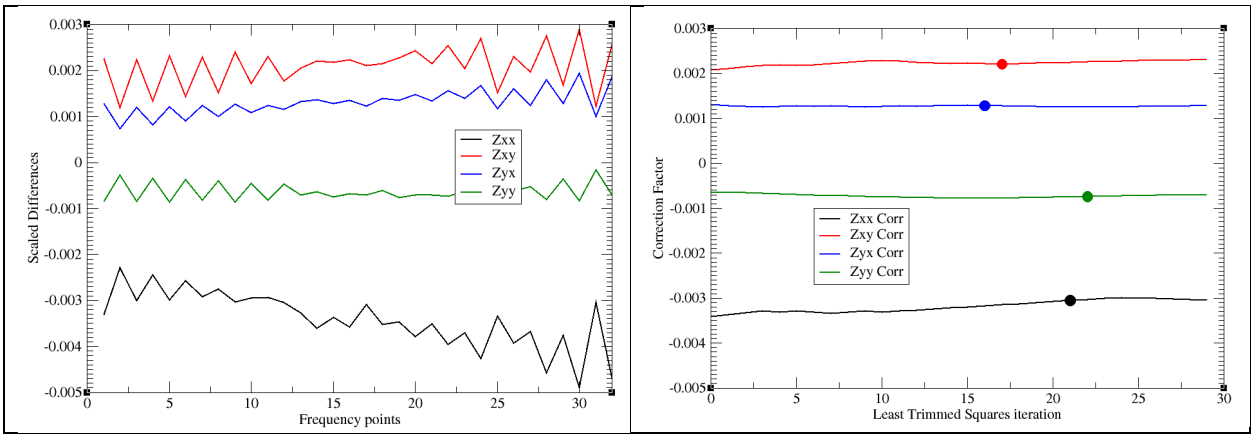

Figure 34: Left: Impedance differences for the 16 pairs given in pair order Re/Im. Right: Averages using LTS rejection. The points show the iteration where the sample variance is <5% of the initial sample variance.

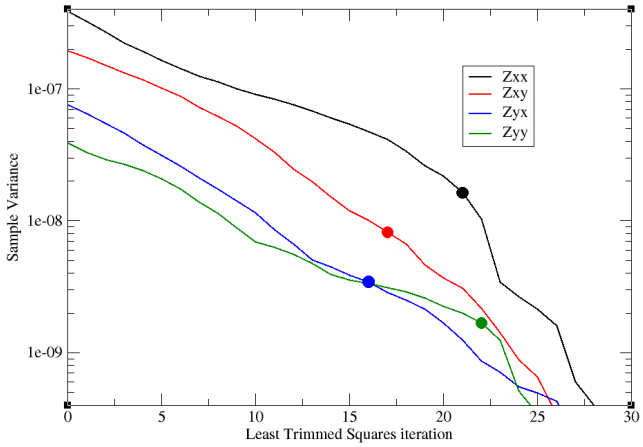

Figure 35: Reduction of sample variances with LTS iteration. The points show the iteration where the sample variance is <5% of the initial sample variance.

This can be seen visually in the plot showing the reduction of the sample variances with LTS iteration (Figure 35). Three of the curves asymptote early, whereas for Zxx it needs 23 points to be rejected to derive a stable sample mean.

To protect against bias from too few points, the scheme was implemented with each iteration sequence ending when the sample variance is less than 5% of the initial sample variance. For site MT1131 this occurred as shown in Figure 35 by the filled circles after 20, 16, 15 and 21 iterations respectively for XX, XY, YX and YY. The resulting best Correction Factors are shown by the filled circles in Figure 34 (right), and are -3.05E-3, 2.21E-3, 1.29E-3 and -7.40E-4 for the four elements respectively. Not surprisingly the XX value is highest and the YY value is lowest, as to be expected from the original data.

Applying the corrections to the HF data from site MT1131 shown in Figure 36 (left) we obtain Figure 36 (right).

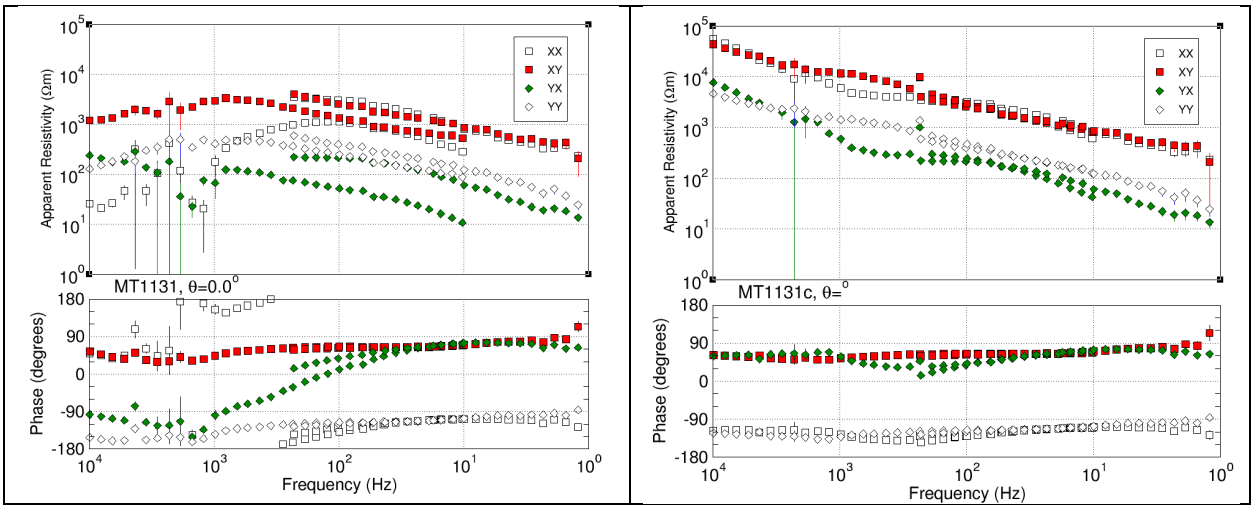

Figure 36: MT1131 original data (left) and HF corrected data (right).

The correction method works well at the overlap frequencies. The problem with it is that it is a function of frequency, so at high frequencies the correction dominates and drives the high frequency phases to 60°, as Imag = 2 x Real, and the RhoA curves to a corresponding slope.

8. Final correction approach

The above approach is tractable at the overlap frequencies, but fails at high frequencies. Treating the LF data as the branch to be corrected, the previous three steps are followed and the fourth step is replaced with:

4) Derive the corrected ZLF impedances by ZLFcorr(f) = ZLForig(f) + cmplx(*Corr*, 2**Corr*).

Applying this correction (Figure 37, right) brings the HF and LF branches into close agreement. The problem is that the correction factor is based on the average of all 16 overlap frequencies, whereas we want to match up the last four.

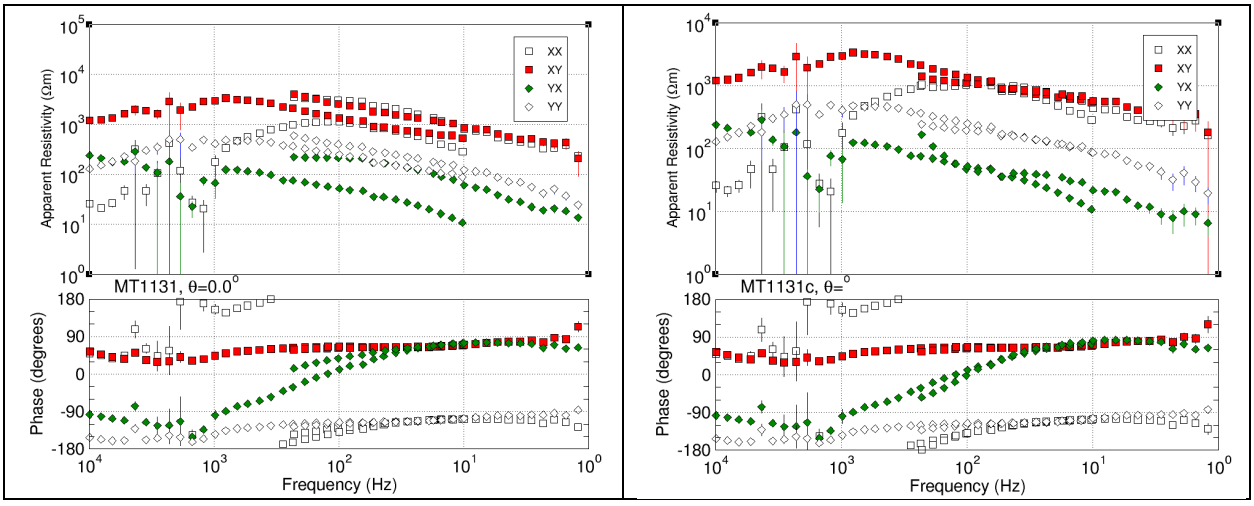

Figure 37: MT1131 original data (left) and LF corrected data (right).

To improve the match for the lowest frequency HF points to the LF estimates, we perform the LTS only on the last four frequency pairs, and also to make the calculation more robust we use the median values of the accepted estimates rather than the means.

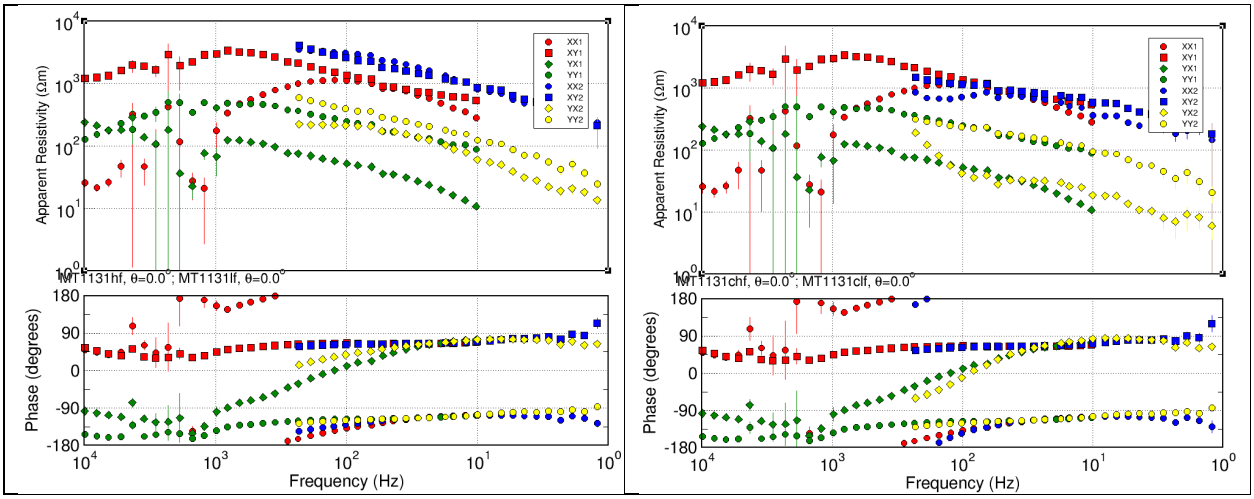

Figure 38: MT1131 original data (left) and LF corrected data (right).

The final corrected version is shown in Figure 38 (right), where the HF and LF estimates are coloured differently for ease of comparison with the original version Figure 38 (left).

The final step is to merge these two sets of estimates together using all of the HF data to 30 Hz, and all the corrected LF data below 30 Hz. We can plot the final merged data as both Zxy and Zyx impedances (Figure 39) and RhoA/Pha curves (Figure 40).

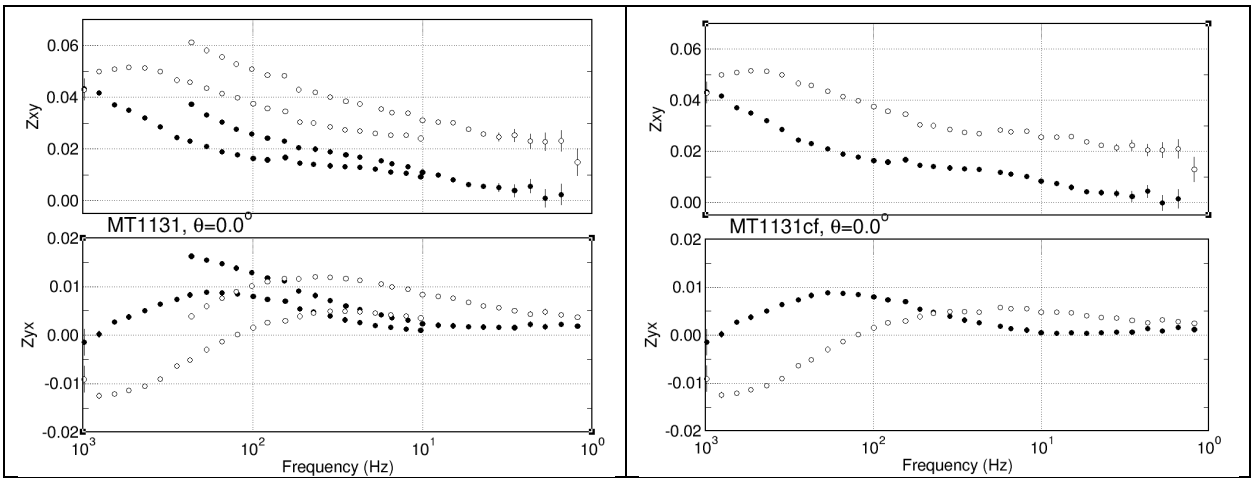

Figure 39: MT1131 original Zxy and Zyx impedances (left) and LF corrected impedances (right). Real parts are in filled circles and Imaginary parts in unfilled circles.

The six sites we have examined above, namely MT1131, MT1143, MT1162, MT1173, MT1232 and MT1272, which all displayed different aspects of the Band Shift, were corrected using the above scheme and the original data and corrected data are show in Figure 40.

Original	Corrected
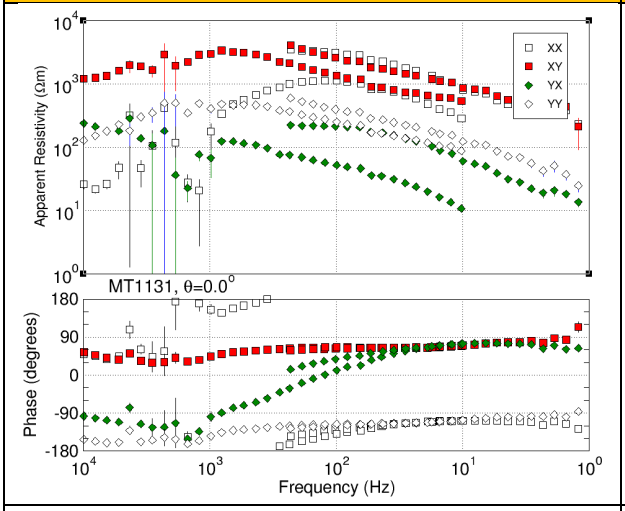	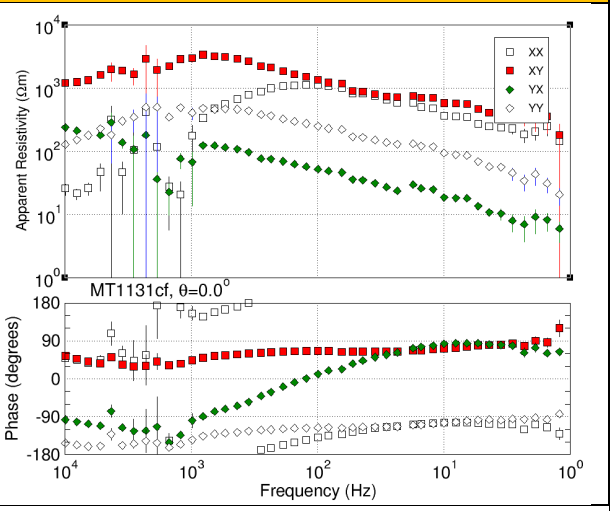
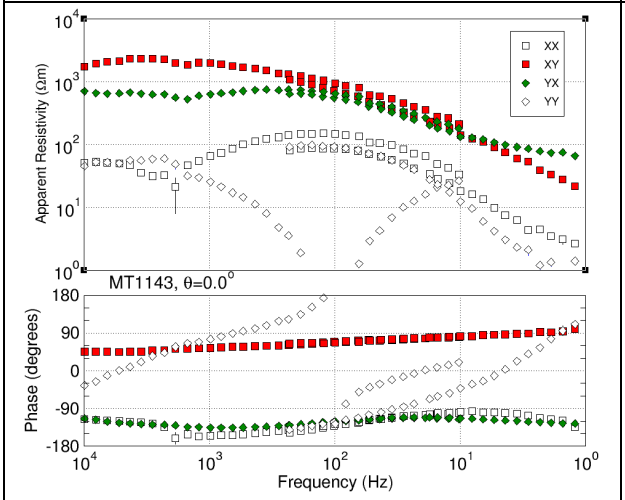	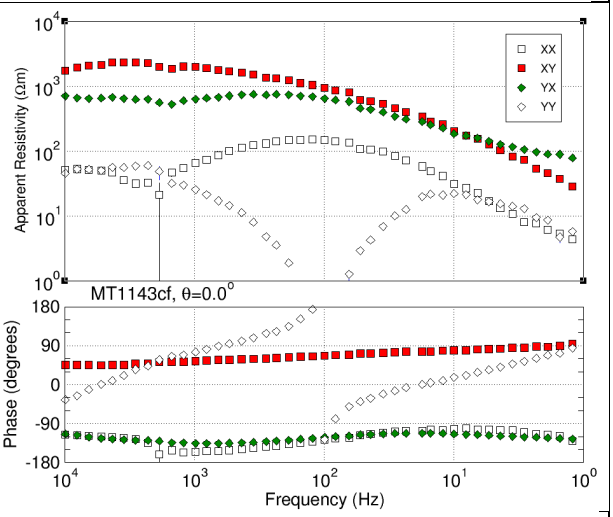
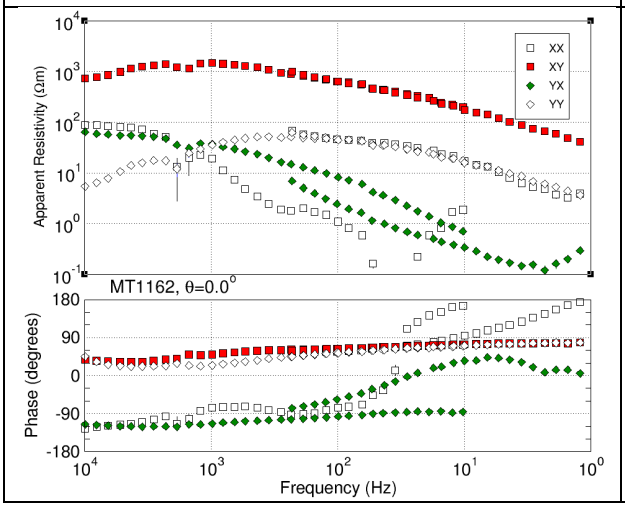	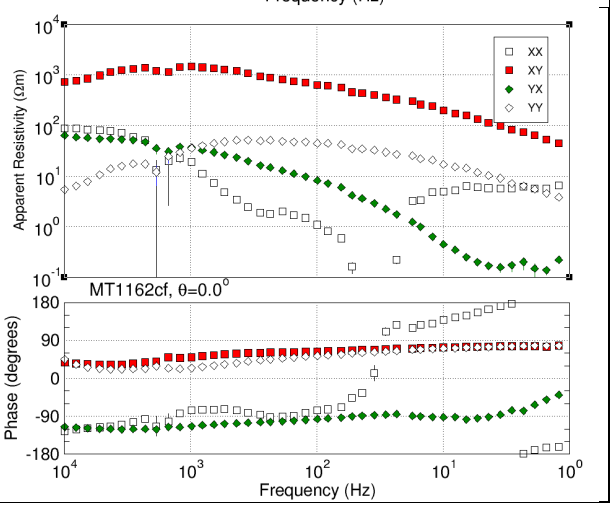

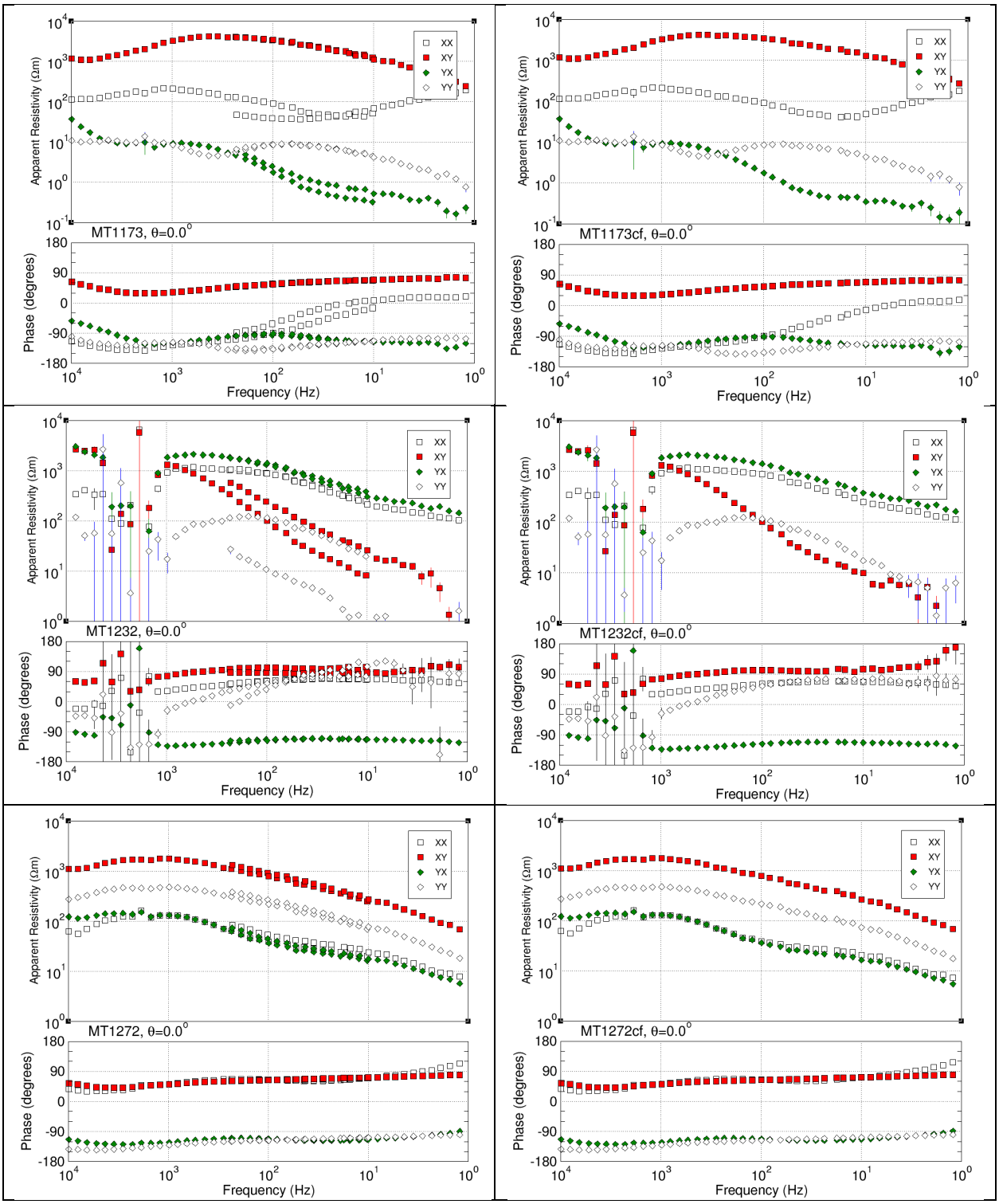

Figure 40: Application of the final correction code to sites MT1131 (top), MT1143 (2nd row), MT1162 (3rd row), MT1173 (4th row), MT1232 (5th row), and MT1272 (bottom row). Left are the original data and right are the corrected data.

9. Band Shift Conclusions

The root cause of the band shift could not be conclusively identified despite extensive testing. Possible mechanisms (motion noise, sensor misalignment, calibration error, magnetic-rock distortion) were each examined and found insufficient to account for the observations.

There seems to be no consistency with regard to particular coil combinations, and in any case the Geometrics coil calibration is flat without any phase, and the Phoenix coil calibration looks normal. As the electric channels used the same equipment for HF and LF acquisition, the effect is most likely associated with the magnetic channels.

The only consistency noted is that the impedance differences appear to display a 1/*f* sensitivity.

There were three reasons offered by the contractor to explain the differences:

1. *There was some high-wind during the survey acquisition; the coils couldn't be dug into the ground as normal due to the very rocky/no soil conditions. This could result in some motion or disturbance of the magnetic sensors after site was set up;*
2. *The amplitude of the magnetic field in the survey area (see regional magnetic field over the Raglan area, see Figure 4-1) is very high and that had an unexpected impact on the field acquisition. The compasses were strongly affected, and the crew reported difficulties to obtain a proper measurement of the azimuth for the sensors ("north arrow of the compasses spinning").*
3. *The crew also noticed some magnetic rocks on the ground and one cannot remove the possibility that the measurements from one coil at a site (either the HF or LF, X or Y) can be 'locally' affected by one high-magnetic rock located below or just next of the coil (i.e. acting like a magnet distorting of the magnetic field on that coil).*

After extensive testing, MTGS was unable to reproduce the observed Band Shift patterns using the mechanisms proposed by the contractor (misalignment, motion noise, magnetic rock distortion). Based on the data available to MTGS, those mechanisms appear insufficient on their own to account for the observed patterns. MTGS does not exclude that additional field information held by the contractor could account for the observations.

Given the inability to identify a conclusive root cause from the provided data, a pragmatic, mathematically-based conditioning approach was developed to make the dataset usable for inversion. This conditioning does not imply a specific physical cause.

We have proceeded on the basis of deriving individual correction factors for each channel at each station. This is a pragmatic rather than a root-cause solution, and the underlying mechanism for the band shift remains unidentified. It does, however, retain the LF estimates rather than removing them.

The correction technique was applied to all of the data and the corrected EDIs are provided as deliverables.

10. Other issues found with the data

MTGS focussed on the EDI data in the *00spectra* folder for the survey, as these are the original response estimates and are in the public domain ([2]). Any problems with those data will appear in one way or another in the subsequent edited and interpolated data. MTGS visually inspected all of the sites, plotting all four impedance elements.

Generally, the data appear to be of good to high quality – this is tested below in the Quality Factors section.

MTGS also notes the following other issues with these data.

10.1. Comparison of repeat sites

Fourteen sites were repeated, namely:

MT1157R.dat MT1158R.dat MT1159R.dat MT1187R.dat MT1195R.dat MT1207R.dat MT1262R.dat MT1264R.dat MT1265R.dat MT1273R.dat MT1274R.dat MT1275R.dat MT1276R.dat MT1277R.dat

and for all but the first three and last one (indicated by underlining) there are two EDI data files.

The off-diagonal XY and YX RhoA and Pha estimates for the ten sites for which there are two files are plotted in Figure 41, with the repeat R labelled as site “1” (XY=black squares and YX=red diamonds), and the original as site “2” (XY=blue squares and YX=green diamonds).

For most pairs, the Repeat occupation does not show measurably higher Quality Factors than the original, and in approximately half of the pairs the lower QF is associated with the Repeat. The two occupations differ in array geometry and coil pairs, which limits direct comparison.

Nonetheless, a significant issue is the restricted consistency observed between initial and subsequent occupations. Repeat measurements at MT sites typically agree to within statistical errors. The differences observed at these 10 repeat sites are substantially larger than is normally encountered for repeat occupations of this type.

[2] https://gq.mines.gouv.qc.ca/documents/EXAMINE/GM71363/.

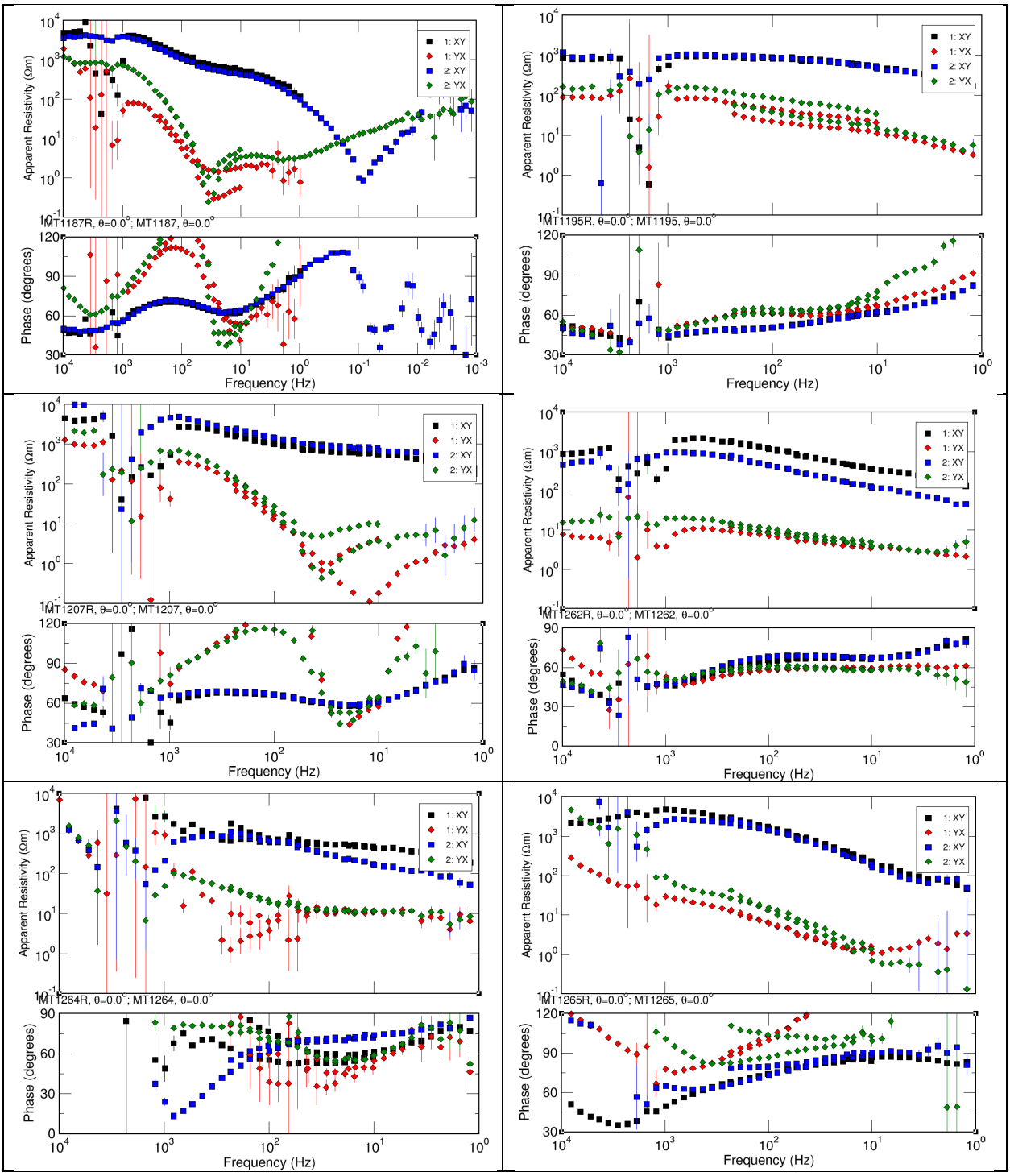
Apparent Resistivity (Ωm)
1: XY
1: YX
2: XY
2: YX
MT1187R, θ=0.0°; MT1187, θ=0.0°
Phase (degrees)
Frequency (Hz)
MT1195R, θ=0.0°; MT1195, θ=0.0°
MT1207R, θ=0.0°; MT1207, θ=0.0°
MT1262R, θ=0.0°; MT1262, θ=0.0°
MT1264R, θ=0.0°; MT1264, θ=0.0°
MT1265R, θ=0.0°; MT1265, θ=0.0°

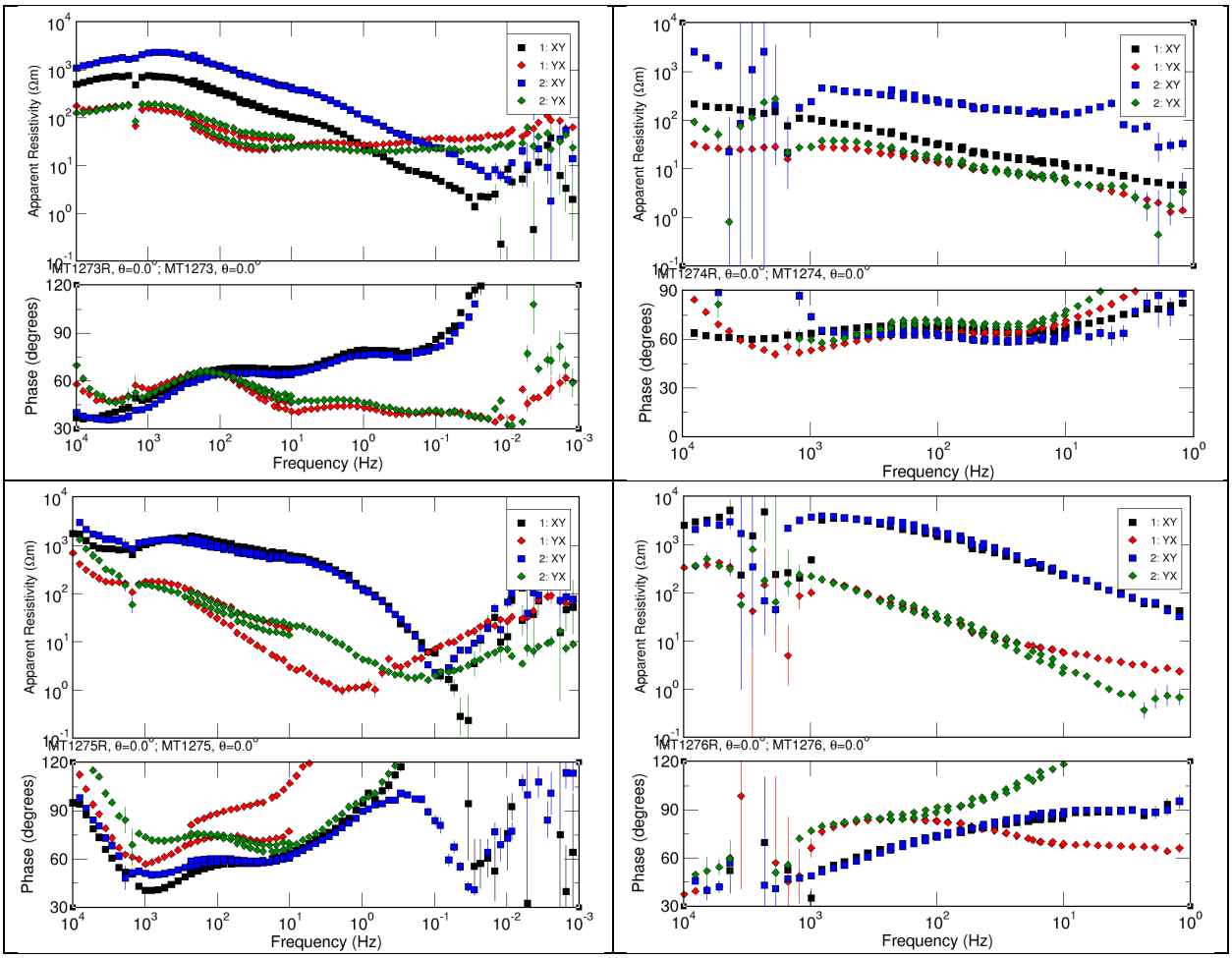

Figure 41: Ten sites for which there are two EDI files, with the repeat R labelled as site "1" (XY=black squares and YX=red diamonds), and the original as site "2" (XY=blue squares and YX=green diamonds).

10.1.1. *Amplitude differences*

For quite a few of the repeat measurements there is an amplitude difference in the RhoA curves but the Pha curves are exactly the same – this is true for example for site MT1273 (Figure 42). The RhoXX and RhoXY curves are about 1/3 of a decade apart, whereas the RhoYX and RhoYY curves are in reasonable agreement, and the phase curves are in statistically excellent agreement.

Data for recording MT1273 used coils GHF-1109+P50-2239 for Hx and GHF-1126+P50-2243 for Hy, and the electrode array was an X-configuration with line length listed as +X=50, -X=50, +Y=50, -Y=50. For recording MT1273R, coils GHF-1099+P50-3090 for Hx and GHF-1121+P50-3091, were used, and the electrode array was a T-configuration with line lengths of +X=100, -X=0, +Y=80, -Y=20.

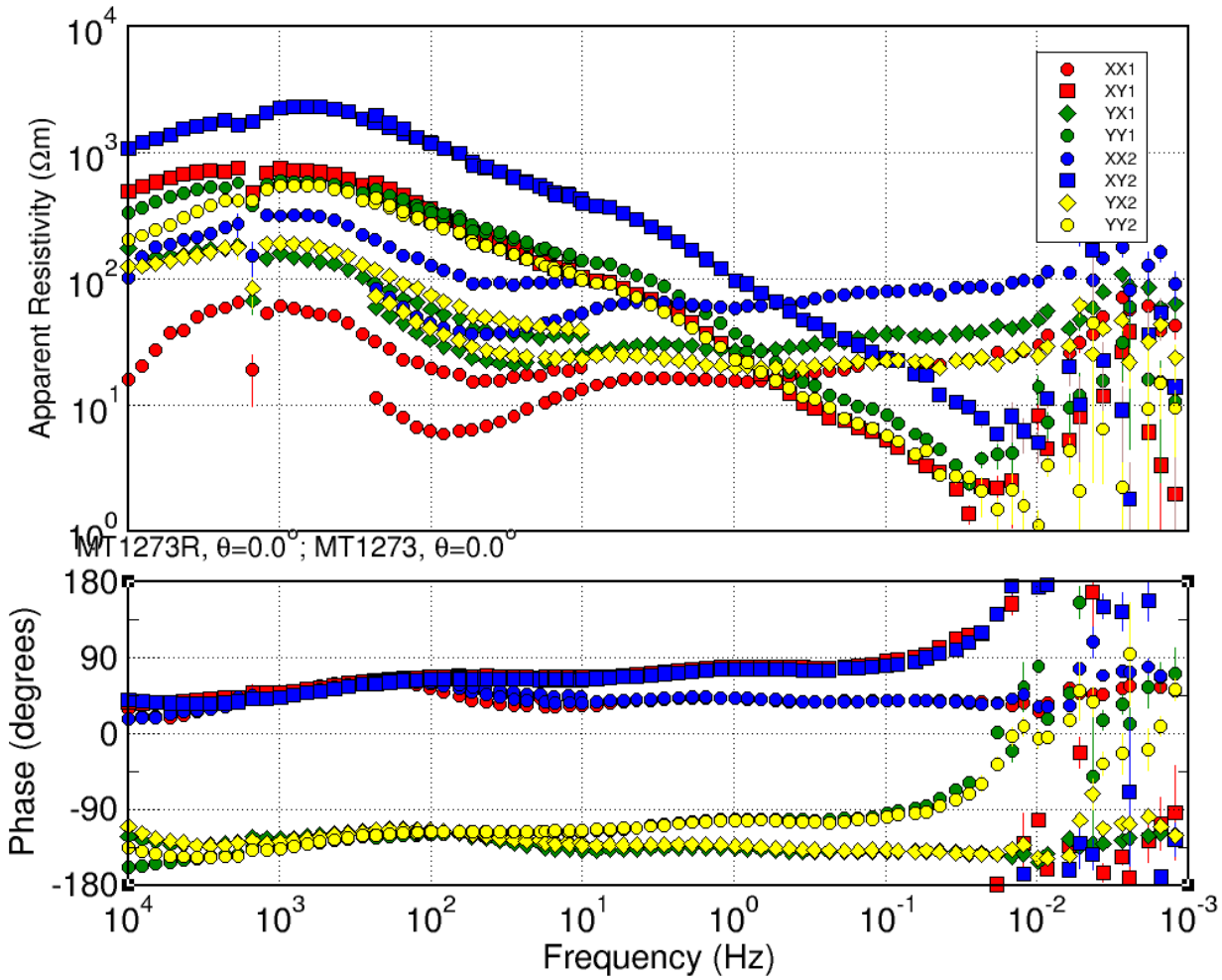

Figure 42: MT estimates for all four elements for site MT1273 from two EDI files, with the repeat R labelled as site "1" (XX,XY=red and YX,YY=green), and the original as site "2" (XX,XY=blue and YX,YY=yellow).

As the effect is in RhoXX and RhoXY, it can be related to the Ex channel. This is most consistent with the recorded value for one of the X line lengths differing from its physical deployment. Calculating the multiplicative differences between the four pairs of RhoA curves in the frequency range of 10 Hz – 0.1 Hz, so as to avoid the Band Shift problems, we get median values of

RhoXX = 3.9 ±0.1 RhoXY = 4.2 ±0.4 RhoYX = 0.8 ±0.05 RhoYY = 0.7 ±0.05.

The components that use the Ex channel, XX and XY, are, to within error, a factor of 4 different, which means an e-field difference of 2 (RhoA is the square of the impedance E/H). Given that the RhoXX and RhoXY original acquisition with elines of 50+50 is, to within error, a factor of 4 less than the Repeat acquisition with elines of 100+0. This factor is numerically consistent with several non-exclusive mechanisms, including a discrepancy between the recorded and deployed length of one X-line, an unrecorded factor-of-two difference in e-field gain, or a wiring or polarity issue affecting the Ex channel.

The data examined here do not allow these alternatives to be distinguished, and MTGS makes no finding as to which (if any) is in fact the cause. Certainly the actual line lengths were all very well determined using DGPS.

Site MT1262 has exactly the same issue – the two pairs of RhoXX and RhoXY curves are offset from each other whereas the phases are in agreement (Figure 43), but in this case the original data are larger than the repeat data. The original recording had an X-configuration electric field array with e-lines of +X=50, -X=50, +Y=50, -Y=50, whereas the Repeat recording had an L-configuration electric field array with e-lines of +X=0, -X=100, +Y=100, -Y=0.

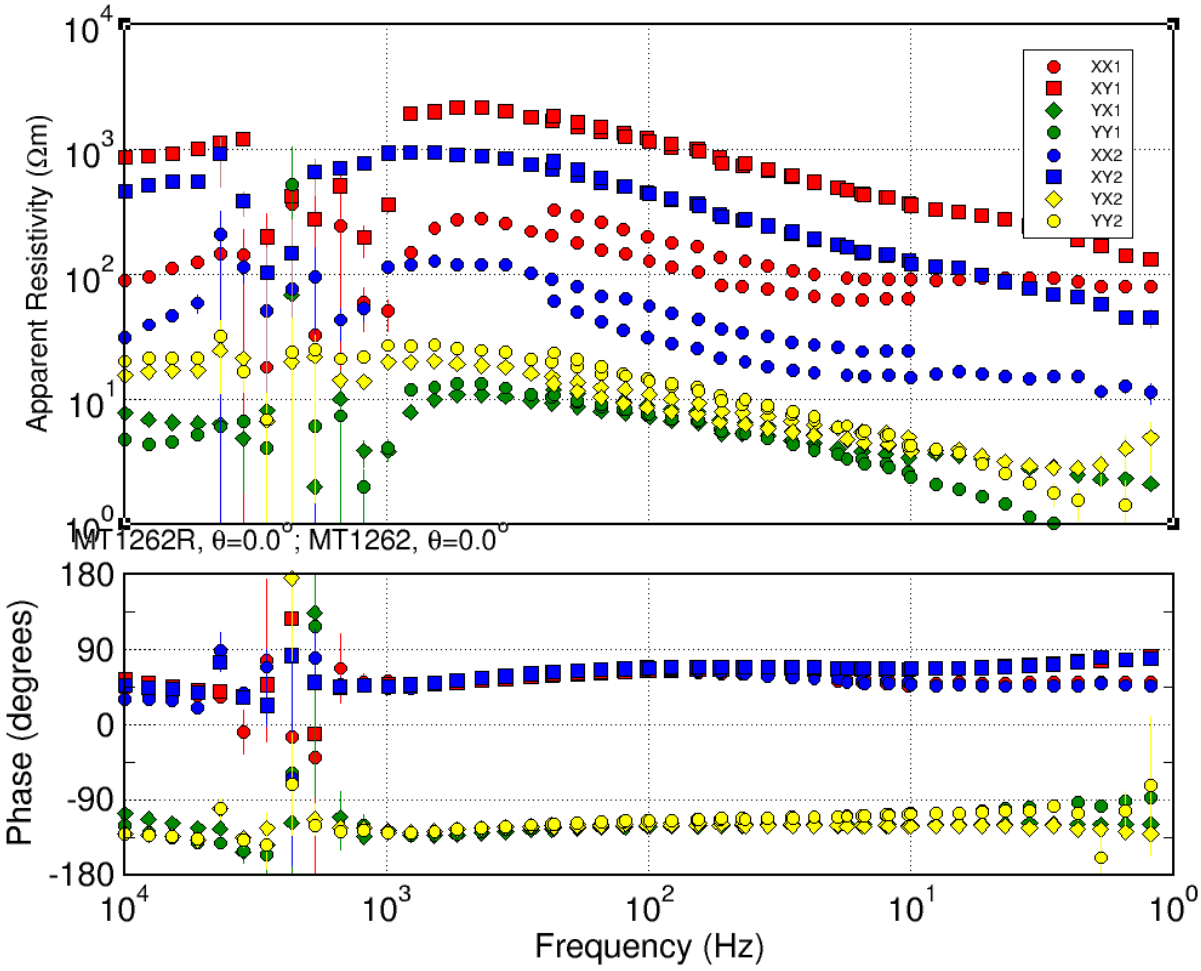

Figure 43: MT estimates for all four elements for site MT1262 from two EDI files, with the repeat R labelled as site "1" (XX,XY=red and YX,YY=green), and the original as site "2" (XX,XY=blue and YX,YY=yellow).

Deriving the multiplicative differences from 300 Hz – 1 Hz for RhoXX and RhoXY, and for RhoYX and RhoYY from 10 Hz – 1 Hz (to avoid Band Shift), they are

RhoXX = 0.25 ±0.10 RhoXY = 0.36 ±0.01 RhoYX = 1.08 ±0.01 RhoYY = 1.79 ±0.5.

RhoXX is exactly consistent with an error that leads to a factor of 1/2 in e-field. RhoXY is not exactly a factor of 1/2, but is close. As discussed above, this factor is numerically consistent with several non-exclusive mechanisms, including a discrepancy between recorded and deployed line lengths, an unrecorded factor-of-two difference in e-field gain, or another acquisition-side cause.

10.1.2. *Different shapes/different phases*

A more pernicious and difficult-to-understand issue is the significant differences in the shapes of the RhoA and Pha curves. An example of this is site MT1267 (Figure 44) for the YX component at low frequencies <30 Hz. Here we see at the low frequencies that the original data has PhaYX going out of quadrant and steeply descending RhoYX curve (yellow diamonds and yellow lines), whereas for the Repeat site PhaYX levels off within quadrant at -111° – -114° and the RhoYX curve begins to level off (green diamonds and green lines).

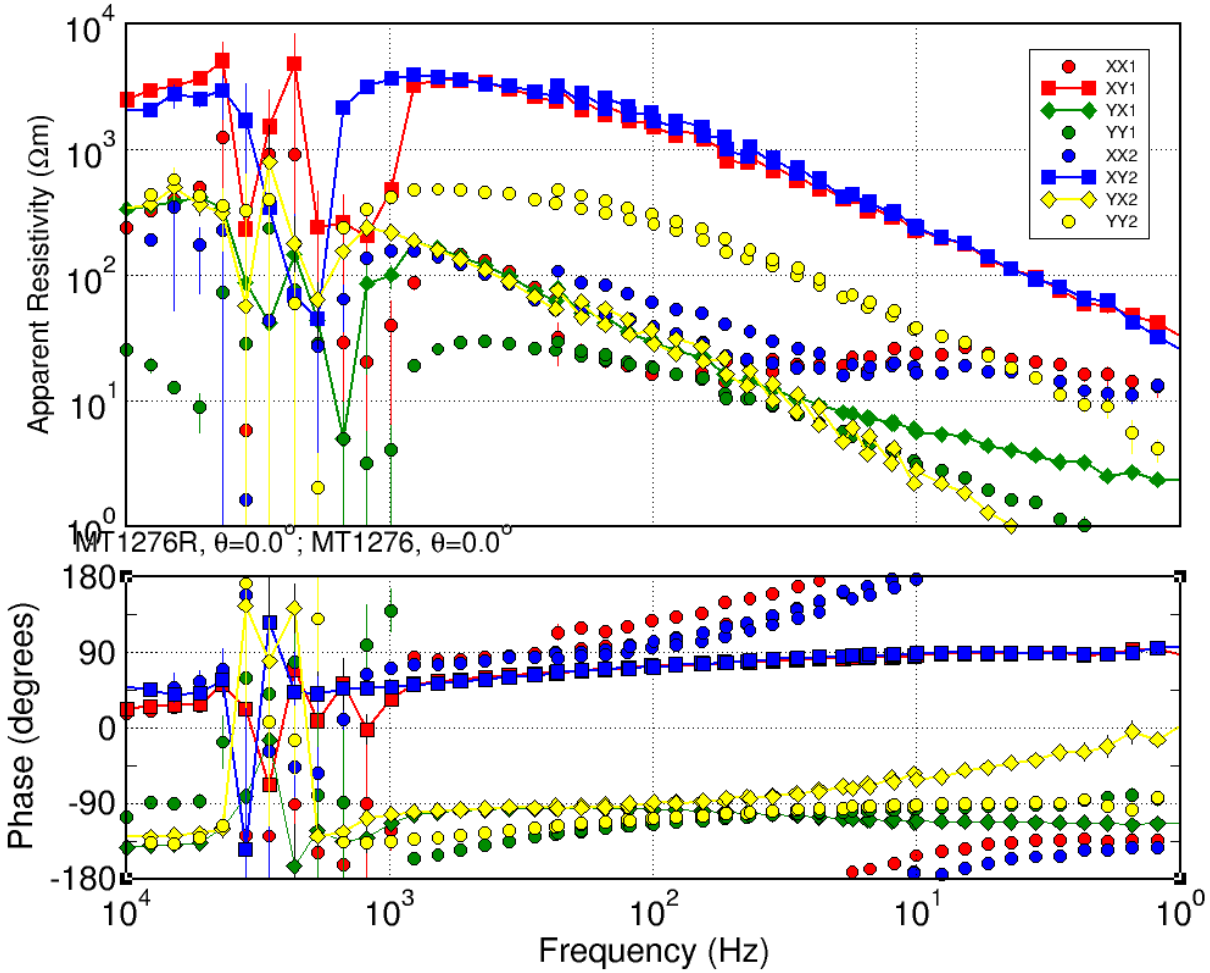

Figure 44: MT estimates for all four elements for site MT1267 from two EDI files, with the repeat R labelled as site "1" (XX,XY=red and YX,YY=green), and the original as site "2" (XX,XY=blue and YX,YY=yellow).

This isn't a simple scaling effect, so isn't an electrode line length data entry error. Also, the LF and HF responses agree quite well, especially for the phases, except for RhoYY curves which are significantly shifted from each other by over an order of magnitude – the factors derived in the range 300 Hz – 30 Hz (to avoid RhoYX issues) are;

RhoXX = 1.02 ±0.90 RhoXY = 1.15 ±0.11 RhoYX = 0.98 ±0.19 RhoYY = 14.9 ±1.9.

There is no ready explanation for this RhoYY shift factor, as all the other curves are in close agreement with each other.

Acquisition for MT1276 used coils GHF-1083+P50-3110 for Hx and GHF-1089+P50-3112 for Hy, whereas for the Repeat site coils GHF-1054+P50-2387 were used for Hx and GHF-1055+P50-2456 for Hy. The P50-3110 and P50-3112 coils are the newer MTC-50Hs, and the P50-2387 and P50-2456 are the older MTC-50s. The calibrations two sets of coils are in agreement internally, i.e. the two MTC-50s agree with each other and the two MTC-50Hs agree with each other. So there is no sign that the coils are the issue.

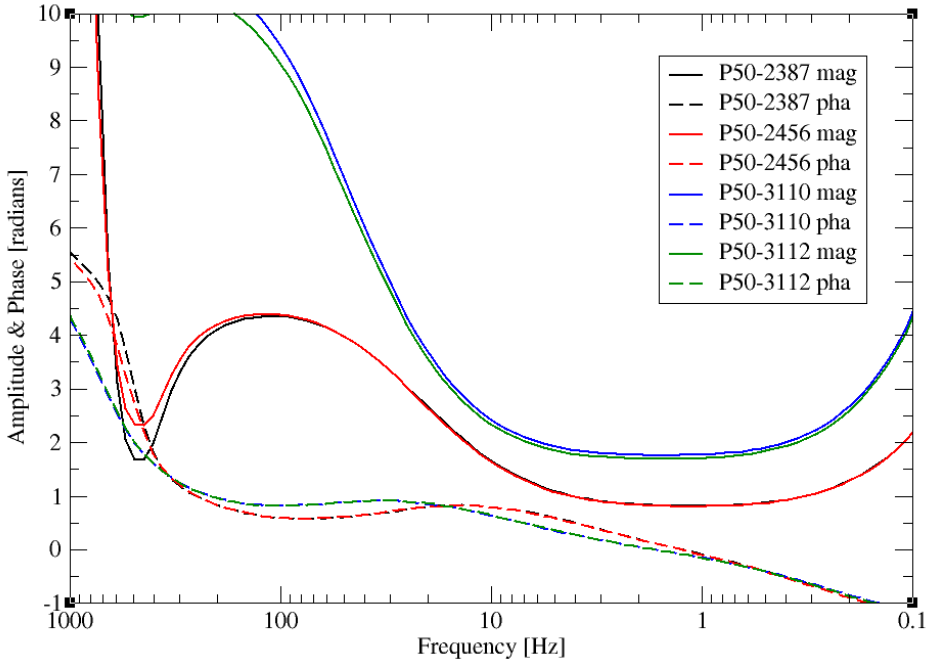

Figure 45: Calibration factors for the four coils used at site MT1276 for the original and repeat recordings.

10.1.3. *Misaligned sensors*

Given the comments by the contractor about the difficulty with magnetic rocks around the sites, it is conceivable that either the Ey or Hx sensors are misoriented. The effect of a misoriented channel is a rotation on the observed impedance $\boldsymbol{Z}_o$ into a rotated reference $\boldsymbol{Z}_r$, viz.

$$Z_r = R_e \, Z_o \, R_h^T$$

where $\boldsymbol{R}_e$ and R_h^T (transpose of $\boldsymbol{R}_h$) are the Cartesian rotation matrices for the electric and magnetic channels respectively, given by

$$R_e = \begin{bmatrix} cos\theta_{Ex} & -sin\theta_{Ey} \\ sin\theta_{Ex} & cos\theta_{Ey} \end{bmatrix} \text{ and } R_h^T = \begin{bmatrix} cos\theta_{Hx} & sin\theta_{Hx} \\ -sin\theta_{Hy} & cos\theta_{Hy} \end{bmatrix} ,$$

and *Ex*, *Ey*, *Hx* and *Hy* are the azimuths of those respective channels with respect to their correct directions. Multiplying these matrices out for the $Z_{yx,r}$ element we get:

$$Z_{yx,r} = +sin\theta_{Ex}cos\theta_{Hx}Z_{xx} - sin\theta_{Ex}cos\theta_{Hy}Z_{xy} + cos\theta_{Ey}cos\theta_{Hx}Z_{yx} - cos\theta_{Ey}sin\theta_{Hy}Z_{yy} .$$

We can see how the misalignment of various sensors will affect the measurement of $Z_{yx,r}$.

For an error in each of the four sensor directions singly, then

Ex error: $Z_{yx,r} = +sin\theta_{Ex}Z_{xx} - sin\theta_{Ex}Z_{xy} + Z_{yx}$ (mixing with both Zxx and Zxy).

Ey error: $Z_{yx,r} = + cos\theta_{Ey}Z_{yx}$ (amplitude scaling effect only).

Hx error: $Z_{yx,r} = + cos\theta_{Hx}Z_{yx}$ (amplitude scaling effect only).

Hy error: $Z_{yx,r} = + Z_{yx} - sin\theta_{Hy}Z_{yy}$ (mixing with Zyy).

Alignment errors of only Ey or only Hx will lead to only amplitude scaling effects on $Z_{yx,r}$, there is no concomitant phase effect (they will of course affect the other elements differently). Note that as they are both sensitive to the cosine, then it doesn't matter which way the sensor is misaligned, whether positive or negative, it has exactly the same effect of reducing the amplitude of the $Z_{yx,r}$ element.

Thus, if there is a phase effect and if there was only one sensor misaligned, it would have to be Ex or Hy. $Z_{yx,r}$ is highly sensitive to Ex misalignment, as it brings in Z_{xy}, which is very large for site MT1276. And $Z_{yx,r}$ is sensitive to the direction of misalignment, as it is a function of the sine of Ex and of Hy.

We can test for misalignment of either Ex or Hy, and the results for +/- 15° of each one are shown in Figure 46. None of these match the two major differences visible in the MT1276R data of (a) increased RhoYX at low frequencies, and (b) reducing PhaYX at low frequencies. However, an error of Ex = +15° does give almost exactly the correct phase response, but the amplitude is somewhat reduced rather than enhanced. However, as discussed by Quantec in their feedback, such an error is highly unlikely.

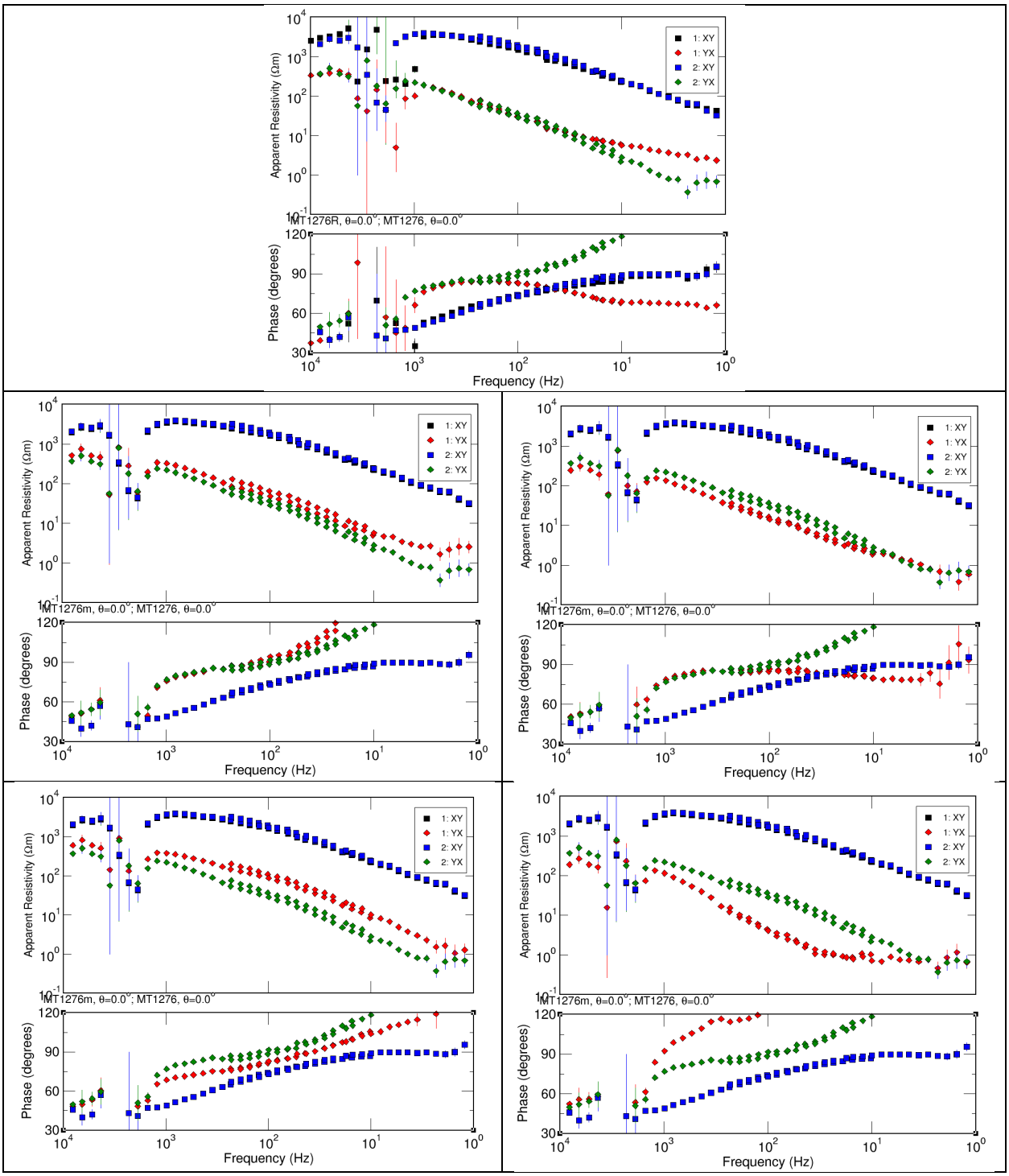

Figure 46: Top row: Repeat data ("1") compared to Original data ("2"). Middle row: Ex misalignment by -15° (left) and +15° (right). Bottom row: Hy misalignment by -15° (left) and +15° (right). Misaligned off-diagonal impedances XY and YX in "1" and original data in "2".

A misalignment of one single channel will not reproduce the differences seen between the original and repeat data – we need to misalign more than one sensor to reproduce the observed effect. However, if we allow multiple channels to be misaligned, we begin to replicate

the differences; below is an example with Ex misaligned by +15°, Ey = 0°, Hx = +15° and Hy = -15° (Figure 47).

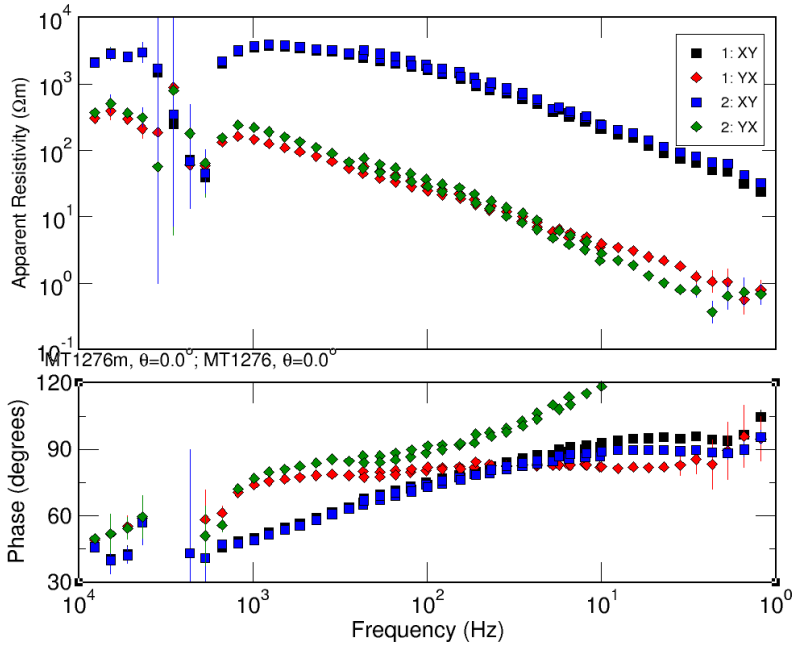

Figure 47: Left: Ex misalignment by +15 °Ey = 0 °, Hx = +15 °and Hy = -15 °. Misaligned off-diagonal impedances XY and YX in "1" and original data in "2".

➔ Simulation of multi-channel misalignment can reproduce the principal features of the differences observed between original and Repeat occupations. This is consistent with the contractor's description of difficult magnetic-rock conditions, and MTGS considers it a plausible mechanism among others. MTGS does not exclude alternative explanations.

10.1.4. *Which EDI to pick?*

Given these issues, it is difficult to know which EDI file to pick as the "correct" one of each of the pairs. Certainly from a quality perspective, the original estimates are generally superior to the Repeat estimates. But there are other issues described above. I choose the following of the pairs (R denotes Repeat kept, no R means original kept):

MT1187	MT1195	MT1207R	MT1262	MT1264
MT1265R	MT1273R	MT1274R	MT1275	MT1276

This choice was primarily based on the file with the superior QF factor.

10.2. High frequency RhoXY and RhoYX do not asymptote

It is curious that the highest frequencies of RhoXY and RhoYX differ at many sites. Given the short inductive scale length – 10,000 Ωm at 10 kHz yields a skin depth of just 500 m – RhoA in both orthogonal directions should be nearly identical. Instead, what we see is systematic

differences, with RhoXY in almost every case larger than RhoYX, and PhaXY smaller than PhaYX (Figure 48).

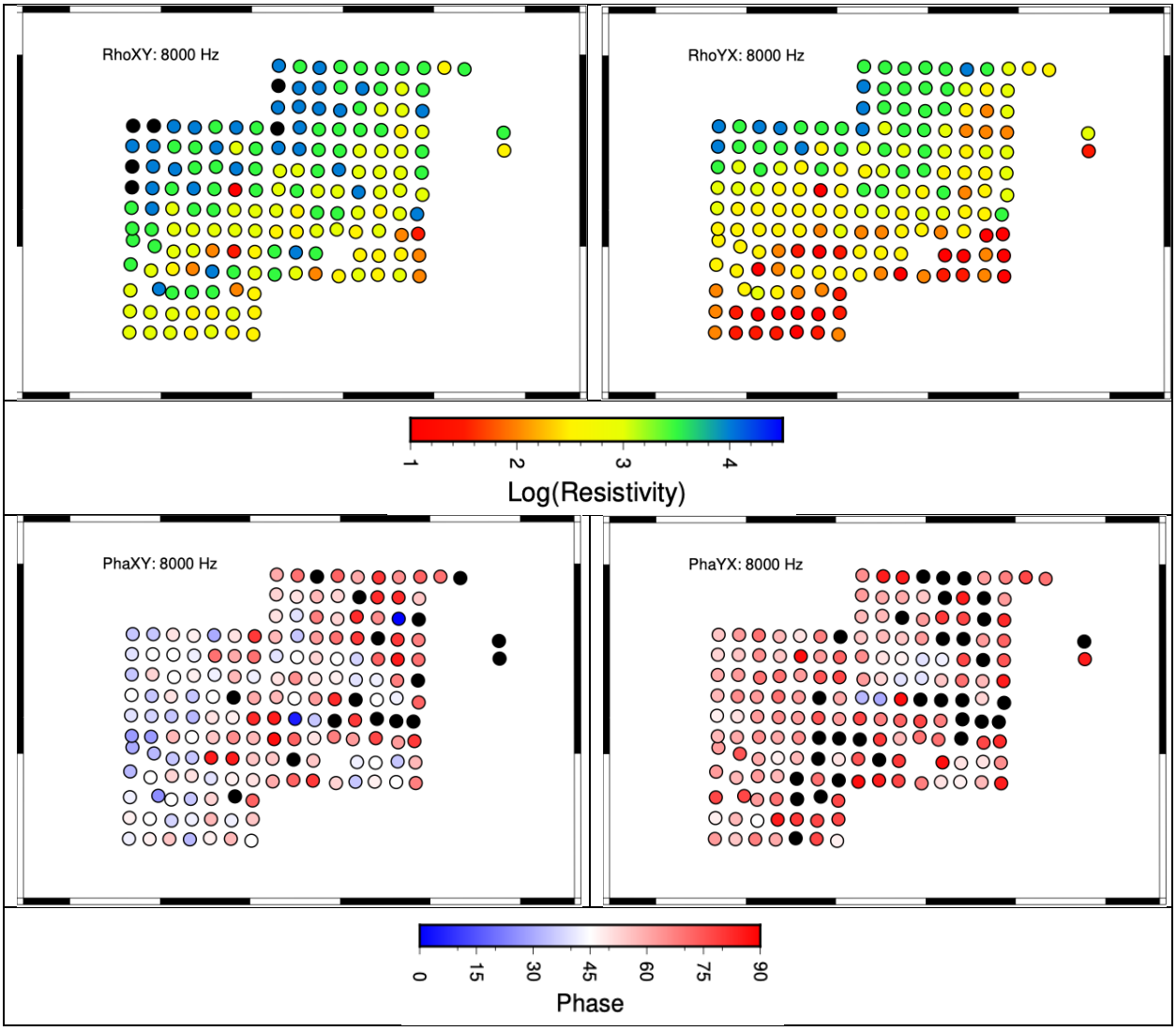

Figure 48: RhoXY, RhoYX, PhaXY and PhaYX values at 8000 Hz.

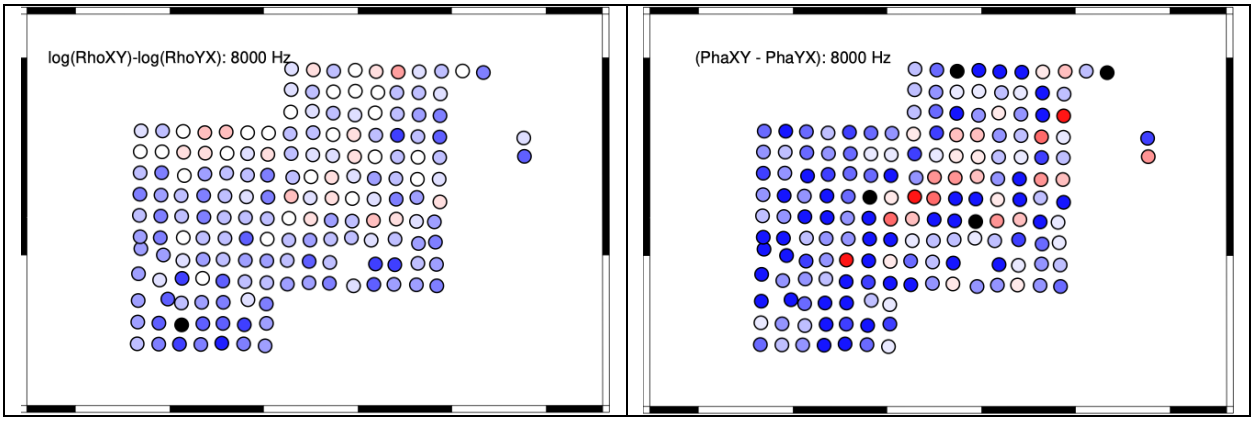

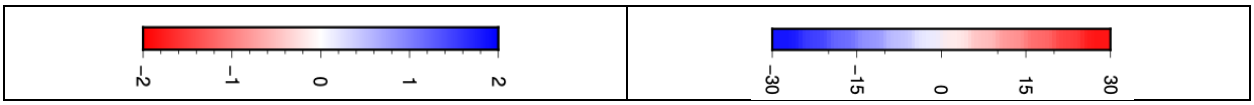

Figure 49: RhoA and Pha XY-YX differences at 8000 Hz.

The differences between the two orthogonal directions are plotted in Figure 49, and there is a clear systematic spatial difference with RhoXY > RhoYX, and PhaXY < PhaYX over almost the whole grid. The average difference in log(RhoA) is +0.6, which is a factor of 4, i.e., the RhoXY values are on average a factor of 4 greater than the RhoYX values at 8,000 Hz.

Several non-exclusive interpretations are consistent with this observation. Among them: a discrepancy between the recorded and deployed e-line length (most deployed lengths are +Y=50 m and -Y=50 m, and a recorded value of 0 m for one of these would produce a factor-of-four effect in RhoYX and RhoYY); an unrecorded factor-of-two gain difference; or another acquisition-side effect. The data examined here do not allow these alternatives to be distinguished, and MTGS makes no finding as to which is in fact the cause.

The data were corrected to a self-consistent state using an industry-standard method (anisotropy correction), not that a specific field error was found and fixed.

11. Average RhoA/Pha curves

To get a sense of the average resistivity structure, the RhoA and Pha curves from all sites were averaged to give the averaged XY and YX curves.

These averaged curves are plotted in Figure 50 (left), and are transformed from periods into the approx. depths, using the Niblett-Bostick transformation [*Jones*, 1983], in Figure 50 (right, only depths to 2,000 m plotted).

The first thing to note is the parallelism of the RhoXY and RhoYX curves at high frequencies >10 Hz. The PhaXY and PhaYX phase curves coalesce from 30 Hz to 1,000 Hz. There is then a strange increase in PhaYX at high frequencies >1 kHz that is not consistent with the RhoYX curve.

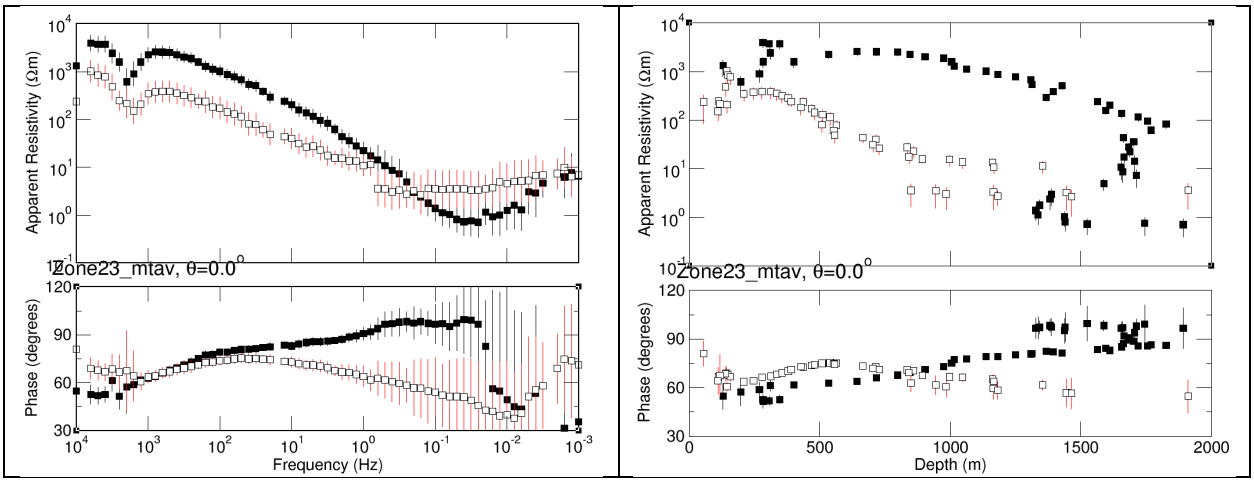

Figure 50: Averaged curves for all sites from Zones 2-3. Left: In frequency. Right: In approx. depth.

Plotting the RhoXY/RhoYX ratio as a function of frequency (Figure 51) we see that the factor of 4 deduced at 8,000 Hz is not the average ratio. The average ratio is best given in the frequency range of 800 Hz – 200 Hz, and is 6.6 $\pm$ 0.14, which means an e-field difference of 2.5 that is hard to explain.

➔ There is no ready explanation for this consistent (RhoXY – RhoYX) difference across the array.

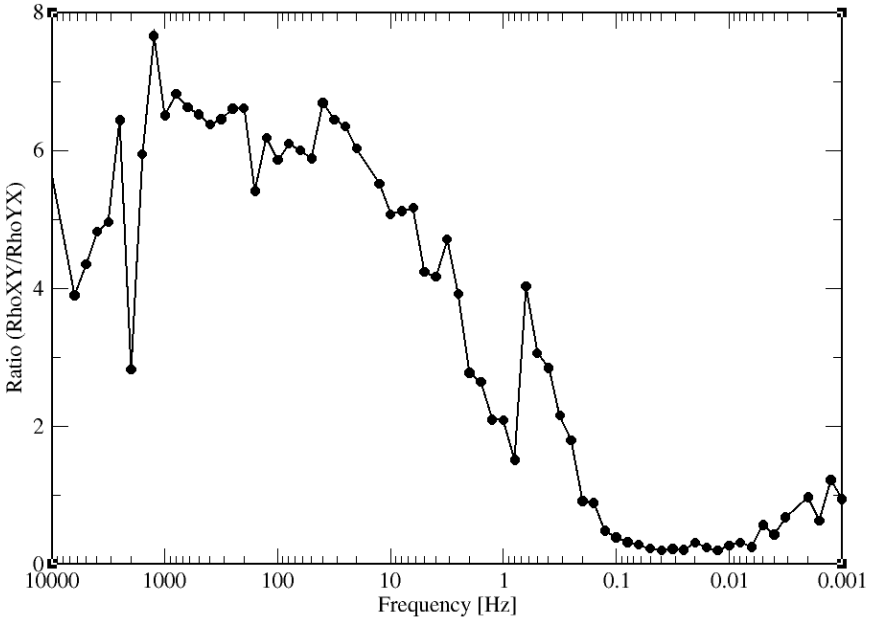

Figure 51: Ratio of RhoXY/RhoYX for the averaged data shown in Figure 50.

11.1. Frequency Band for Depths of Interest

Based on Figure 50 we can define the frequency band for optimally illuminating structures at the primary depths of interest. These are defined as 400 m – 1400 m below surface (Daryl Ball,

email of 2nd December, 2020). Given that the average elevation of the area is 577 ±20 m, this means that in terms of depth below sea level (bsl) these depths correspond to -177 m and 823 mbsl, rounded to -200 m and 850 mbsl.

We can examine skin depth penetration by mode (XY and YX) and by frequency to give us first-order information about sensitivity to various depths (Figure 52, depths are metres below sea level, mbsl). The white region in the plots indicates the depths of primary interest, and light green and light red are 200 m above and below those depths.

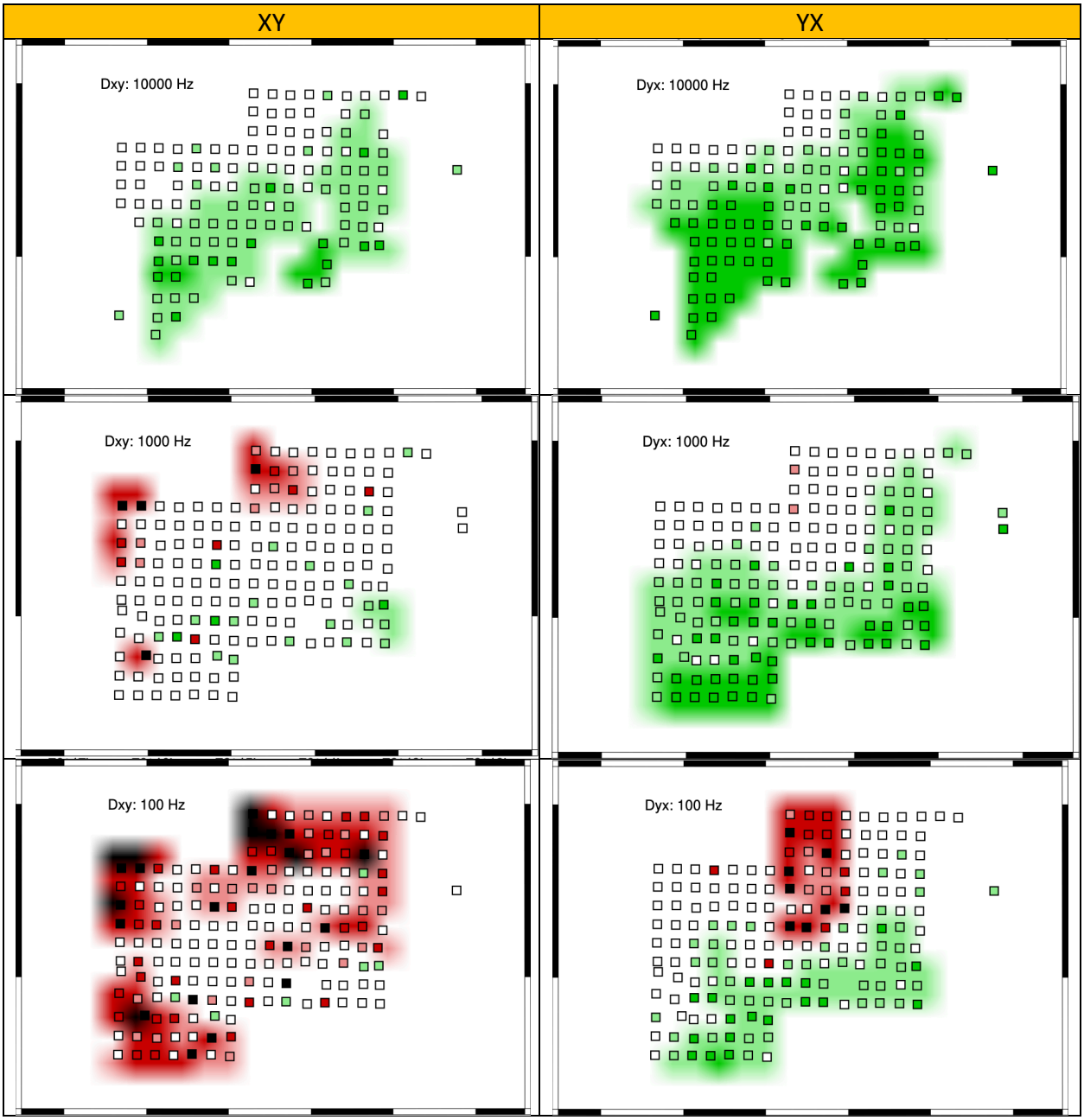

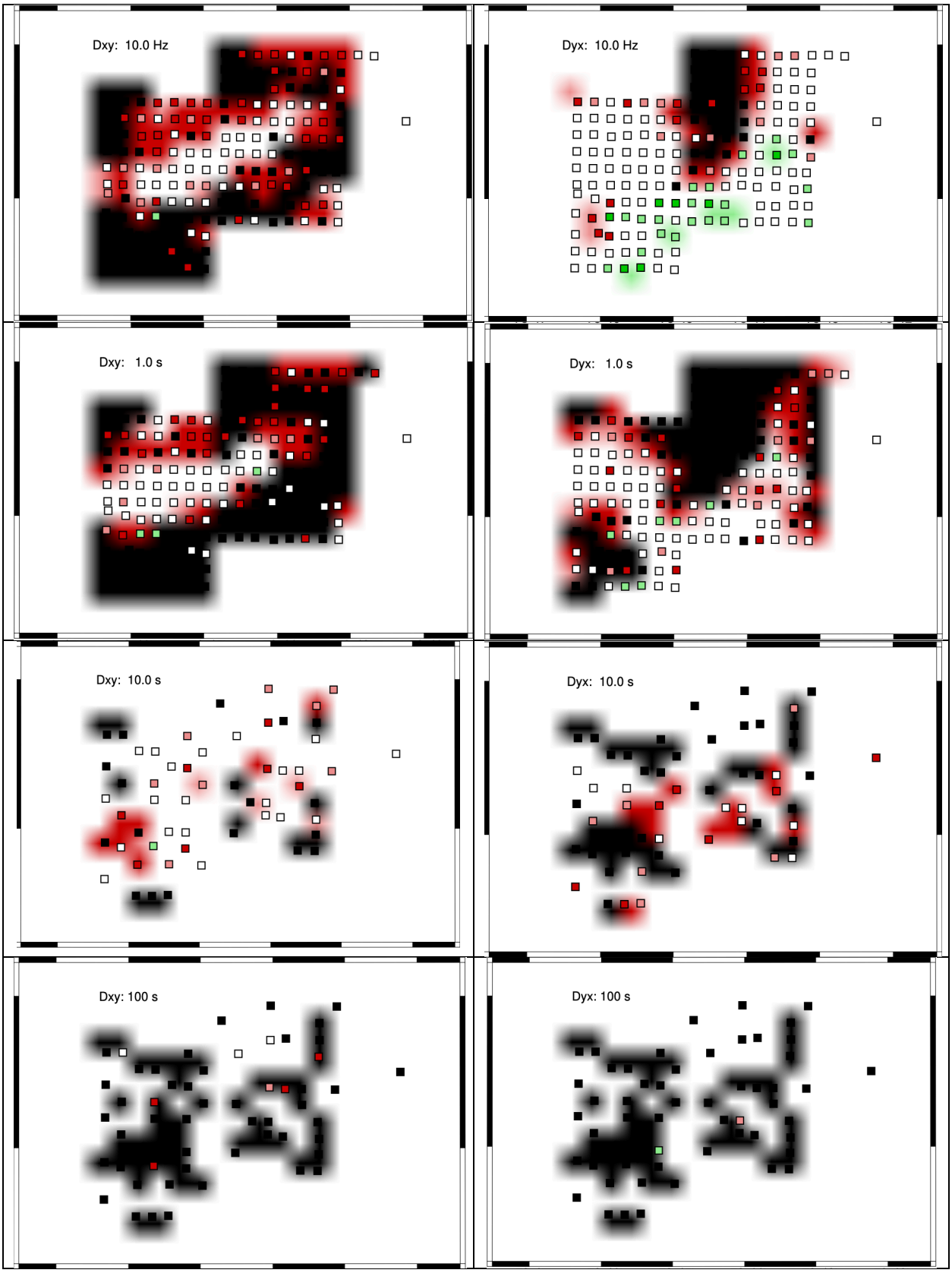
Dxy: 10.0 Hz
Dyx: 10.0 Hz
Dxy: 1.0 s
Dyx: 1.0 s
Dxy: 10.0 s
Dyx: 10.0 s
Dxy: 100 s
Dyx: 100 s

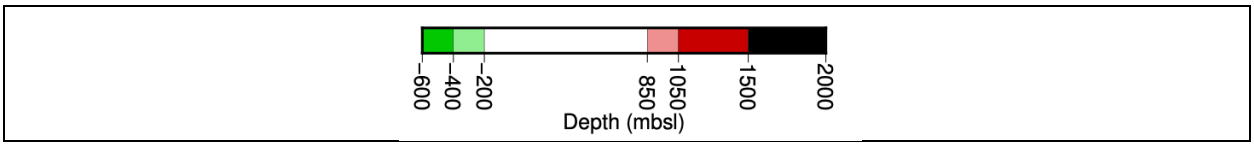

Figure 52: Skin depths for Zxy (left) and Zyx (right) data at frequencies/periods of 10 kHz (top), 1 kHz (2nd row), 100 Hz (3rd row), 10 Hz (4th row), and 1 s (bottom row).

The histograms of the skin depth penetrations are shown in Figure 53; the red region denotes the primary depths of interest.

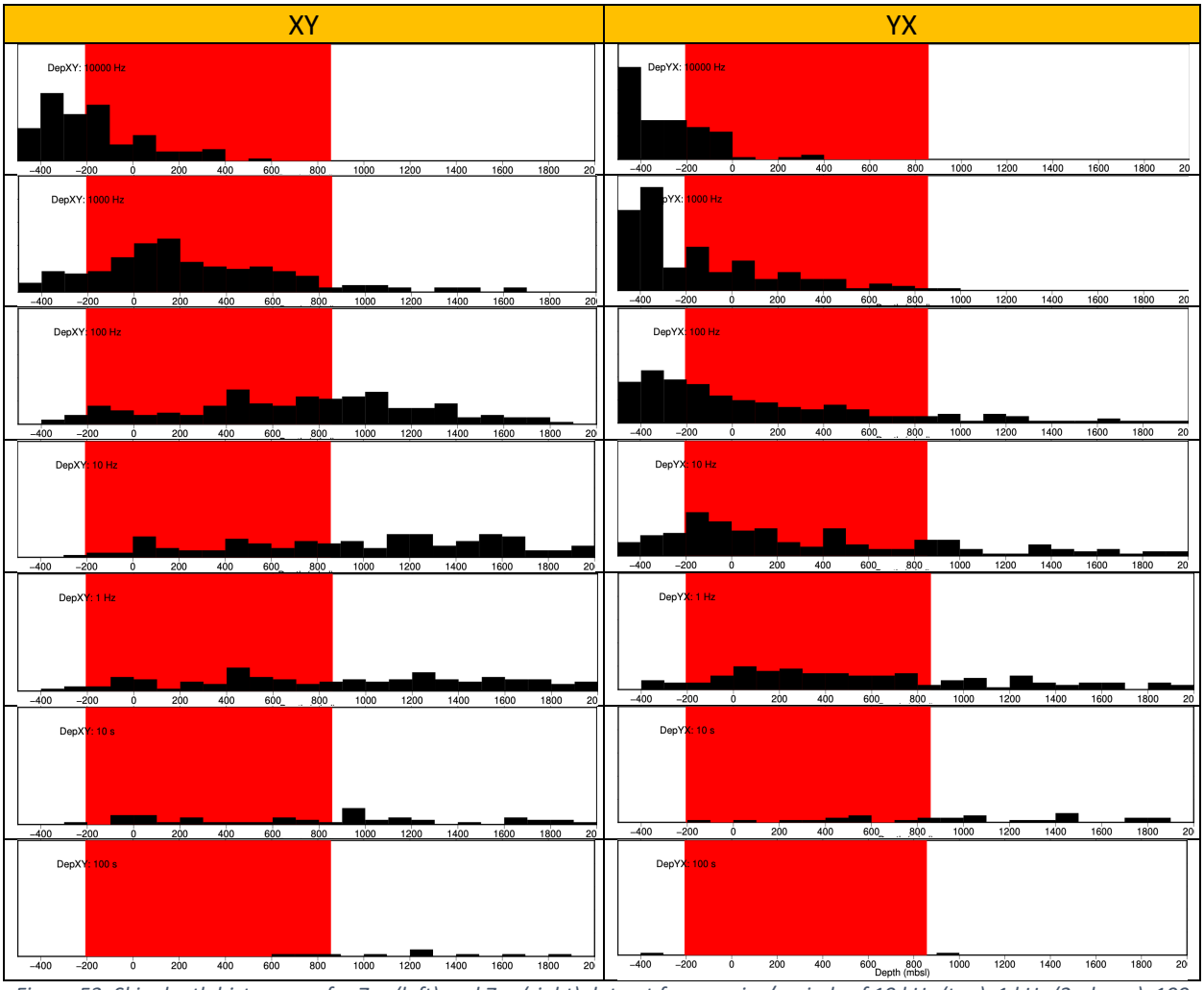

Figure 53: Skin depth histograms for Zxy (left) and Zyx (right) data at frequencies/periods of 10 kHz (top), 1 kHz (2nd row), 100 Hz (3rd row), 10 Hz (4th row), and 1 s (bottom row). The red region is the primary depths of interest.

Clearly to obtain optimum information of the depths of interest we need to consider all of the data in the five-decade band from the highest frequency of 10 kHz down to 0.1 Hz (10 s period).

The frequencies needed for those depths, based on Niblett-Bostick transformation from frequency to depth [*Jones*, 1983] for Zxy and Zyx impedances are shown in Figure 54, and in histogram form in Figure 55.

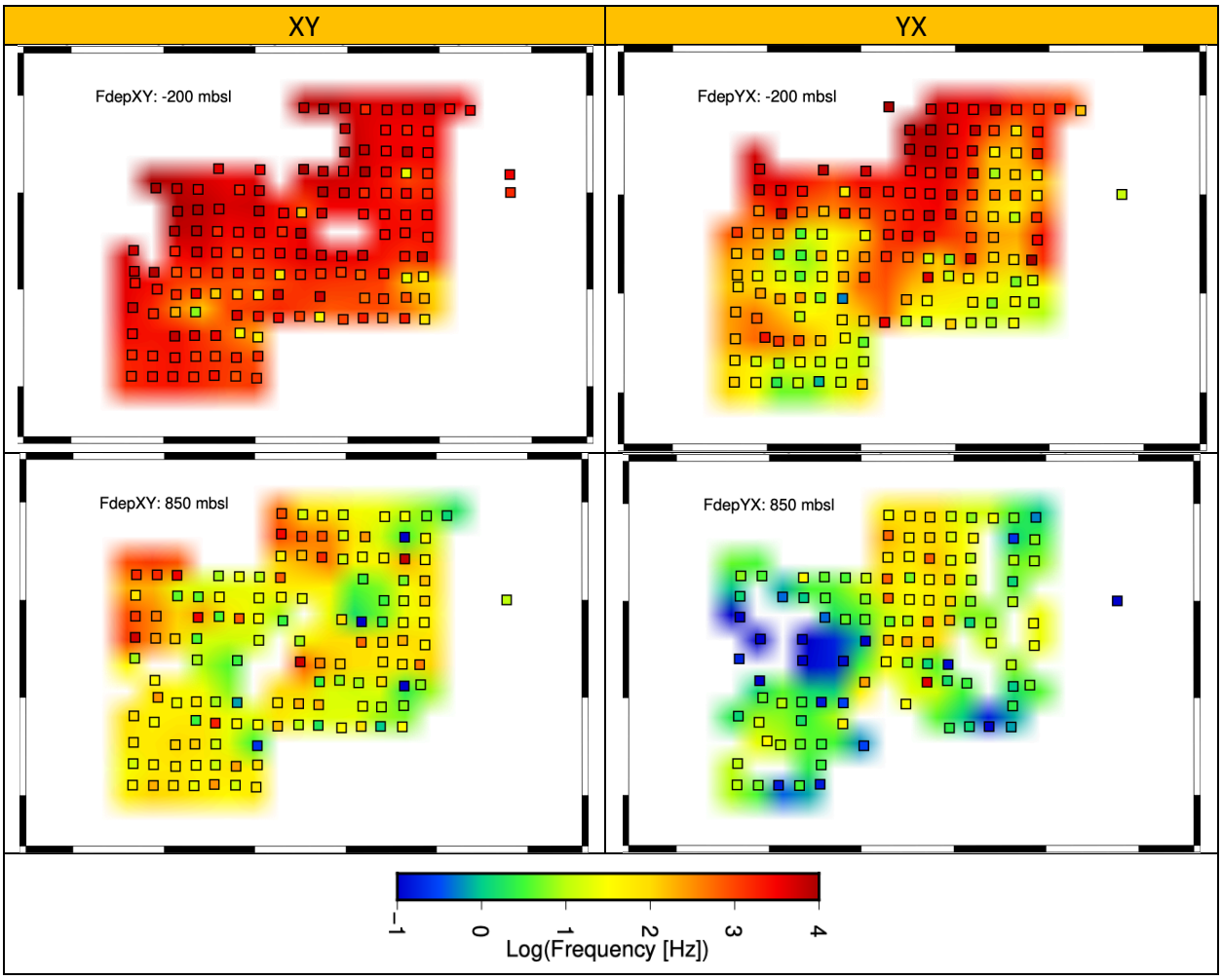

Figure 54: Frequencies required for an NB depth of -200 m (top row) and +800 m (bottom row).

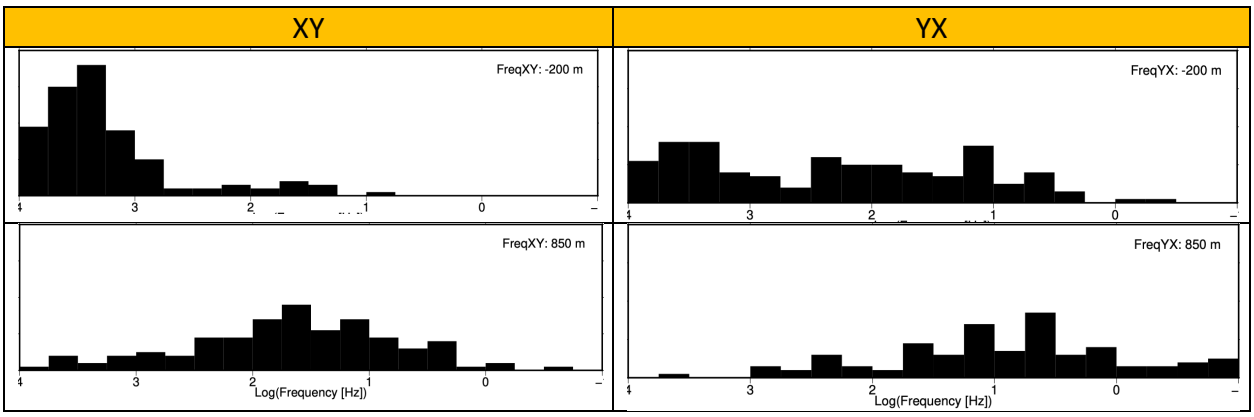

Figure 55: Histograms of frequencies required for an NB depth of -200 m (top row) and +800 m (bottom row).

We can conclude from this frequency/depth analysis that we need to consider a wide range of frequencies from 10 kHz to at least 1 Hz, and for some sites in the west-central part of the grid down to 0.1 Hz (10 s).

➔ Frequencies to be modelled are from 10 kHz to 1 Hz, and preferably to 0.1 Hz.

This five-decade band covers two deadbands, namely the AMT deadband from 5 kHz – 800 Hz and the MT deadband from 8 Hz – 0.1 Hz. Data are optimally acquired in these deadbands with overnight acquisition and long durations. As 2/3 of the sites were short-duration daytime sites, there will be poor resolution from those sites at depths that are at the top and bottom of the client-defined depths of interest.

12. PROQ effects

The Average PhaXY curve goes out of the 1st quadrant at 1 s (i.e., rises above 90°) and returns to the 1st quadrant at 40 s – this is termed the Phase Roll Out of Quadrant (PROQ) effect in MT.

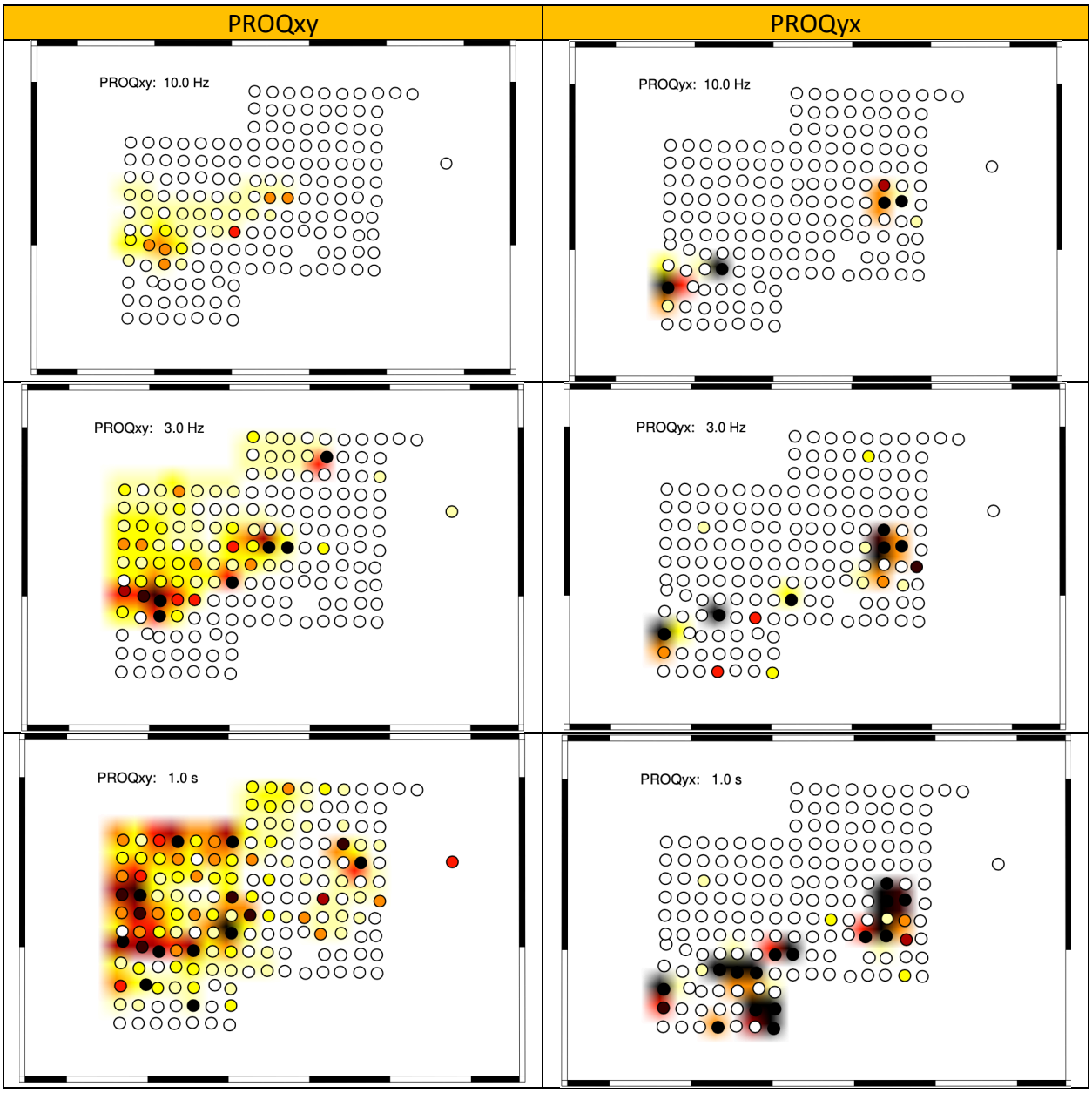

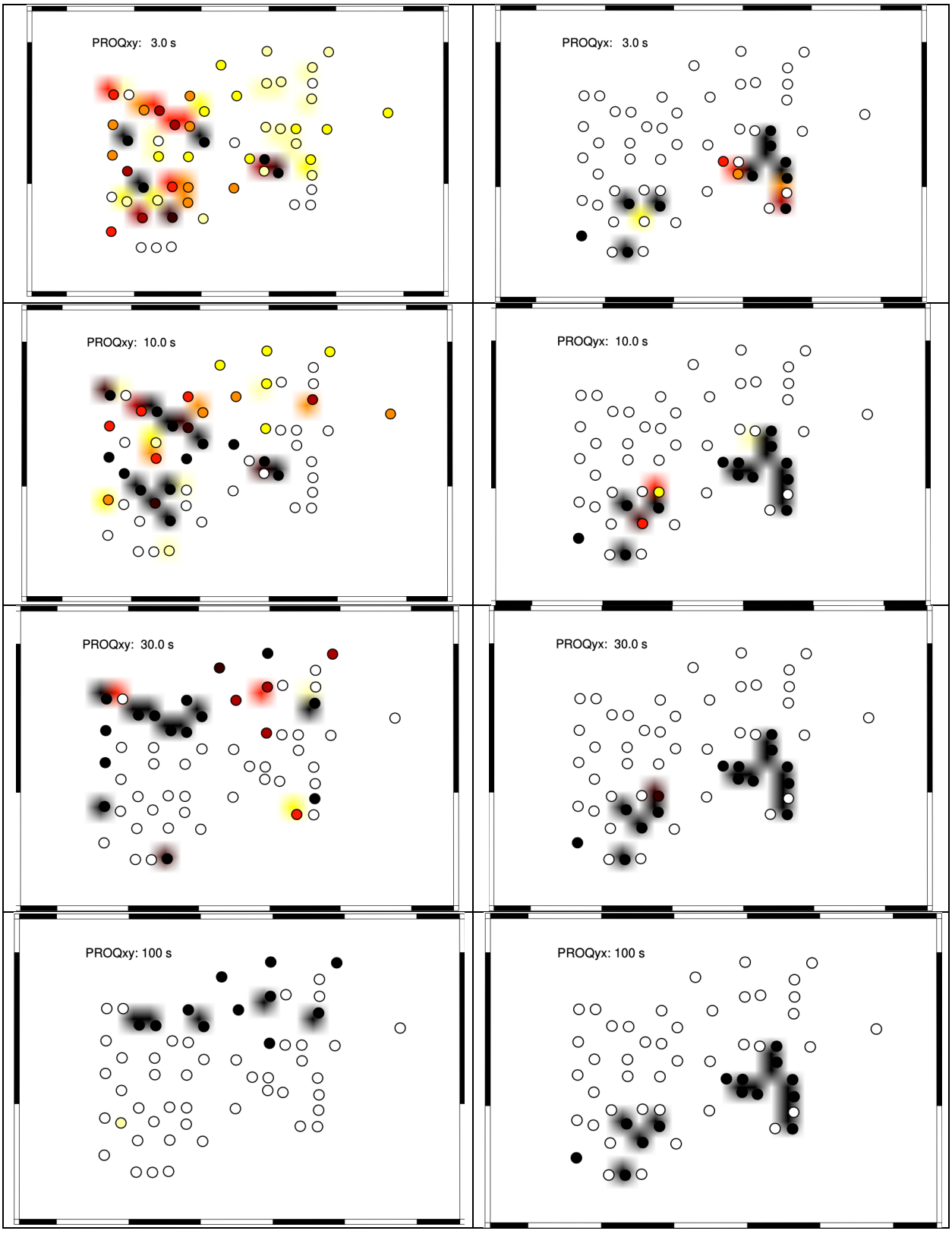
PROQxy: 3.0 s
PROQyx: 3.0 s
PROQxy: 10.0 s
PROQyx: 10.0 s
PROQxy: 30.0 s
PROQyx: 30.0 s
PROQxy: 100 s
PROQyx: 100 s

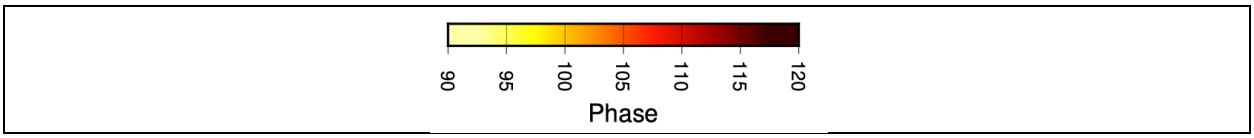

Figure 56: PROQ for PhaXY (left) and PhaYX (right) at frequencies/periods of 10 Hz, 3 Hz, 1 s, 3 s, 10 s, 30 s, and 100 s.

This was also noted as a systematic effect for almost all sites in Raglan Zones 5-8 (report CMTS-2020-Glencore-1-R2).

Plotting PROQs for the PhaXY and PhaYX data in Figure 56 we see that the PROQ initiates in PhaXY at around 10 Hz with a few sites to the SW, then grows in strength and lateral effect. Below 1 Hz (i.e., beyond 1 s) there are far fewer stations with data as these are the overnight sites. The PROQ for PhaYX appears to be more scattered, and is likely to be noise and/or distortion effects. These will be examined later.

13. Quality Factor plots

13.1. Description

Currently, there is no accepted way in the MT community of quantitatively assessing the quality of MT response curves. Generally, curves can be rated on a 5-point qualitative scale from excellent (1) to good (2) to average (3) to poor (4) to unusable (5) on visual inspection. However, the response estimates usually vary in their quality with period – data in the AMT deadband (5 kHz – 800 Hz) and the MT deadband (8 Hz – 0.1 Hz) are often far poorer than neighbouring data, especially if acquisition was in the daytime only. The lowest frequency/longest period data can also be poor due to insufficient recording times, non-uniform source fields, lack of source field energy (=low sunspot number), etc.

The quality of the RhoA and Pha curves is basically a function of the smoothness of the curves, i.e., point to point consistency, and the errors associated with the estimates. Smooth XX, XY, YX and YY curves that have consistent errors such that small scale scatter of the estimates lies within small errors are desirable. To undertake quantitative assessment of quality, and to automate the process of poor data identification, I have devised an objective "Quality Factor" of the XY and YX curves that is a combination of a measure of smoothness and a measure of error. Note that I cannot apply this approach to the XX and YY curves.

The **Average Quality Factor** is given by **QFav = SQRT(QFxy * QFyx)**

Quality Factors will be of order 1 for high quality data, and QF increases with decreasing quality of data.

13.2. Plots

Plotted are two sets of SF, EF and QF maps for each of five frequency/period bands, one set without adopting an error floor, so using the errors in the data (Figure 57), and the other set with an assumed error floor of 2° in phase/7% in apparent resistivity (Figure 58), which is fairly standard in the MT community to assume we cannot get data to better than these floors, especially in as challenging environment as the Raglan field area (see Figure 4).

The frequency/period bands are:

1) 10 kHz – 1,000 s: these 7 decades cover all of the frequency range of the contract. Note that the daytime sites only acquired data to 1 Hz.
2) 10 kHz – 1 kHz: this decade covers the AMT deadband. Overnight acquisition gives the best chance of high quality data in the AMT deadband [*Garcia and Jones*, 2002]. About 1/3 of the 2017 sites were overnight, whereas about 2/3 were daytime only.
3) 1 kHz – 10 Hz: these two decades are usually the best quality data in an AMT survey.
4) 10 Hz – 10 s: these two decades cover the MT deadband. Overnight acquisition is usually required to ensure high quality data in this band. For the daytime sites the estimates only go to 1 Hz.
5) 10 s – 1,000 s: these are the deepest penetrating decades. To ensure good data beyond 100 s it is usual to have two nights of acquisition.

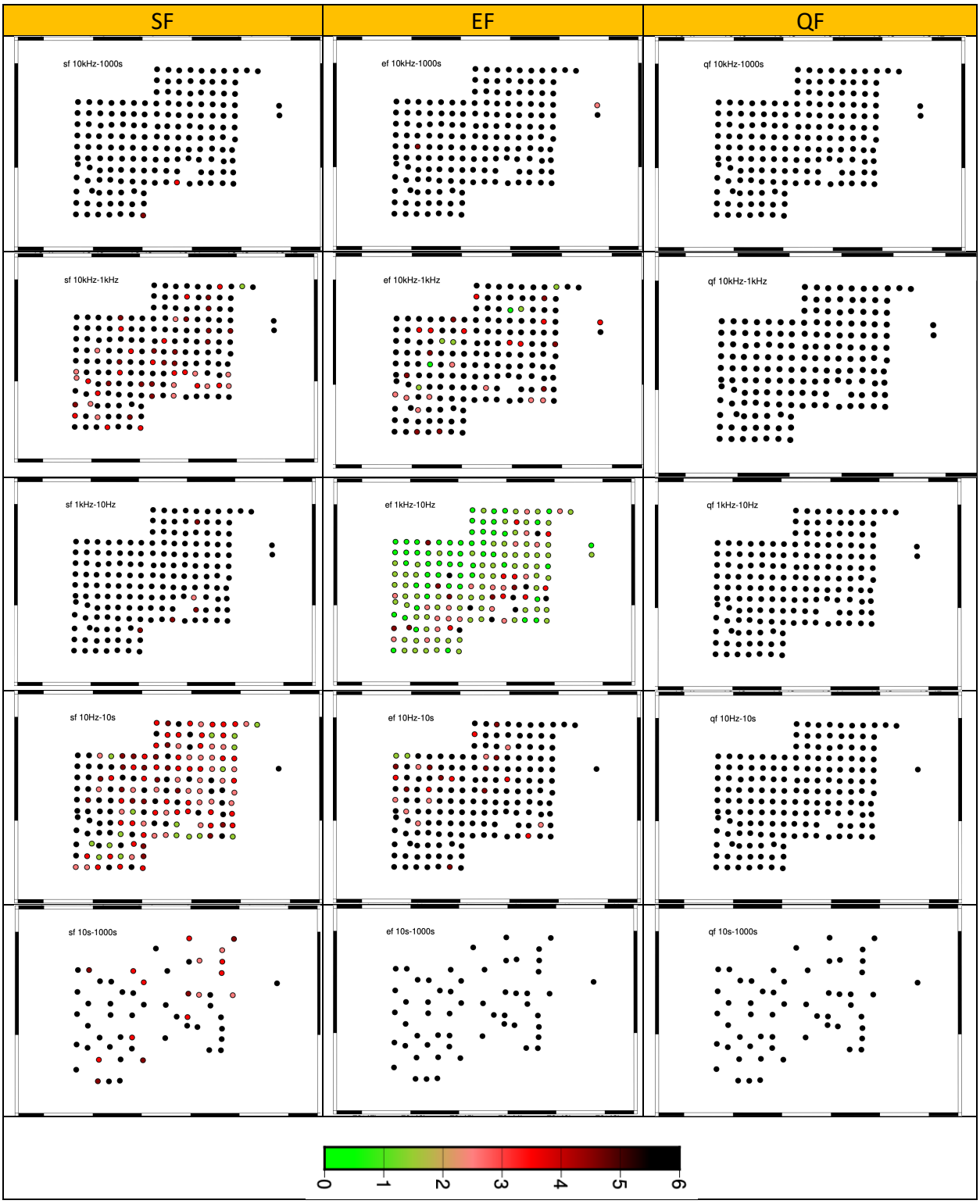

Figure 57: Maps of the Smoothness Factor (SF, left column), Error Factor (EF, centre column) and Quality Factor (QF, right column), for frequency/period bands of 10 kHz – 1,000 s (top row), 10 kHz – 1 kHz (2nd row), 1 kHz – 10 Hz (3rd row), 10 Hz – 10 s (4th row), and 10 s – 1,000 s (bottom row), without adopting an error floor. The EFs here are the actual average PhaXY and PhaYX phase errors in the frequency band.

Clearly the error estimates are too low – this is reflected in the poor SFs. The SF maps all exhibit very high nRMS misfits of the Rho^{+} model curve to the data. As the nRMS is normalized by the error estimates, this implies that the error estimates are too small. The best average phase error estimates are in the range 1 kHz – 10 Hz, but at <0.25° are lower than is realistic for data of this type in this environment.

The QF maps, which are the multiple of SF and EF, imply low data quality, but this result is driven by the small magnitudes of the delivered errors rather than by the data themselves.

Assuming a 2°/7% error floor in Pha/RhoA respectively, the maps are very different and are far more reasonable and believable (Figure 58).

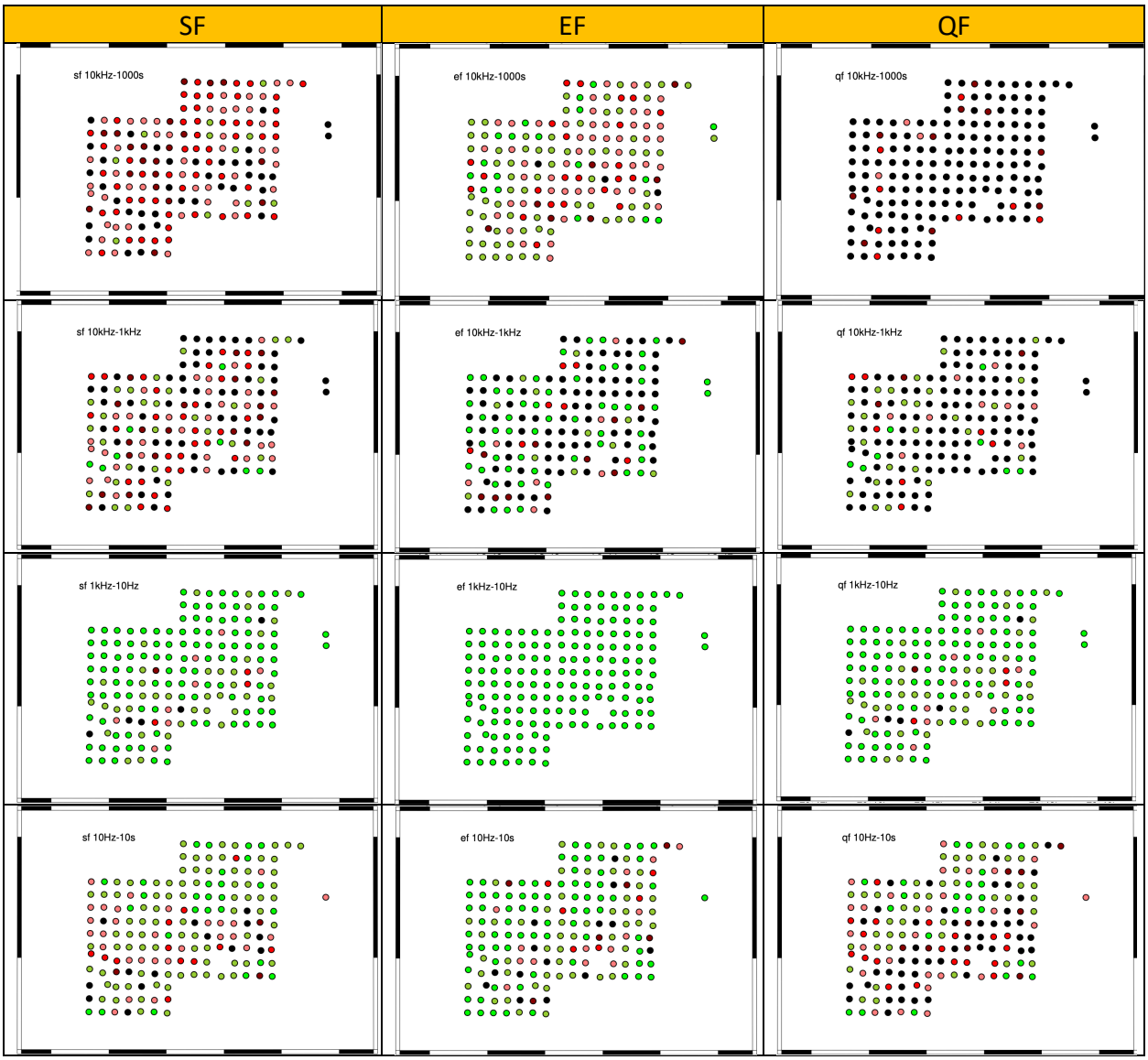

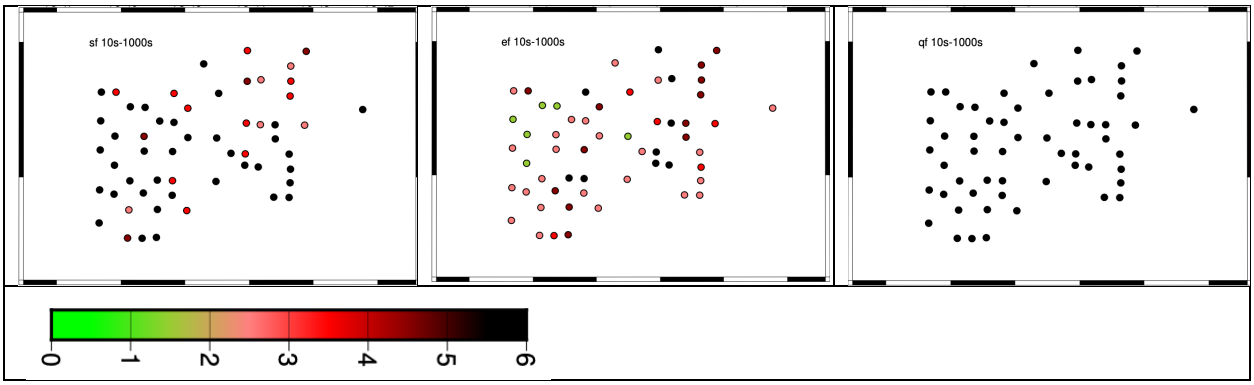

Figure 58: Maps of the Smoothness Factor (SF, left column), Error Factor (EF, centre column) and Quality Factor (QF, right column), for frequency/period bands of 10 kHz – 1,000 s (top row), 10 kHz – 1 kHz (2nd row), 1 kHz – 10 Hz (3rd row), 10 Hz – 10 s (4th row), and 10 s – 1,000 s (bottom row), for an adopted error floors of 2 ° in Pha and 7% in RhoA. The EFs here are the average PhaXY and PhaYX phase errors in the frequency band.

Looking at these maps we can draw the following conclusions:

- Quality is limited in the AMT deadband (10 kHz – 1 kHz), which is somewhat unexpected given that one third of sites were acquired overnight.
- There is generally excellent quality data in the 1 kHz – 10 Hz band. QFs for the most part are less than 2 (light green and dark green).
- Data quality in the MT deadband of 10 Hz – 10 s (0.1 Hz) is good at some sites, but the daytime sites only have data to 1 Hz so the image is biased somewhat. Generally though the QFs are >2 even at overnight sites; this may be due to using metal plates for electrodes, or may be due to low source strength.
- Data quality at the longest periods (10 s – 1,000 s) is generally not usable, with QFs > 6 at all sites. Given the acquisition time of the overnight sites and that the Phoenix Low Frequency coils were used, the most likely contributor to the reduced quality at these periods is the use of metal-plate rather than non-polarizing electrodes, or that natural signal was too low.
    - Note that some of the large SFs will come from PROQ effects, and those sites with dominant PROQ effects can be seen in Figure 56.

14. Qualitative Dimensionality Analysis – Phase Tensors

I perform a qualitative dimensionality analysis on the data to determine whether 1-D and 2-D interpretation methods can be applied, or we must use 3-D methods. For this I plot the Phase Tensors.

For two-dimensional (2-D) structures, the along-strike e-field (Ex, where “x” is defined as being along strike – Note: in Quantec’s deliverables “x” is defined along the profile rather than along strike; this convention has been respected in the analysis) divided by the across-strike h-field

(Hy, "y" is across strike) is defined as the transverse-electric (TE) mode [3] of induction in MT. In contrast, the across-strike e-field (Ey) divided by the along strike h-field (Hx) is defined at the transverse magnetic TM mode.

It is vitally important that the correct geoelectrical strike be defined for 2-D data – an incorrect strike direction will lead to erroneous models, and thereby erroneous interpretations and conclusions.

A rapid visual way for assessing dimensionality and directionality is to plot the MT Phase Tensors [*Caldwell et al.*, 2004]. The great attraction of Phase Tensors (PT) is that for perfect error free data then local galvanic distortion caused by near-surface inhomogeneities of no interest is removed, and only directionality and dimensionality of the Earth structure is qualitatively indicated.

However, as discussed by *Jones* [2012], Phase Tensors should only be used in a qualitative manner; for quantitative assessment then more sophisticated approaches must be adopted. One major problem with Phase Tensors is that they use the data without any consideration of errors, so in the case of scatter the Phase Tensors will be inconsistent from site-to-site.

*Phase Tensors (PT) at frequencies of 1,000 Hz, 100 Hz, 10 Hz, 1 Hz, 0.1 Hz (10 s) and 0.01 Hz (100 s) are plotted in Figure 60.**Error! Reference source not found.**. Phase Tensors at frequencies of 1,000 Hz (top left), 100 Hz (top right), 10 Hz (middle left), 1 Hz (middle right), 0.1 Hz (10 s, bottom left), and 0.01 Hz (100 s, bottom right). The colours of the ellipses are the phase tensor beta values.*

Low beta values (dark or light blue, <5°) means that the data conform to either a 1-D or 2-D representation of the structure below. High beta values (yellows and reds) indicate that the data are either representative of 3-D structures, OR that the data are scattered and noisy. Note that the estimation of PT values is from algebraic manipulation of the MT impedance tensors, and so is totally non-robust and is highly sensitive to even minor amounts of noise.

The shape of the ellipses indicates whether the data are 1-D, which is true if the ellipse is near circular, or 2-D for low beta. If 2-D then the geoelectric strike direction is represented by the major or minor axis, depending on whether the site is on or off a conductor.

[3] In 2D Maxwell's Equations separate into two independent sets. One set describes electric currents travelling along the structures, and is called the TE mode. The other set describes electric currents travelling perpendicular to structures, and is called the TM mode. Essentially, the TE mode is responsive to current flow, whereas the TM mode is responsive to charge distribution. Hence, the two sense the subsurface resistivity distribution differently, and a joint inversion of both TE and TM mode data together is a true Joint Inversion in an inversion manner as the two trade-off against each other.

- Some of the ellipses are dark to light blue, which indicates very low to low PT absolute skew (|β|) below 5°, especially at high frequencies. For those sites an assumption of 1-D or 2-D dimensionality is valid.
- Then for some sites however, particularly at lower frequencies, |β| values rise to 5°-10° (green), which is an indication of either weak 3-D structures being sensed at those depths or of noisy data.
- For quite many sites |β| values are 10°-20° (yellow), which is an indication of stronger 3-D effects that need to be taken into account and possibly invalidates 2-D models of that area.
- Those sites that show very high PT skew, red, with very narrow ellipses are clearly from noisy data as they are inconsistent with their neighbours.

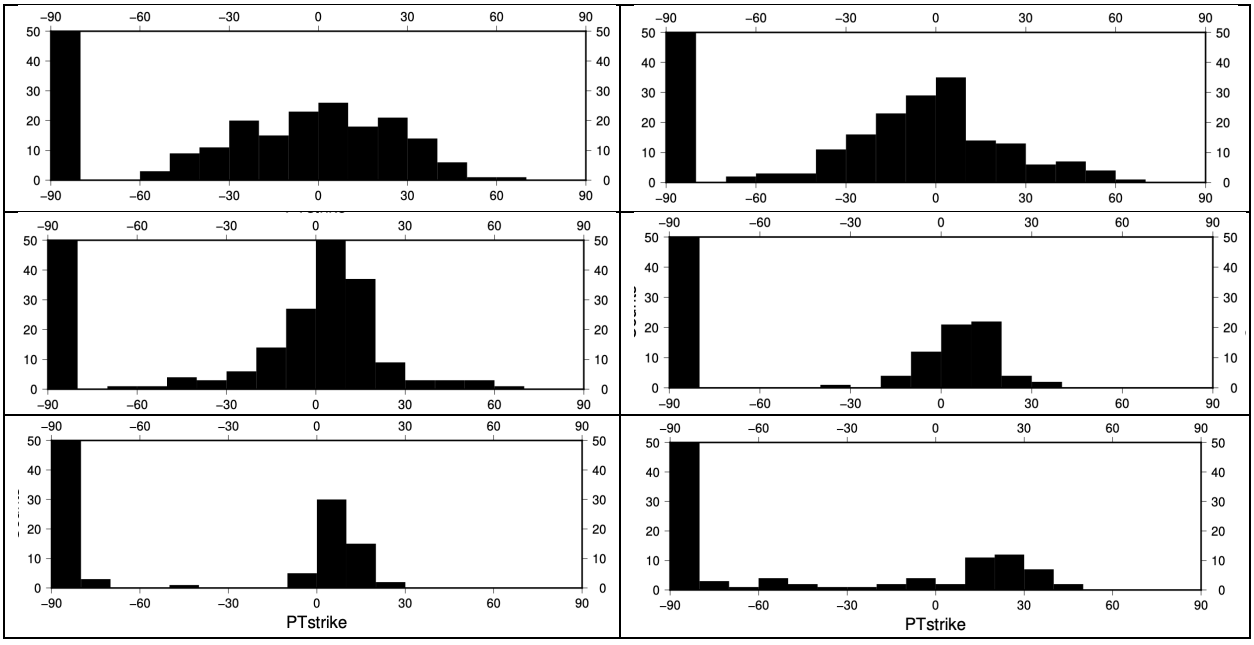

Figure 59 : Phase Tensor strike histograms at frequencies of 1 kHz (top left), 100 Hz (top right), 10 Hz (middle left), 1 s (middle right), 10 s (bottom left) and 100 s (bottom right).

With regard to geoelectrical strike, histograms of the PT ellipse major axis directions (Figure 59) shows a peak of around 0° at all frequencies from 1 kHz to 10 s, that becomes less defined at lower frequencies (=deeper depths of penetration) of 100 s. This means that a geoelectrical strike of either N-S or E-W [4] is acceptable to most sites for shallower depths, but structures become more 3-D with increasing depth.

[4] Note that the Phase Tensor major axis will "flip" by 90° on either side of a vertical boundary, such as a fault, in exactly the same manner that anisotropy directions flip.

A full quantitative dimensionality analysis using the *McNeice and Jones* [2001] multi-site, multi-frequency distortion dimensionality code "*strike*" is performed below. That analysis will inform us which data can validly be interpreted in 2-D and what the appropriate geoelectrical strike direction is to adopt for each profile.

15. Approximate Resistivity Images

A quickview way of imaging the data is to obtain an approximate resistivity at a given depth using the Niblett-Bostick transform [*Jones*, 1983]. This is done for depths of -200 m, 0 m, 400 m and 850 m BSL (below sea level, which is about 577 m below surface on average), so depths below surface of approx. 400 m, 600 m, 1000 m and 1400 m. The maps for RhoMAX (left) and RhoMIN (right) are shown in Figure 60.

RhoMAX is the maximum resistivity at that depth, and RhoMIN is the minimum resistivity. These values are determined by rotating the data through 90° at each frequency for each site and recording the maximum and minimum resistivities and their directions. Note that these are not necessarily at right angles to one another. Sites are plotted only when both orthogonal directions (XY and YX) reach to the desired depth.

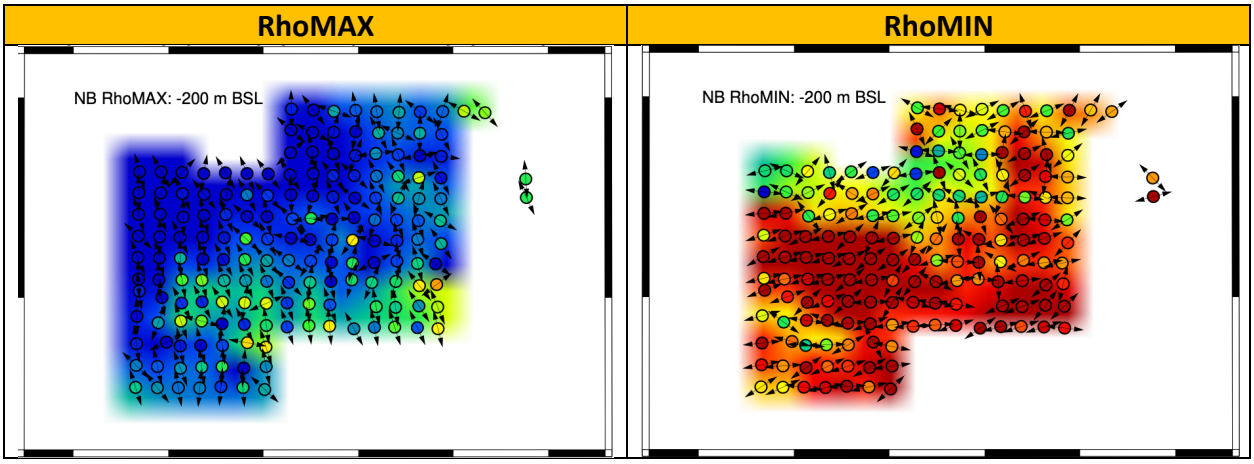

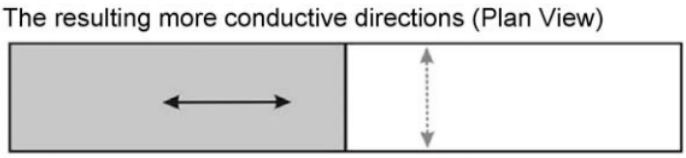

Schematic diagram portraying the MT anisotropy direction for the two quarter-space fault model with the more conductive side shaded grey. On the more conductive (grey) side of the fault, the TM mode apparent resistivity is the more conductive, whereas on the resistive side of the fault the TE mode apparent resistivity is the more conductive. This results in the more conductive directions being parallel to the geological strike on one side of the fault (the resistive side, white), and perpendicular on the other (the conductive side, grey).

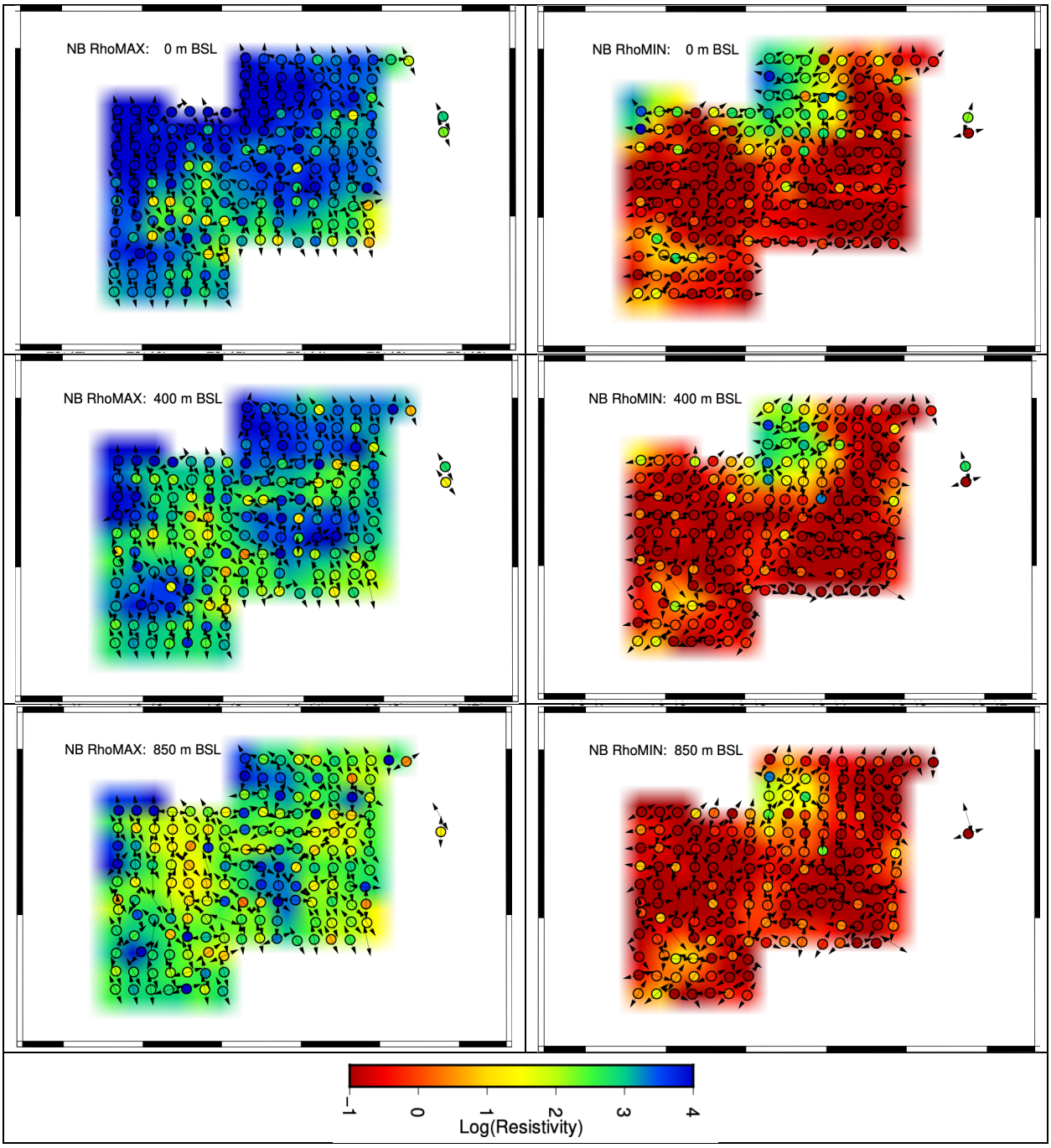

Figure 60: RhoMAX (left) and RhoMIN (right) approx. resistivity maps at depths of -200 m (top row), 0 m (2nd row), 400 m (3rd row), and 850 m (bottom row) below sea level. Note, sites are plotted only when both orthogonal directions (XY and YX) reach to the desired depth.

The actual values at each site are shown by the coloured circles, and the arrows indicate the direction of RhoMAX and RhoMIN respectively. Single site differences with neighbouring sites are a likely sign of galvanic distortion effects that have to be corrected for. The raw estimates have been smoothed using a 2-D median filter of a width of 250 m to produce the colour contour map on each figure.

The histograms of the azimuths of the RhoMAX and RhoMIN directions are shown in Figure 61.

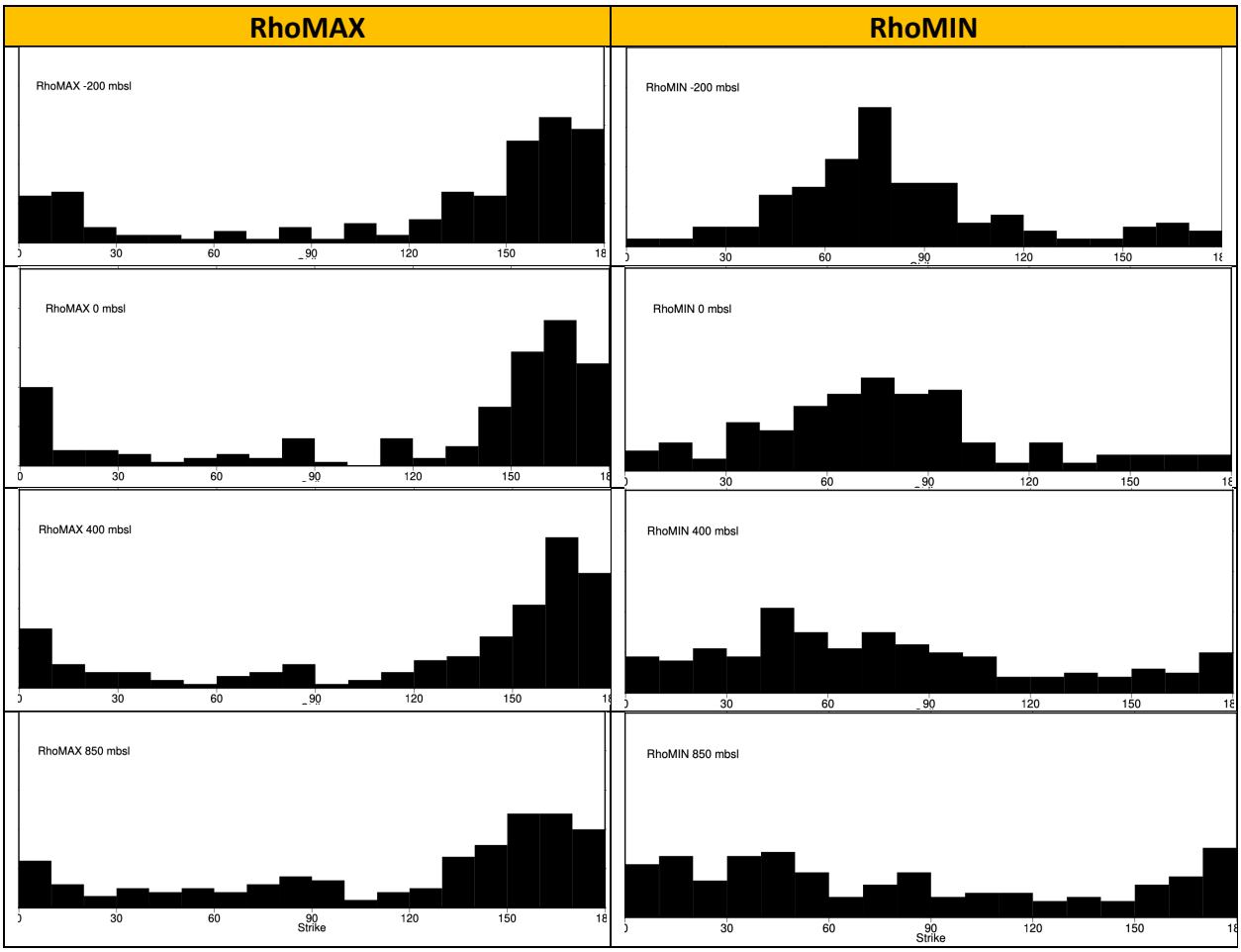

Figure 61: Histograms of the RhoMAX (left) and RhoMIN (right) directions at depths of -200 m (top row), 0 m (2nd row), 400 m (3rd row), and 850 m (bottom row) bsl.

The RhoMAX direction appears to be consistent with depth at NNW-SSE. The RhoMIN direction is well-defined at shallow depths with a direction of ENE-WSW, but becomes more diffuse with depth.

These are however unweighted histograms that do not take the strength of the anisotropy, i.e., RhoMAX/RhoMIN into account. Maps of anisotropy for depths of 500 m, 1000 m, 1500 m and 2000 m are shown in Figure 62. The arrows indicate the RhoMIN direction, and their lengths are the strengths of the anisotropy for depths of -200 m, 0 m, 400 m and 850 m bsl (approx. 400 m, 600 m, 1000 m and 1400 m below surface).

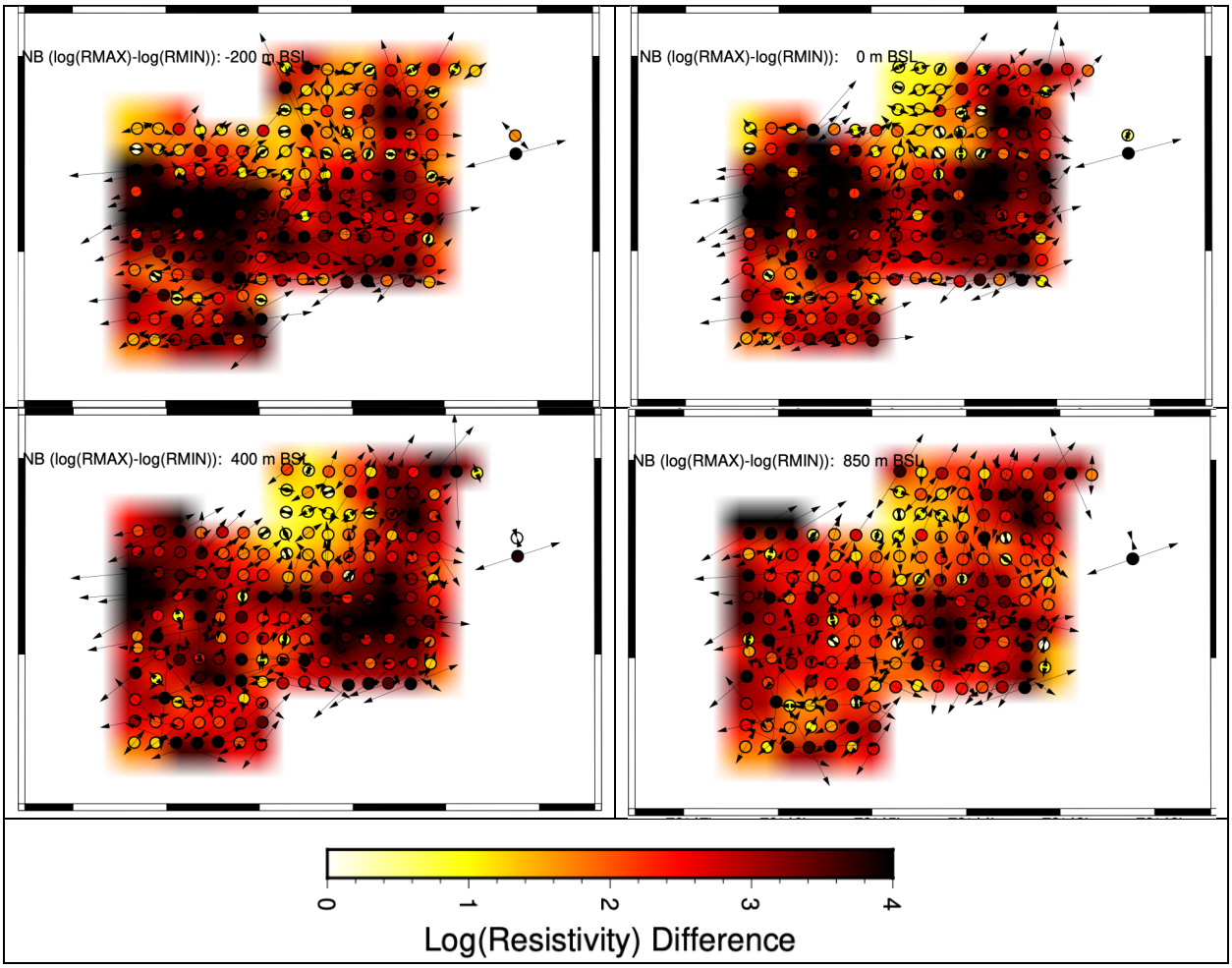

Figure 62: Anisotropy, given by RhoMAX/RhoMIN, for depths of -200 m (top left), 0 m (top right), 400 m (bottom left), and 850 m (bottom right) bsl. Arrows are the RhoMIN direction, and their lengths are the strength of the anisotropy.

Histograms of the RhoMIN directions are plotted in Figure 63, where weights have been applied that are the RhoMAX/RhoMIN anisotropy at each site.

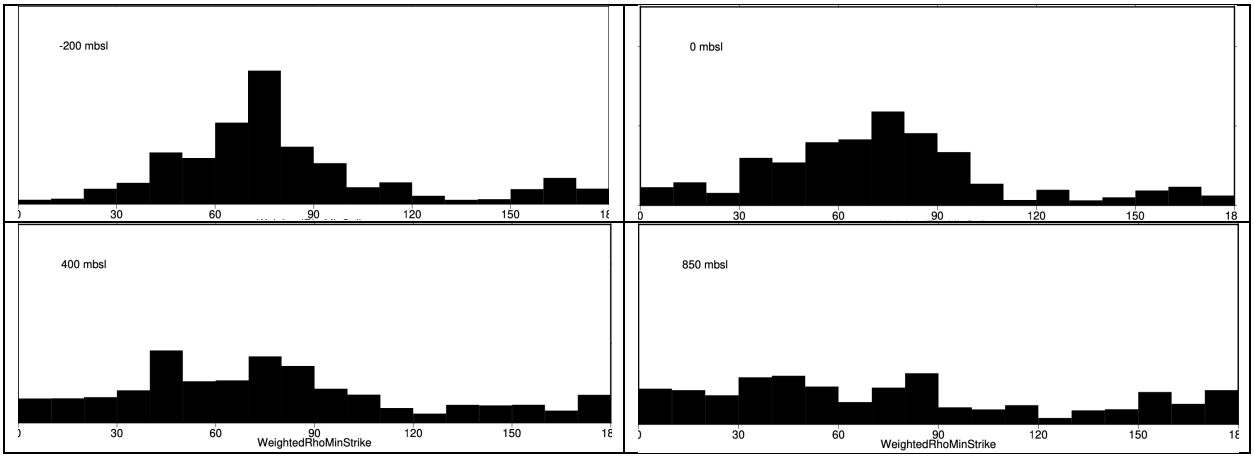

Figure 63: Weighted histograms of the RhoMIN directions at depths of -200 m (top left), 0 m (top right), 400 m (bottom left), and 850 m (bottom right) bsl. Weights are the RhoMAX/RhoMIN anisotropy.

These histograms essentially confirm the prior observation that the upper part of the target zone of interest has a dominant strike direction of ENE-WSW, but the lower part is far more variable. This variation will be examined in detail in the strike analysis.

16. Strike Analysis

The purpose of geoelectrical strike determination is two-fold; first it is to ascertain IF a 2-D model of the data is valid, and second, if a 2-D model is valid then to derive the best strike angle to adopt for 2-D inversion. This has to be performed in a statistical manner to derive the angle that fits the data at most sites and most frequencies.

The most-consistent geoelectrical strike over a series of sites and frequencies is best determined using the multi-site, multi-frequency distortion decomposition code of *McNeice and Jones* [2001], based on the approach of *Groom and Bailey* [1989; 1991]. The primary objective when using any strike approach is to determine the most consistent strike direction acceptable to the majority of sites for the majority of frequencies. The optimum manner to determine that direction is in a stepwise mode, going from single-station to multi-station and from a few frequencies to broad frequency bands, to locate significant departures from uniformity, rather than utilizing all data immediately.

16.1. Single site analyses

First, we run the code in single-site, multi-frequency mode, averaging data in various frequency or depth bands. We assume an error floor [(5)] of 3.5% in impedance throughout; this is equivalent to 7.12% in apparent resistivity and 2° in phase. This floor was chosen based in the Quality Factor analysis above.

16.1.1. *Single-site, multi-bands*

We start by analysing data in decade-wide bandwidths. The geoelectric strike directions for five frequency bands of 10 kHz – 1 kHz, 1 kHz – 100 Hz, 100 Hz – 10 Hz, 10 Hz – 1 Hz, and 1 s – 10 s are shown in Figure 64.

[5] An error floor is the minimum value of the error. Errors that are less than the error floor are increased to the error floor value, whereas errors that are greater than the error floor are unchanged. We routinely adopt an error floor when undertaking data fitting as most error estimates are derived from parametric error estimators, and are known to be far too small (see, e.g. Chave, A. D., and A. G. Jones (1997), Electric and magnetic field galvanic distortion decomposition of BC87 data, *Journal of Geomagnetism and Geoelectricity*, *49*(6), 767-789.).

The lengths of the arrows indicate the phase difference between modes, i.e., the phase in the strike direction minus the phase in the perpendicular-to-strike direction, which is a measure of the strength of the dimensionality. This phase difference is zero for 1-D structures, and is large for strong 2-D or 3-D structures. The colour indicates how well the distortion model fits the data, with green acceptable (nRMS < 2) and red unacceptable (nRMS > 3).

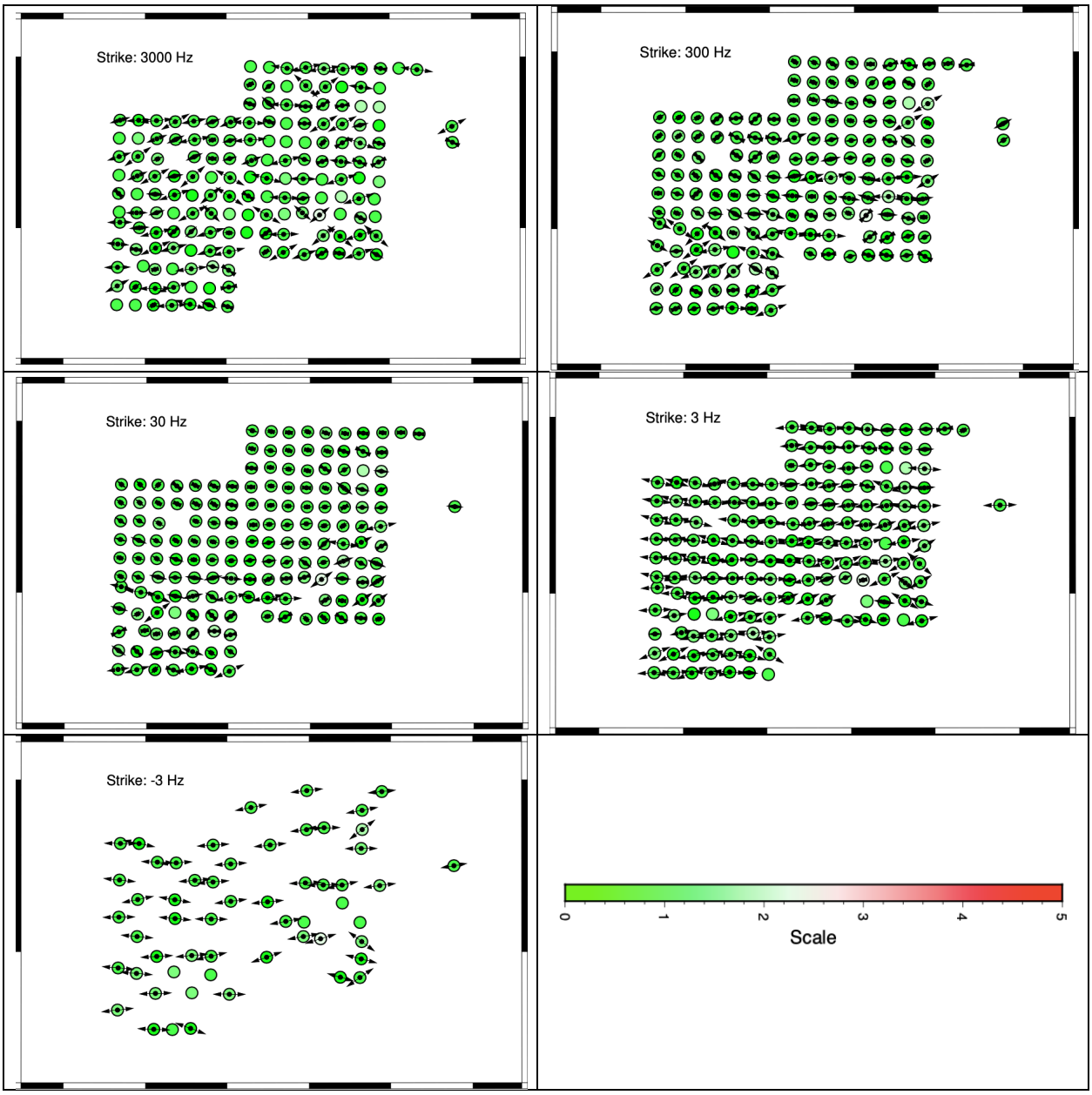

Figure 64: Single-site, multi-frequency strike directions for frequency bands of 10 kHz – 1 kHz (top left), 1 kHz – 100 Hz (top right), 100 Hz – 10 Hz (middle left), 10 Hz – 1 Hz (middle right), and 1 s – 10 s (bottom left). The length of the arrows indicates the phase difference, which is a measure of the strength of dimensionality, and the colour indicates the nRMS, with green acceptable and red and black unacceptable.

The plots show that the distortion model very well fits the data for all sites and for all frequency bands. The strike directions clearly exhibit generally an overall predominance for a direction of generally ENE-WSW to E-W, but there is scatter at high frequencies.

Histograms of the strike directions are plotted in Figure 65 on a 45° – 135° segment, as "strike" has a 90° ambiguity; the general strike direction was assumed to be E-W. In contrast to the impression from qualitative analyses above using Phase Tensors and RhoMIN directions, in these single-station strikes there is no dominant strike direction from 10 kHz to 100 Hz, but below 100 Hz there is a very strong preference for N80E to N85E. This direction is evident in all of the strike arrows in Figure 64. This is responding primarily to the basin and not to subsurface structures.

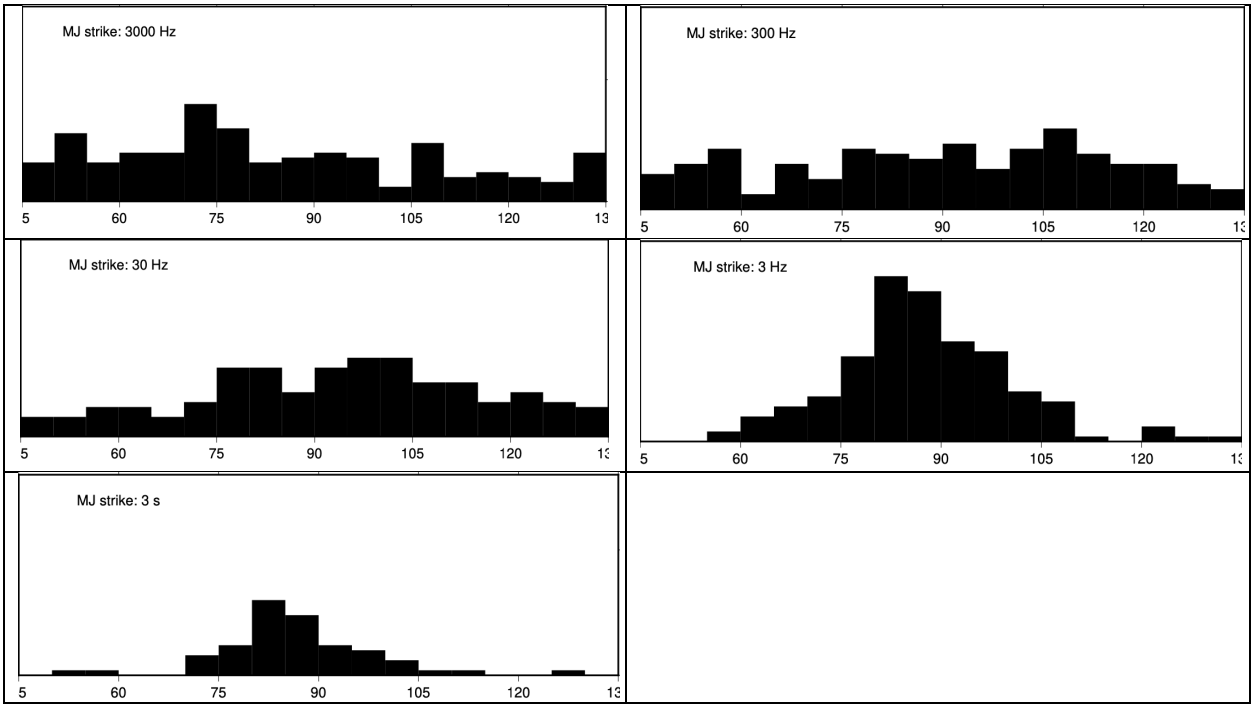

Figure 65: Histograms of the strike directions in the frequency bands 10 kHz - 1 kHz (top left), 1 kHz - 100 Hz (top right), 100 Hz - 10 Hz (middle left), 10 Hz – 1 Hz (middle right), and 1 s – 10 s (bottom left).

16.1.2. *Single-site, single frequency band: 10 kHz – 0.1 Hz (10 s)*

Next we examine the strike directions determined when we seek the strike that is acceptable at each site for all frequencies in the five-decade-wide band from 10 kHz – 10 s, which are the frequencies that are most sensitive to depths to 1400 m below surface. Note that for 2/3 of the sites the data only go to 1 Hz, so for those sites 4 decades are analysed.

The Quality Factors for this 5-decade frequency band are poor to very poor at 2/3 of the sites (Figure 66), due to the daytime data having poor AMT deadband data (5 kHz – 1 kHz) and poor data below 10 Hz due to short duration acquisition.

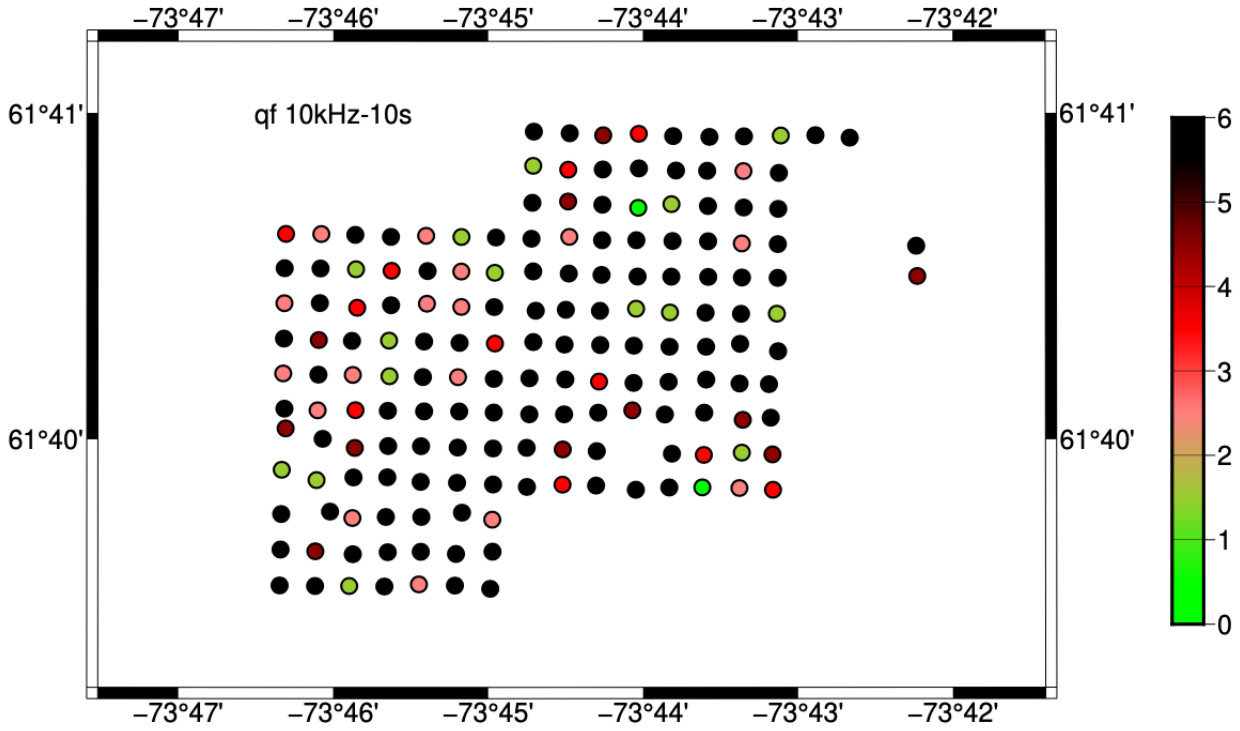

Figure 66: Quality Factors in the frequency band 10 kHz - 10 s.

The strike directions are shown in Figure 67. Almost all of the data accept a single strike direction for the whole band of frequency from 10 kHz – 10 s. This is quite remarkable. The strike directions do vary with location, but are predominantly approx. E-W.

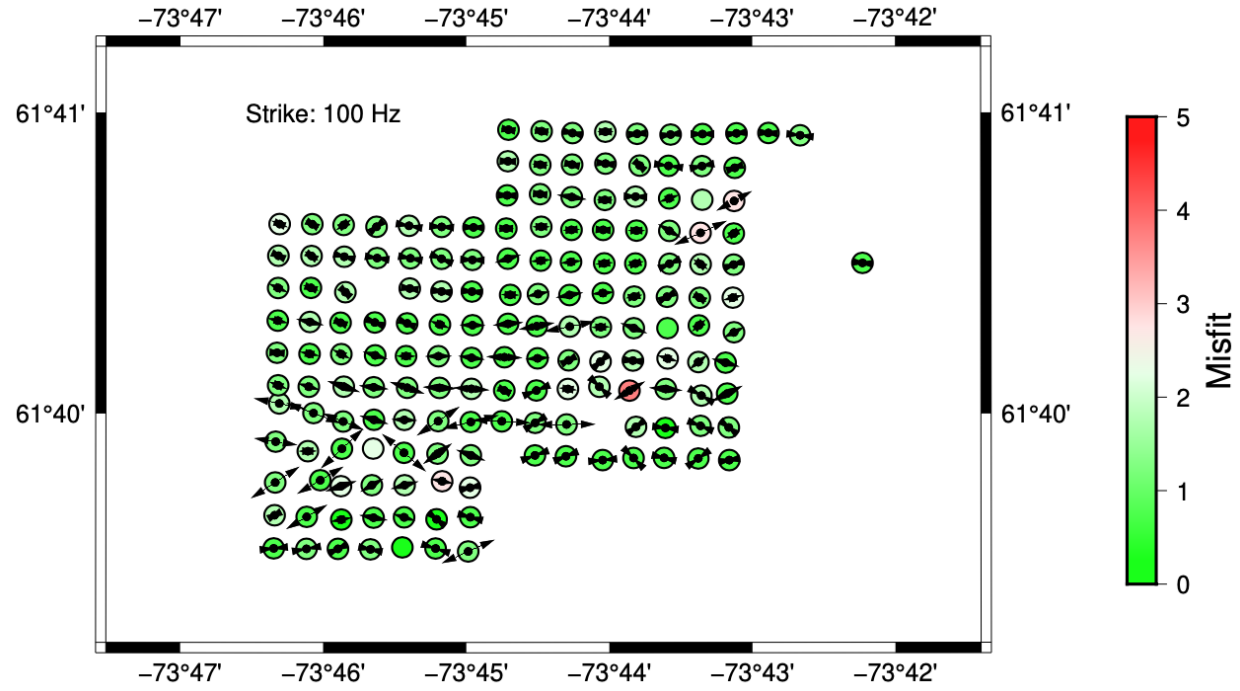

Figure 67: Strike direction for each site in the frequency band 10 kHz – 10 s. The scale is the average error of misfit of the distortion model to the data. Green = acceptable; Red = unacceptable. Assumed error floor of 3.5% in max |Z|.

The histogram of the strike directions is shown in Figure 68, and a peak in strike direction is evident at E-W. (Below though I derive a weighted histogram, where the weights are the sensitivity to strike direction at each site, that does exhibit a strong peak.)

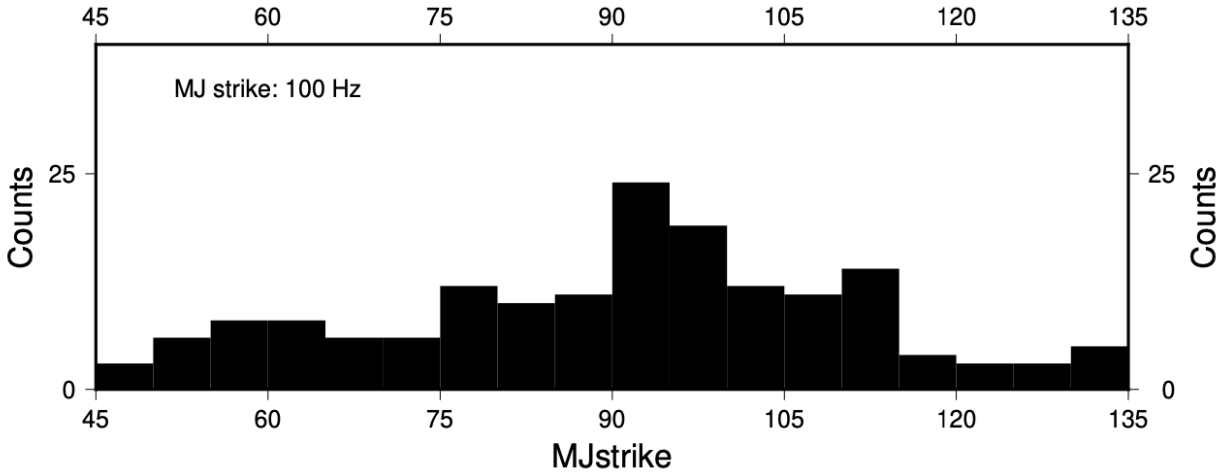

Figure 68: Histogram of strike directions in the five-decade band 10 kHz – 10 s.

Plotting the strike directions against longitude there is some clustering of strike directions, with a trend of N105E to the west moving to N80E in the East (Figure 69).

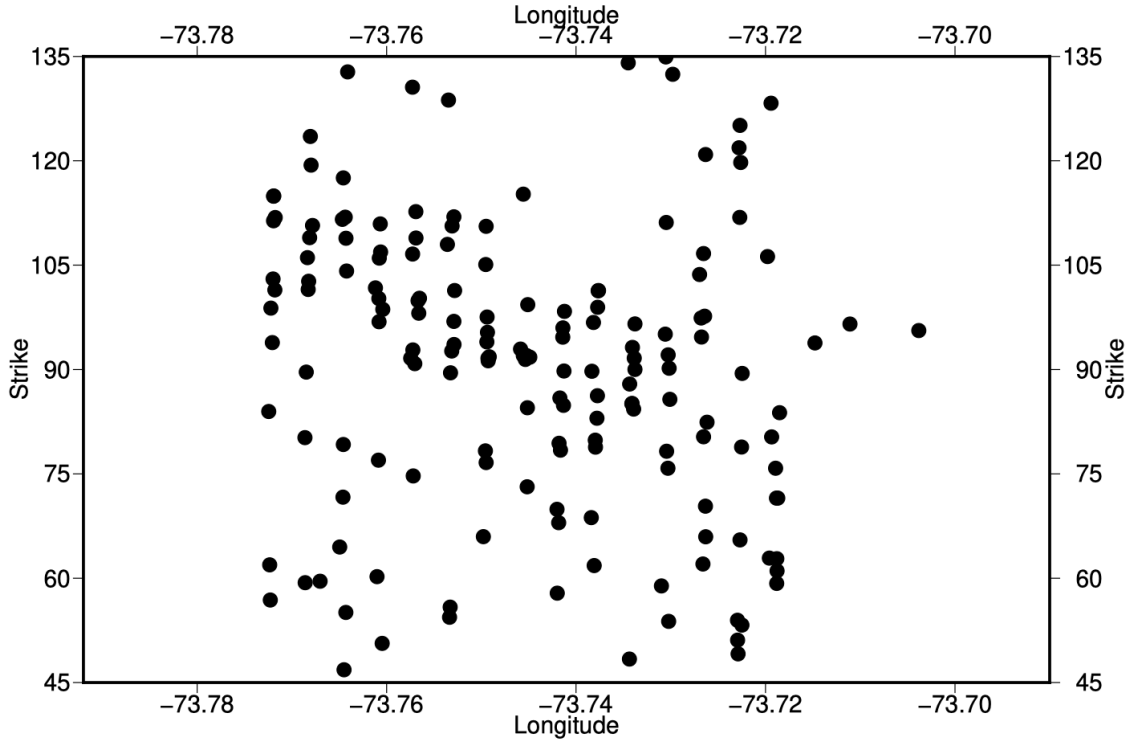

Figure 69: Strike direction against longitude for single-site analysis in the frequency range 10 kHz – 10 s.

16.1.3. *Single-site, single frequency band: 1 kHz – 1 Hz*

Given that 2/3 of the sites are daytime only, so have very poor AMT deadband responses, and are short duration, so do not go to lower frequencies than 1 Hz, I analyse the data in the 3-decade frequency band 1 kHz – 1 Hz. The Quality Factors are far higher in this band at most sites (Figure 70).

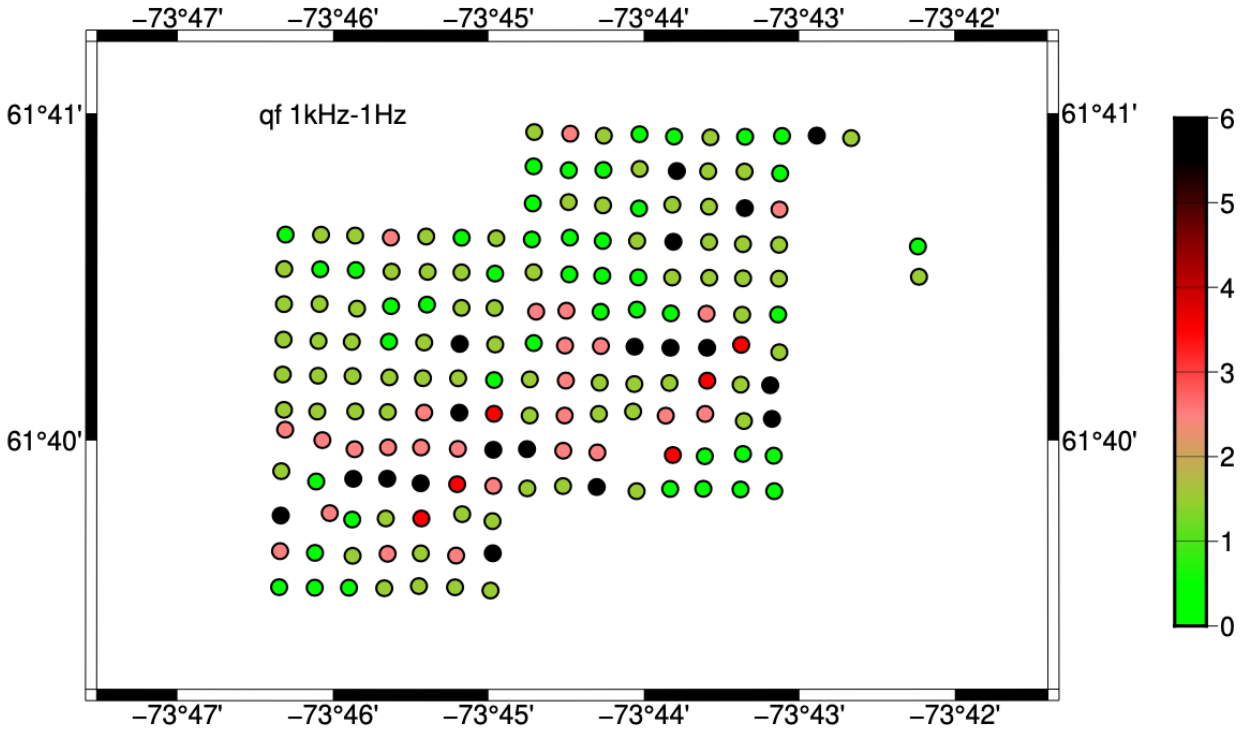

Figure 70: Quality Factors in the frequency band 1 kHz – 1 Hz.

The strike directions and dimensionality and quality of fit to the distortion model are shown in Figure 71, and the histogram of the strike directions is shown in Figure 72, and a peak at E-W in strike direction is again evident.

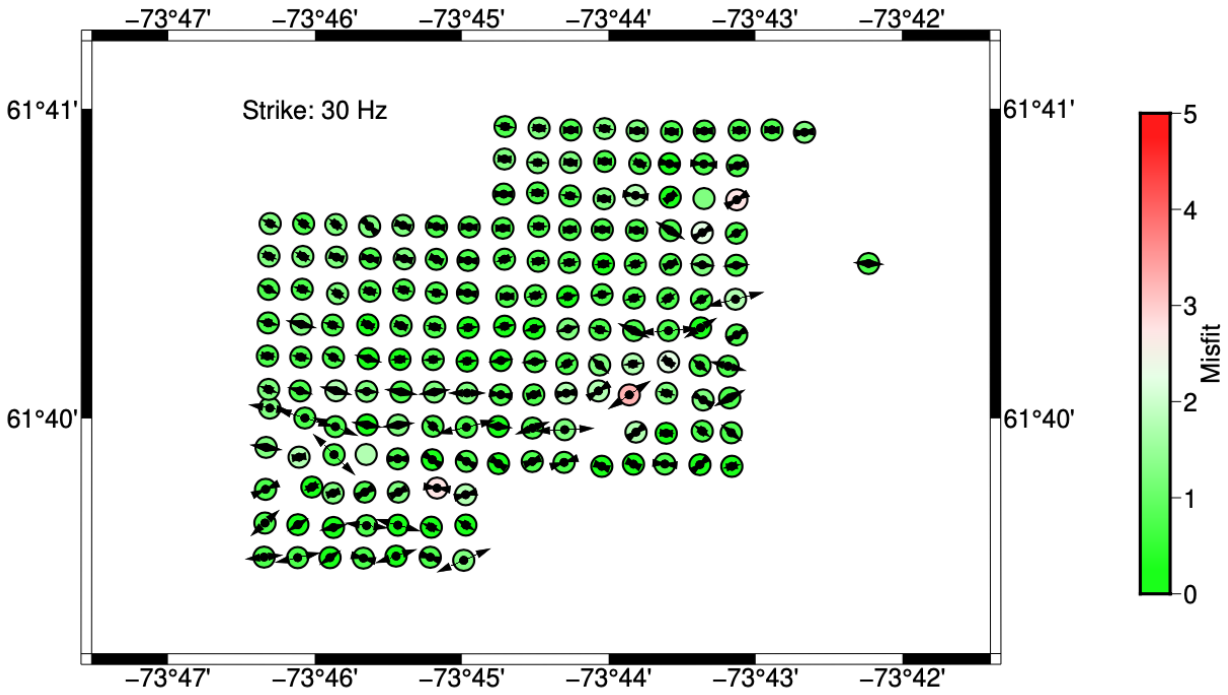

Figure 71: Strike direction for each site in the frequency band 1 kHz – 1 Hz. The scale is the average error of misfit of the distortion model to the data. Green = acceptable; Red = unacceptable. Assumed error floor of 3.5% in max |Z|.

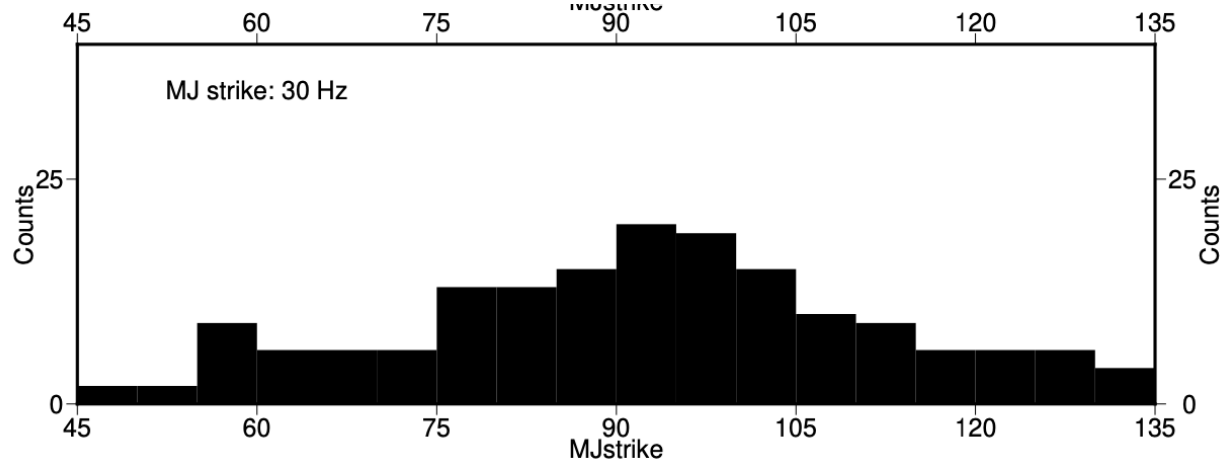

Figure 72: Histogram of strike directions in the three-decade band 1 kHz – 1 Hz.

Plotting the strike directions against longitude there is again clustering of strike directions, with a trend of N105E to the west moving to N80E in the East (Figure 73).

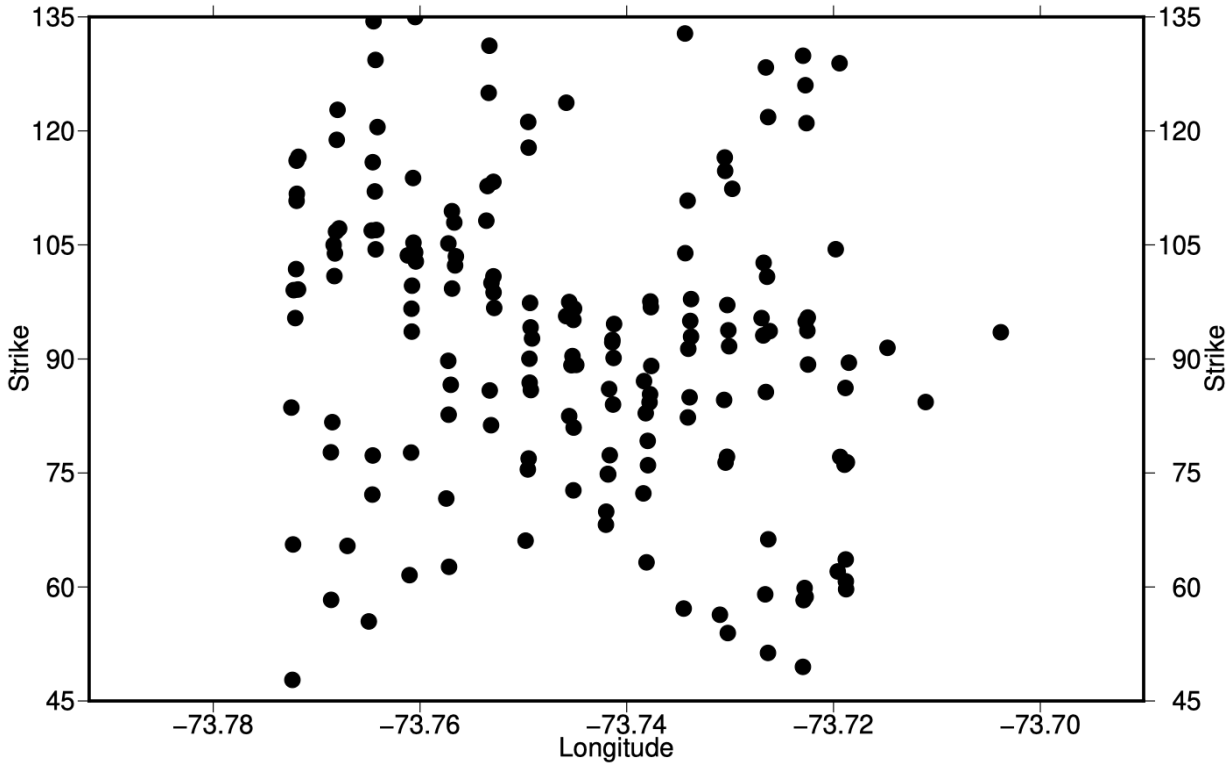

Figure 73: Strike direction against longitude for single-site analysis in the frequency range 1 kHz – 1 Hz.

16.1.4. *Single-site, single depth band: 400 m – 1400 m*

Penetration by MT data can vary from site to site due to laterally varying conductivity beneath the property. To account for this we can perform strike analyses based on approximate depths instead of frequency. We use the Niblett-Bostick algorithm [*Jones*, 1983] to transform the MT response estimates from frequency to depth.

The primary focus of depth of investigation for the MT data is 400 m to 1400 m. So finally we perform strike analyses in that depth band. The single site strikes for that depth band are shown in Figure 74. Again, there is very good site-to-site consistency, and the distortion model fits the data at all sites except for one.

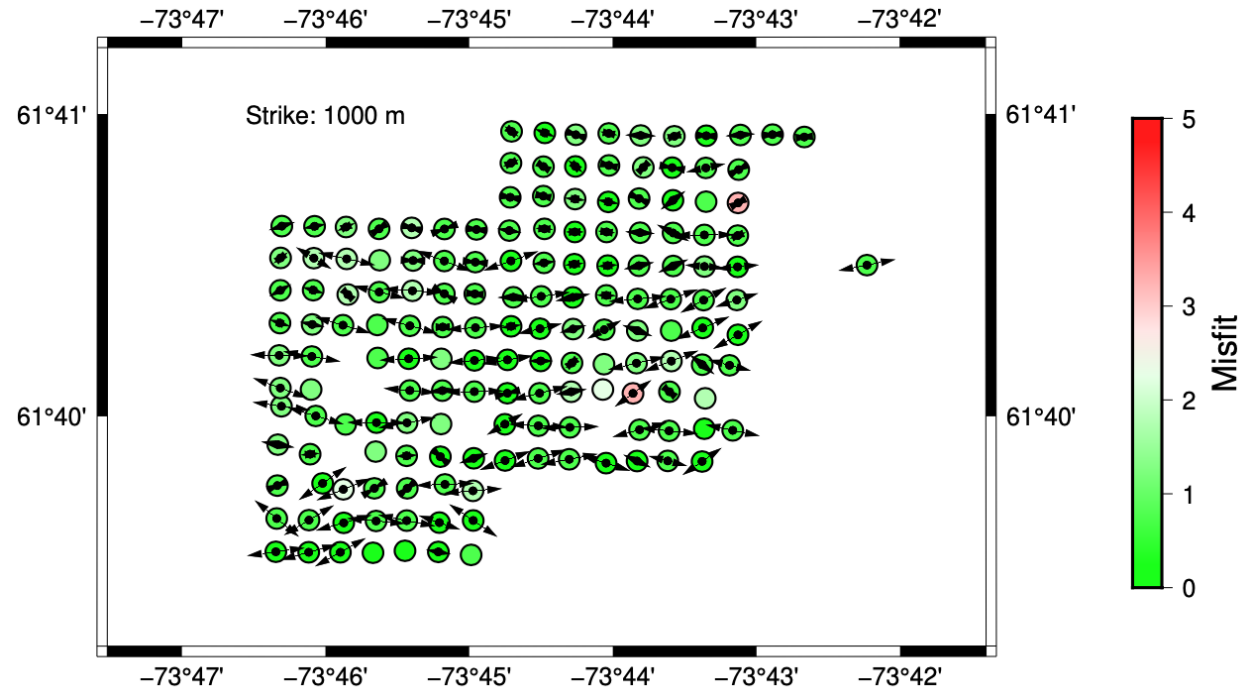

Figure 74: Strike azimuths for each site for the depth band 400 – 1400 m. The length of the arrow denotes the phase difference at the centre of the range, so is a measure of the strength of the structural anisotropy, and the colour denotes the goodness-of-fit to the distortion model, with green being acceptable and red being not acceptable. Error floor of 3.5% of max |Z|.

A histogram of all strikes is shown in Figure 75, where there is again a broad peak around E-W.

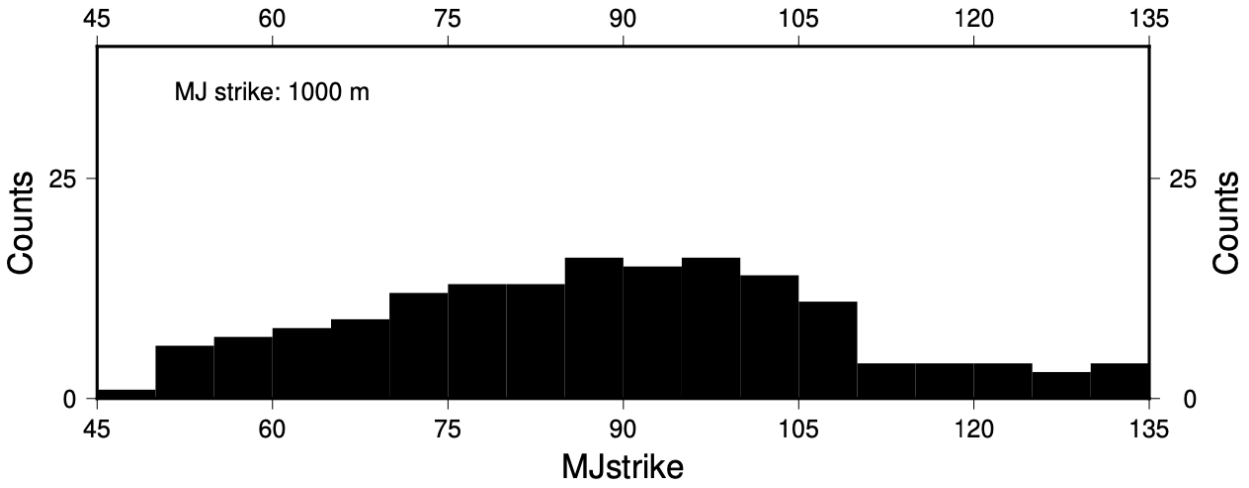

Figure 75: Histogram of individual site strikes for the depth band 400 – 1400 m.

16.1.5. *Single-site: Misfit sensitivity with strike direction - unweighted*

One way of determining sensitivity to strike direction is to rotate the data at each site through 90°, and determine the minimum and maximum misfit, then derive the ratio of the maximum RMS/minimum RMS (see below plots for profile analyses to see these rotations). This ratio indicates which sites are sensitive to strike direction (i.e., 3-D or very 2-D), and which are less

sensitive (i.e., close to 1-D). The ratios are plotted in Figure 76 for the whole 5-decade band 10 kHz – 10 s (left) and the 3-decade band 1 kHz – 1 Hz (right), and the sites with greatest sensitivity to strike are shown in dark red and black circles.

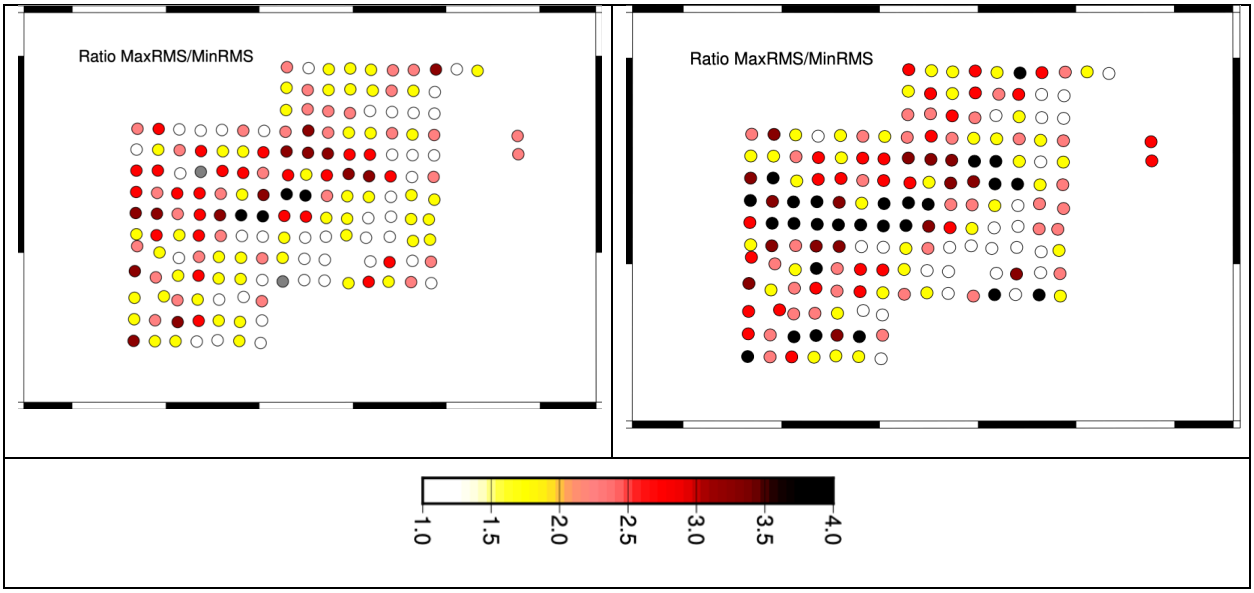

Figure 76: Ratio of the maximum RMS/minimum RMS for each site for the frequency band 10 kHz – 10 s (left) and 1 kHz – 1 Hz (right).

Single-station anomalies are an expression of noise and scatter at that station.

The histogram of the ratios (Figure 77) shows that for the 5-decade band (10 kHz – 10 s) half of the sites (55%) have weak sensitivity to strike direction, with the maxRMS/minRMS ratio <2.0 (white and yellow sites on Figure 76), and 90% <3.0. For the 3-decade band (1 kHz – 1 Hz), the histogram is flatter, with 38% <2.0 and 75% < 3.0.

Strong dimensionality is exhibited by 25% of the sites, shown in dark red and black on Figure 76 (right), mostly located in the centre and centre-west of the grid.

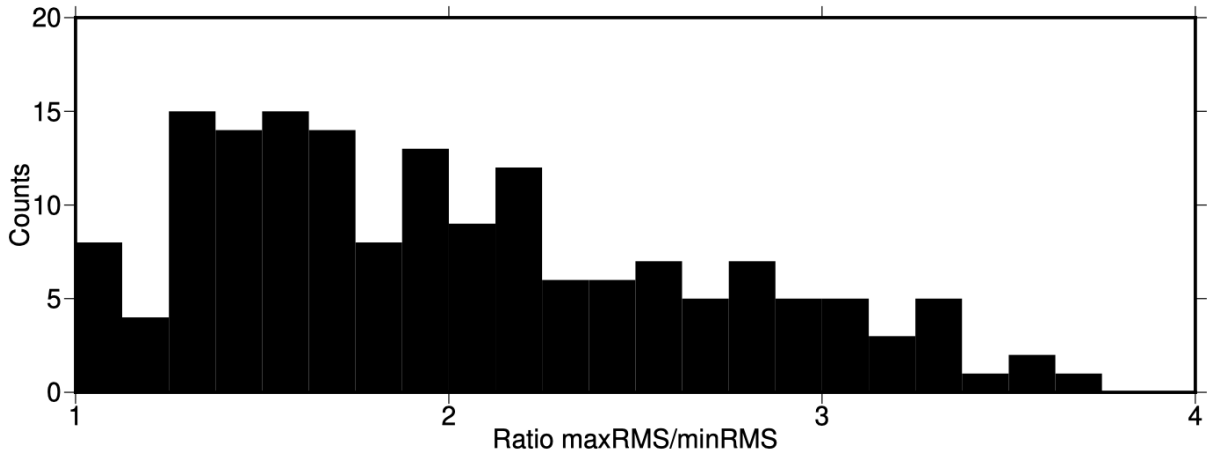

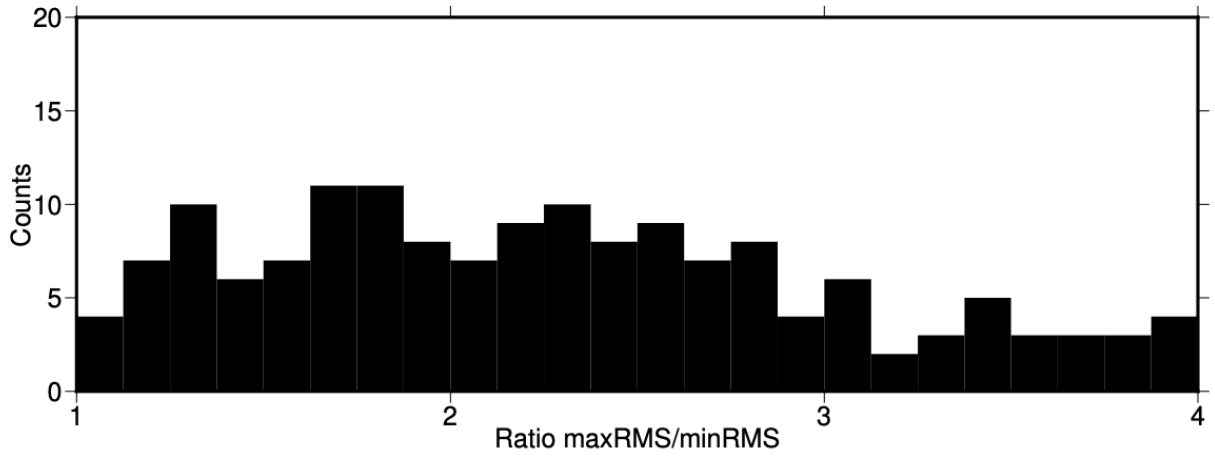

Figure 77: Histogram of the ratios of MaxRMS/MinRMS for single-site strike directions in the 5-decade frequency band 10 kHz – 10 s (top) and in the 3-decade frequency band 1 kHz – 1 s (bottom).

16.1.6. *Single-site: Misfit sensitivity with strike direction - weighted*

Given that 2/3 of the data have poor AMT and MT deadband estimates as they were short-duration, daytime acquisition, the question is whether the data quality influences these strike analyses.

To guard against inaccurate conclusions being drawn based on poor data, the ratio map of Figure 76 (right) for the 1 kHz – 1 Hz band is re-plotted but scaling the ratios by the QFs from Figure 70 (QFs<1 set to 1). This map is shown in Figure 78. We now note that very few of the sites have dependably strong maxRMS/minRMS ratios.

We can derive the histogram of the strike directions shown in Figure 67 but weighted by the sensitivity to strike given by the ratio/QF (with QF set to 1 if <1) shown in Figure 78. This histogram is shown in Figure 79, and the peak at around 90° – 110° is far more prominent than in the unweighted histogram (Figure 68).

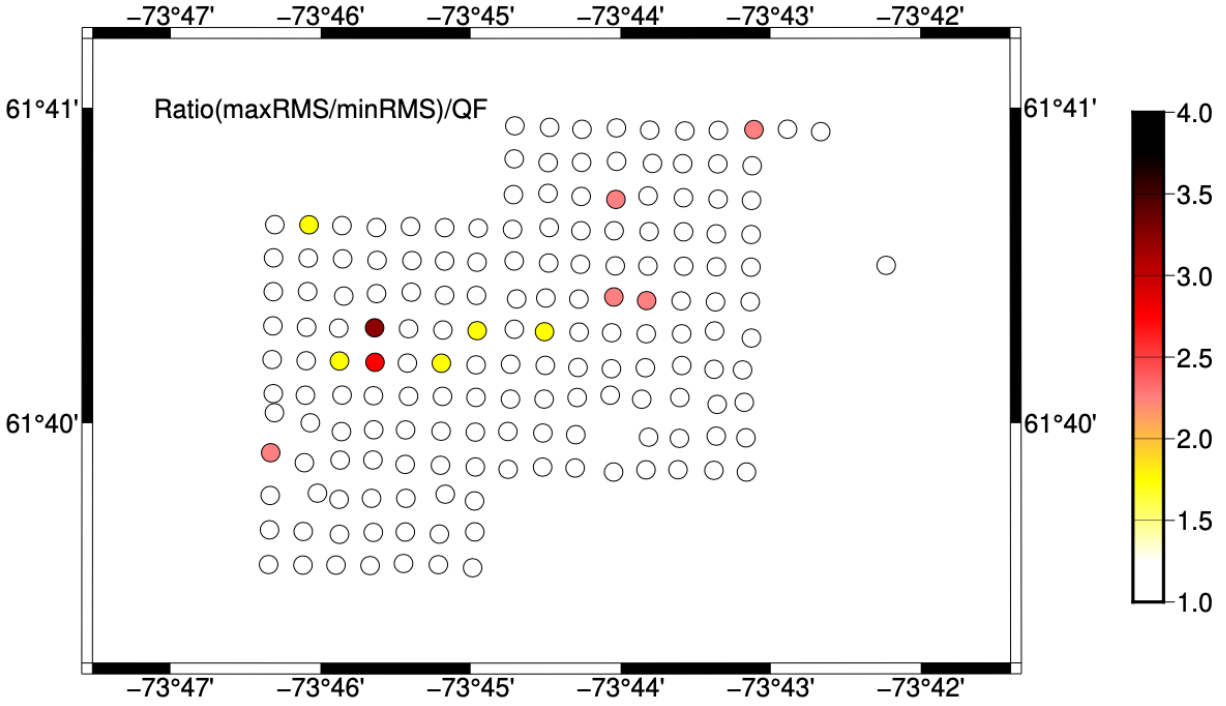

Figure 78: Ratio(maxRMS/minRMS)/QF for each site for the frequency band 1 kHz – 1 Hz. If QF<1 then set to 1.

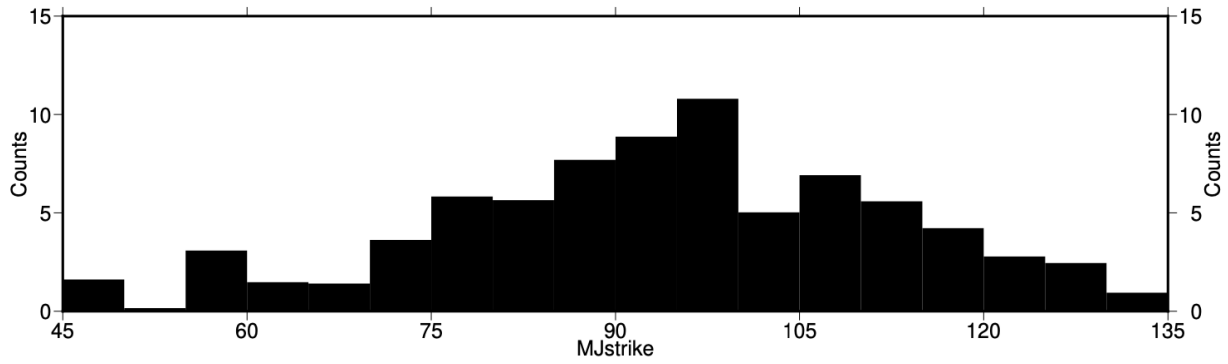

Figure 79: Weighted histogram of strike directions in the 3-decade band 1 kHz - 1 Hz, weights are ratio(maxRMS/minRMS)/QF, where if QF<1 it is set to 1.

Plotting the scaled ratios (=ratio/QF) by longitude against strike direction (Figure 80), we find that most sites have no reliable maxRMS/minRMS ratio, but those that do exhibit a strike direction that varies from around 110° in the west rotating to around 90° in the east.

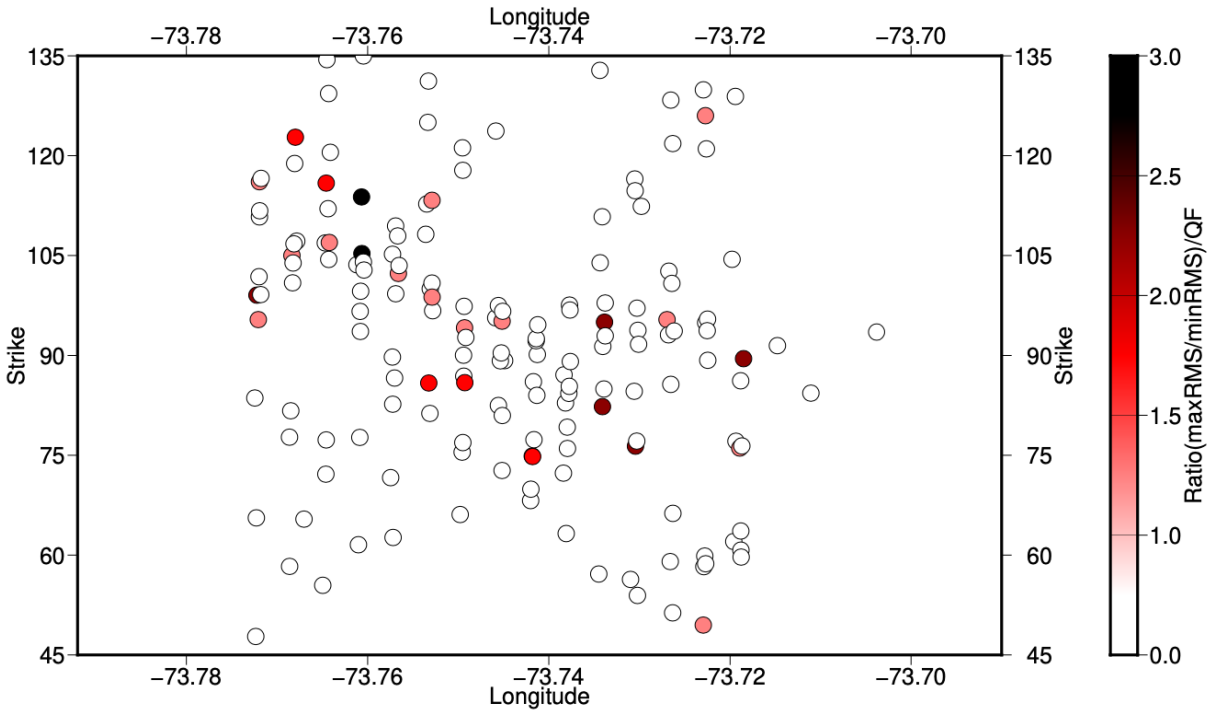

Figure 80: Ratio(maxRMS/minRMS)/QF at each site with Longitude and Strike direction.

16.1.7. *Single-site: Conclusions*

It is clear from our single site analyses that geoelectrical strike direction is weakly defined by these data, attesting to near 1-Dness for most of the sites. No one strike direction will fit all of the sites for all frequencies or depths of interest. Detailed analyses scaling the sensitivity to strike (i.e., the maxRMS/minRMS ratio) by quality (i.e., QF) for the frequency band 1 kHz – 1 Hz does show a robust feature that is present in the analyses, and that is a strike direction that is generally around 110° in the west rotating to around 90° in the east

16.2. Profile analyses

Given the single-site analyses, the next step is to determine if strike analyses along profiles leads to consistency. The sites are grouped into 15 N-S profiles, labelled P01 – P15 from west to east, with each profile comprising 11 sites in each profile save for profile P11, which has 10 sites. The profiles and sites are listed in Table 3.

Also, given the above analyses and discussion about data in the AMT deadband, and given that 2/3 of the sites do not have any data at frequencies <1 Hz, the strike analysis is performed for the 3 decades from 1 kHz – 1 Hz.

Table 3: Site allocation to N-S profiles

Profile	No. sites	Sites	Profile	No. sites	Sites
P01	11	MT1130-MT1139 & MT1338	P09	11	MT1217-MT1227
P02	11	MT1140-MT1150	P10	11	MT1228-MT1238
P03	11	MT1151-MT1161	P11	10	MT1239-MT1249
P04	11	MT1162-MT1172	P12	11	MT1250-MT1260
P05	11	MT1173-MT1183	P13	11	MT1261-MT1271
P06	11	MT1184-MT1194	P14	11	MT1272-MT1282
P07	11	MT1195-MT1205	P15	11	MT1283-MT1293
P08	11	MT1206-MT1216			

16.2.1. *Single profiles*

The strike directions for each profile individually are shown in Figure 81 (note that the vectors are plotted at double the scale length of prior plots for clarity) and in Figure 82, and the distortion model clearly fits the data. For each profile of 11 sites, the number of data are 11 sites x 33 frequencies x 8 data at each frequency = 2904 knowns. The number of unknowns for each minimization is 1 strike + 11 shears + 11 twists + 11 x 33 x 4 impedance estimates (in a 2D tensor there are two complex terms, so 4 unknowns) = 1475.

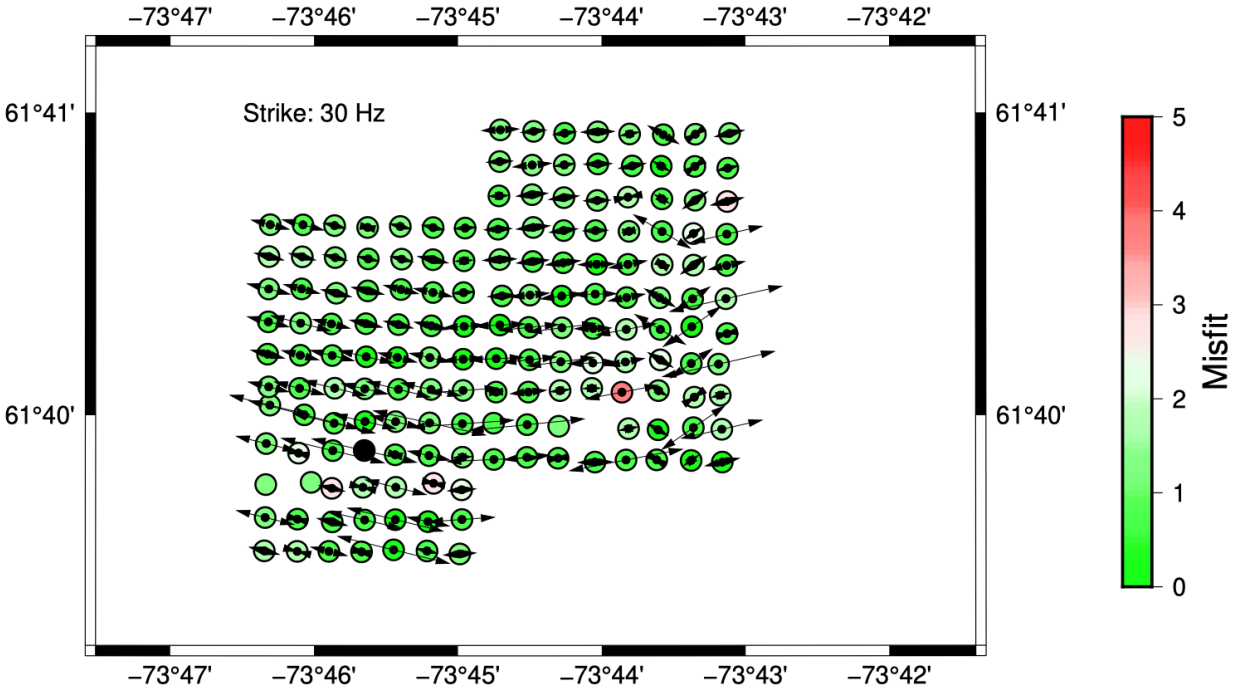

Figure 81: Strike directions for each profile for data in the 3-decades 1 kHz - 1 Hz.

Strike is around N105E for the western 6 profiles, then appears to rotate to N85E for the next 6 profiles, but this abrupt change occurs just as there are more northern sites and less southern sites. The easternmost 3 profiles appear to be more scattered.

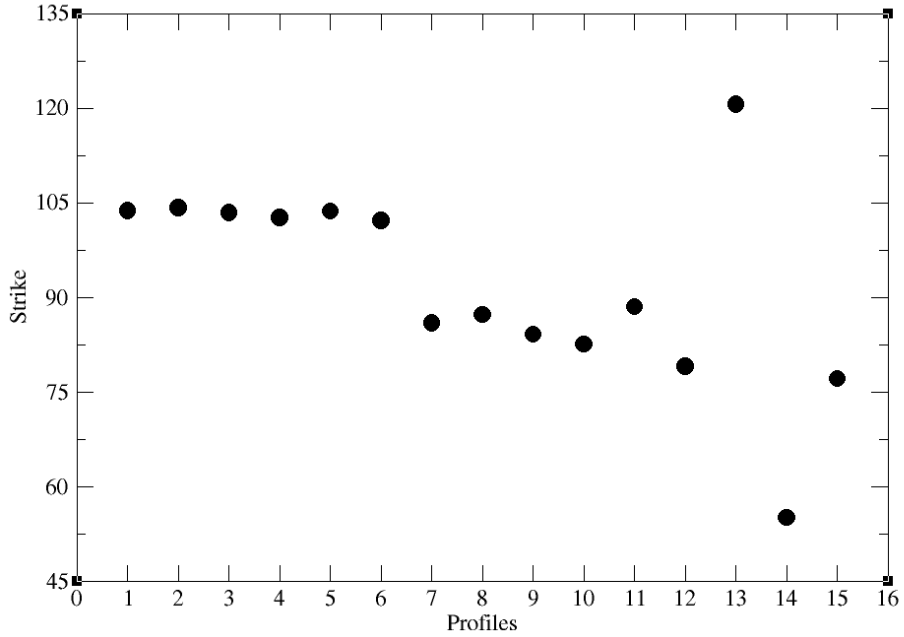

Figure 82: Strike direction for all sites along each profile P01 - P15 in the 3-decade frequency band of 1 kHz - 1 Hz.

16.2.2. *Multiple-profiles – groups of 3*

We can test of profile-to-profile consistency by analysing multiple profiles at a time with a moving spatial window, the strike for P01 comprise analysing sites from P01+P02 all together, then the strikes for profiles P02 to P14 comprise the profile and its neighbours on either side. Finally the strike for profile P15 comes from sites along profiles P14+P15.

For three profiles that is a total of 33 sites, so the number of data are 33 sites x 33 frequencies x 8 data at each frequency = 8712 knowns. The number of unknowns for each minimization is 1 strike + 33 shears + 33 twists + 33 x 33 x 4 impedance estimates (in a 2D tensor there are two complex terms, so 4 unknowns) = 4423.

The model of distortion fits all of the sites, except one, MT1252 (red circle on 3rd site from bottom of Profile 12). Again, strike is around 105° for the western 6 profiles (Figure 83, Figure 84), then rotates to 85° for the next 6 profiles, and again this abrupt change occurs just as there are more northern sites and less southern sites. Then the easternmost 3 profiles appear to be more consistent with a 60°-65° strike direction.

There are two regions that exhibit strong dimensionality, labelled Anomaly A and Anomaly B in Figure 83. One lies at the western side with a strike of 105° (Anomaly A), and the other lies at the eastern side with a strike of 60°-65°.

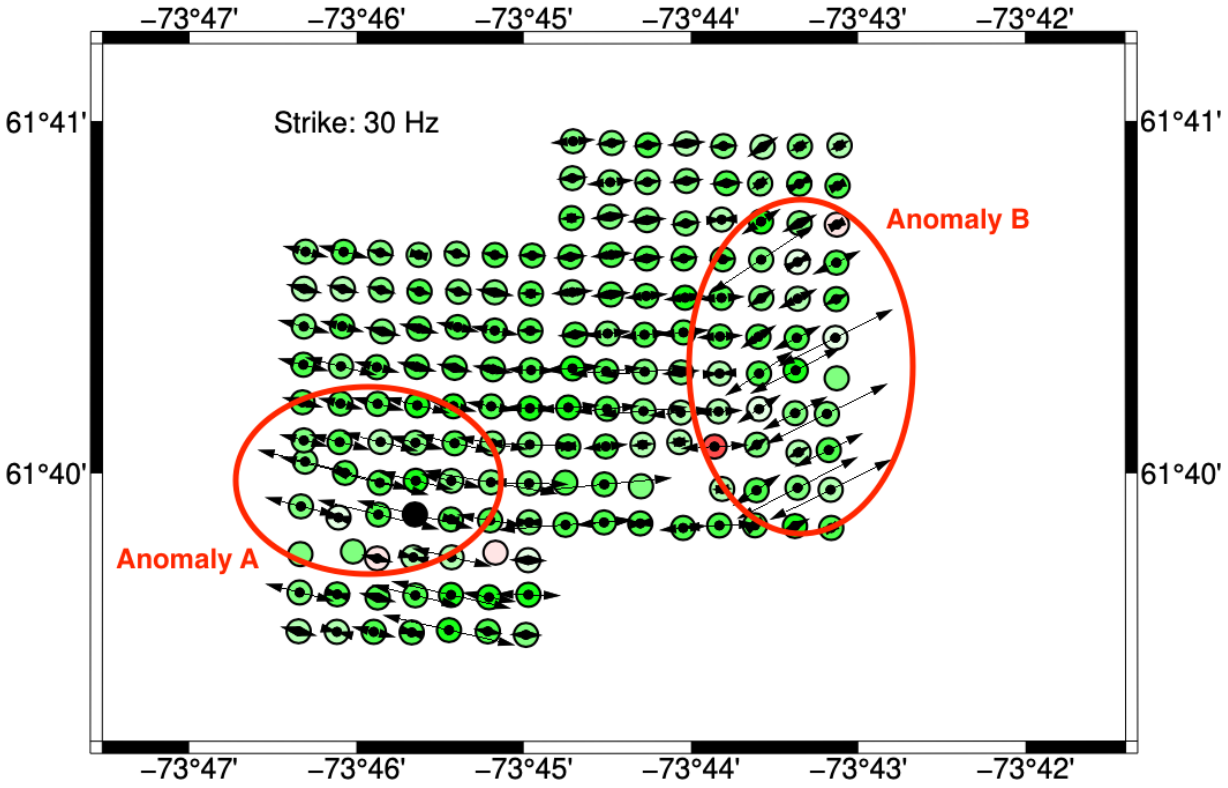

Figure 83: Strike directions for each profile for triples of profiles of data in the 3-decades 1 kHz - 1 Hz.

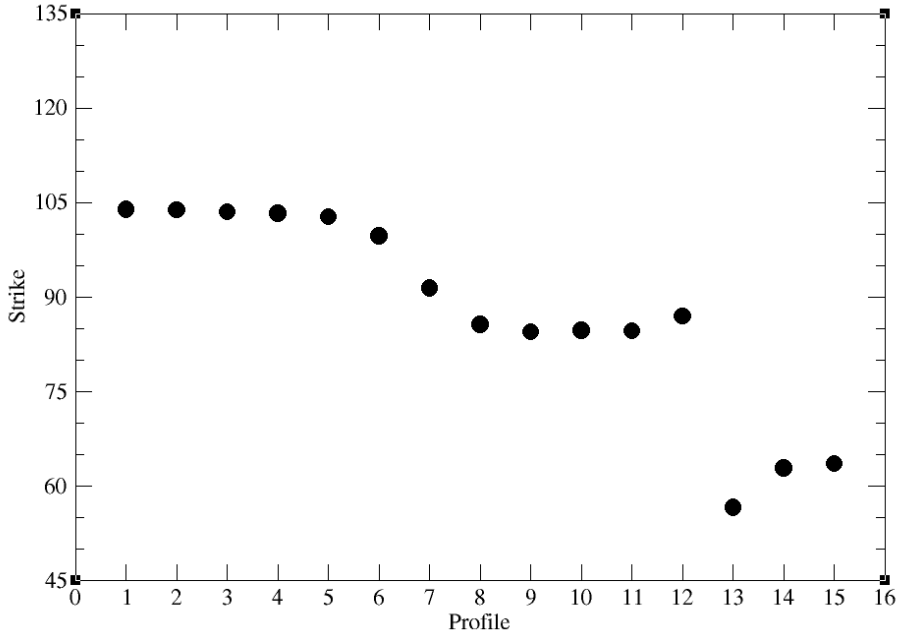

Figure 84: Strike direction for all sites along each profile P01 - P15 and its two neighbours in the 3-decade frequency band of 1 kHz - 1 Hz.

16.2.3. *Multiple-profiles – groups of 5*

We repeat the multi-profile exercise, but in profiles groups of 5 profiles, the central one being the main one and its two neighbours on either side. This is reduced to 3 profiles for the two end profiles (P01+P02+P03 for P01, etc.) and 4 profiles for the profiles next to them (P01+P02+P03_P04 for P02, etc.).

For five profiles of 55 sites total, the number of data are 55 x 33 x 8 = 14520 knowns. The number of unknowns is 1 + 55 + 55 + 55 x 33 x 4 = 7371. Each of the 15 minimisations takes between 1.5 h to 3 h on single core of an intel i9 chip running at 2.4 GHz. Total wall-clock time was 22 hours.

Again, strike is around 105° for the western 2 profiles, then with the intriguing direction of 120° for profiles 3 and 4. Strike then rotates to 80°-90° for the next 9 profiles. Then the easternmost 2 profiles appear to be more consistent with a 60°-65° strike direction. Again, there are two marked anomalies that show strong sensitivity to strike direction, Anomaly A in the SW with strike dominantly of around 120°, and Anomaly B in the E with strike around 60°-65°.

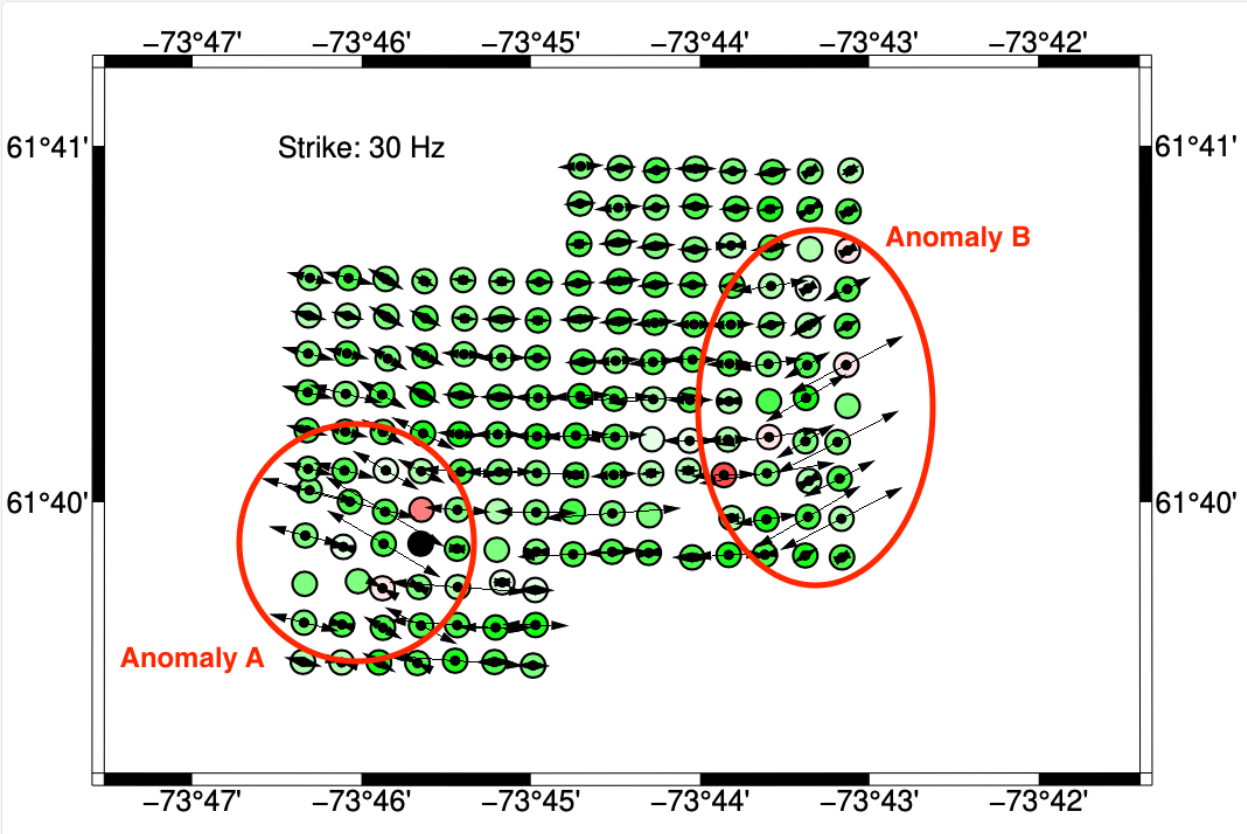

Figure 85: Strike directions for each profile for quintuples of profiles of data in the 3-decades 1 kHz - 1 Hz.

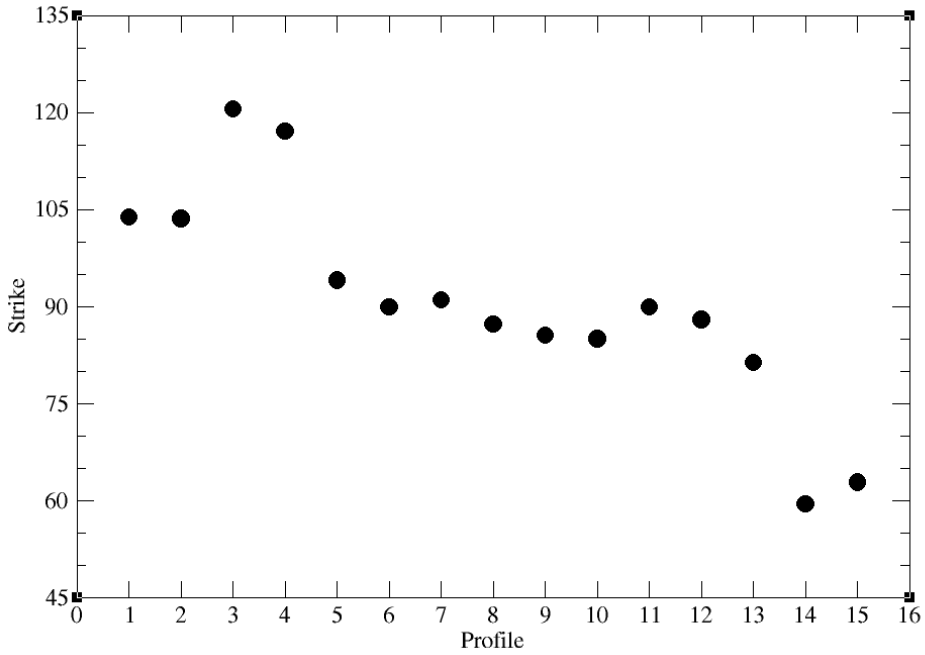

Figure 86: Strike direction for all sites along each profile P01 - P15 and its four neighbours in the 3-decade frequency band of 1 kHz - 1 Hz.

16.2.4. *Sensitivity to strike for profile groups*

Finally, for profile analysis we determine the sensitivity to strike for each profile group. This is accomplished by fitting a distortion model to all the sites along each profile for assumed strike directions from 0° to 90° in 1° increments.

The variation of nRMS for each profile is shown in Figure 87 – some profiles exhibit high sensitivity to strike direction, such as P01 and P05, and others far less so, especially the four eastern profiles. Some of this may come from along-profile strike variation, and this is examined in the next section.

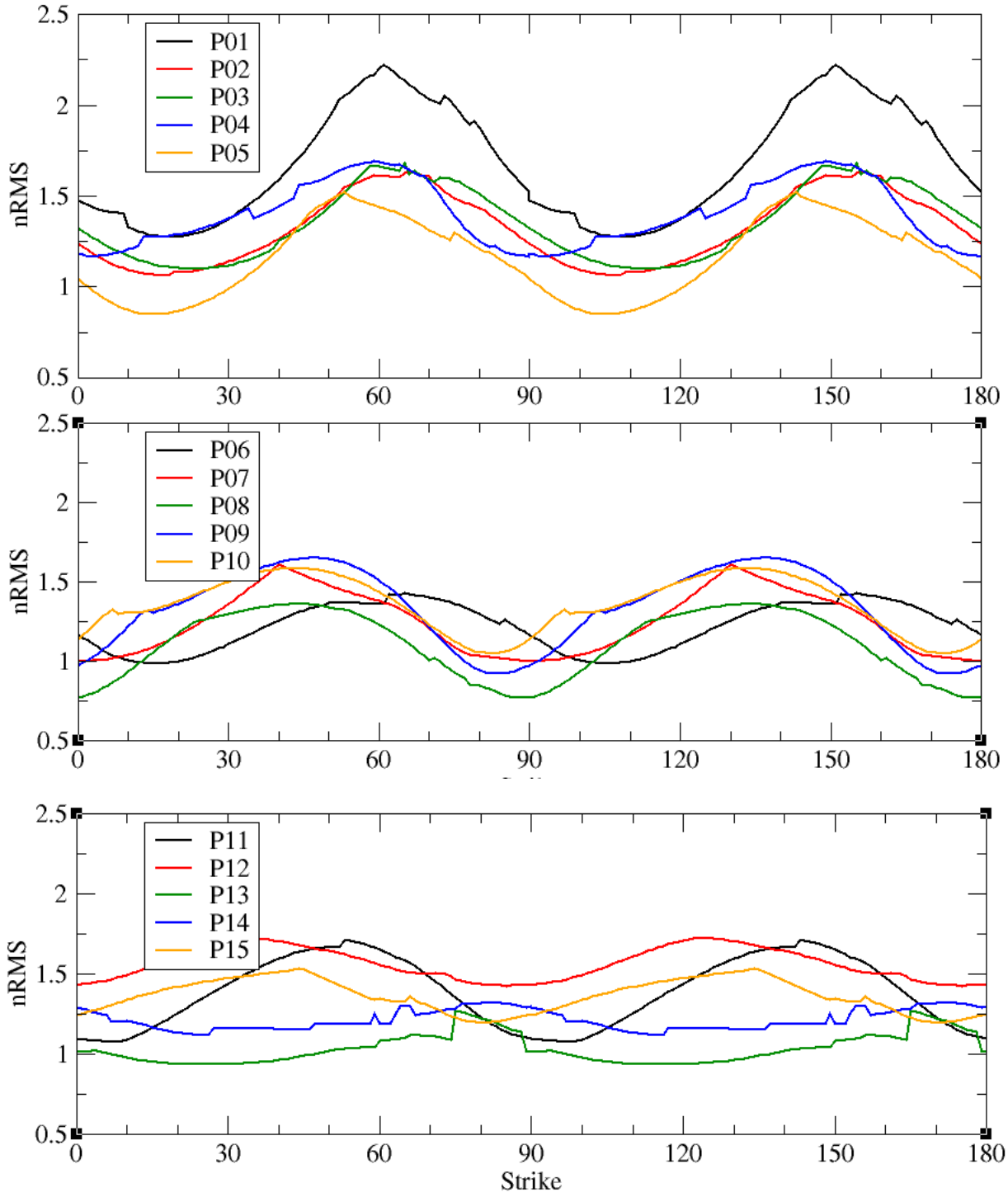

Figure 87: Variation of nRMS with strike direction for each profile.

16.3. Multi-site, local groups

There does appear to be variation along the designated acquisition N-S profiles, so we must adopt a novel approach and perform assessments of local groups of sites, first 9 sites then 25

sites then 49 sites. The aim here is to try to stabilize the strike directions to the local area rather than at one single site, which may be affected by noise or strong distortion or other effects.

The 9 sites group is notionally a stencil footprint of 3x3 set of sites for a uniform grid. Similarly for 25 sites it is notionally a stencil footprint of 5x5 sites. Finally 49 sites is a stencil footprint of 7x7 sites

16.3.1. *9 sites*

Local groups of nine sites, with the central site under consideration being one of the nine and the other eight are the closest eight to that site, i.e., notionally a moving 3x3 grid footprint with the main site in the centre, were constructed and multi-site, multi-frequency analyses performed from 1 kHz – 1 Hz. Thus, a total of 168 separate minimizations were performed, each of nine sites (no. sites *n*=9) of 33 frequencies (no. freqs. *m*=33). So the number of data to be fit per minimization was 9 x 33 x 8 = 2376 (8 data in the 2x2 complex impedance tensor), and the number of unknowns was 1207 (1 strike + *n* twists + *n* shears + 4*nm* regional impedances).

The strike directions are shown on Figure 88, and in histogram form in Figure 89. Again, there is a dominance of strikes from 90° – 105°.

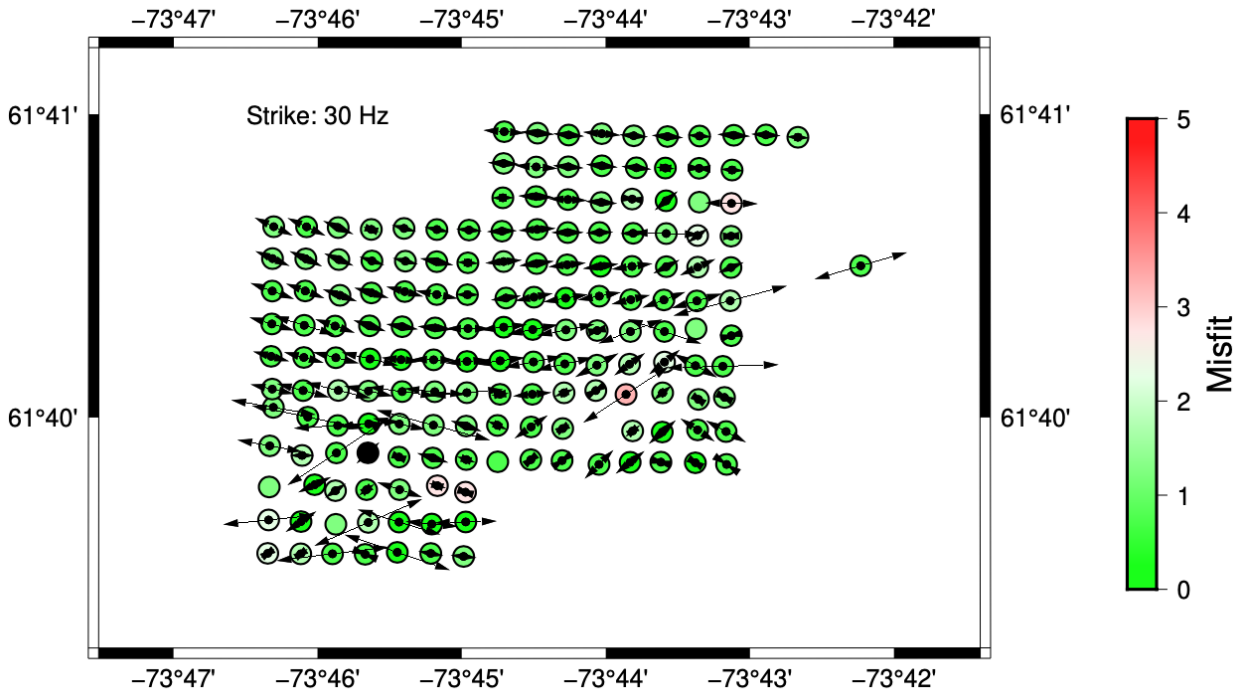

Figure 88: Strike directions in the frequency band 1 kHz - 1 Hz for local groups of 9 sites centred on the main site. The length of the arrow is the phase difference in the two orthogonal directions at 30 Hz.

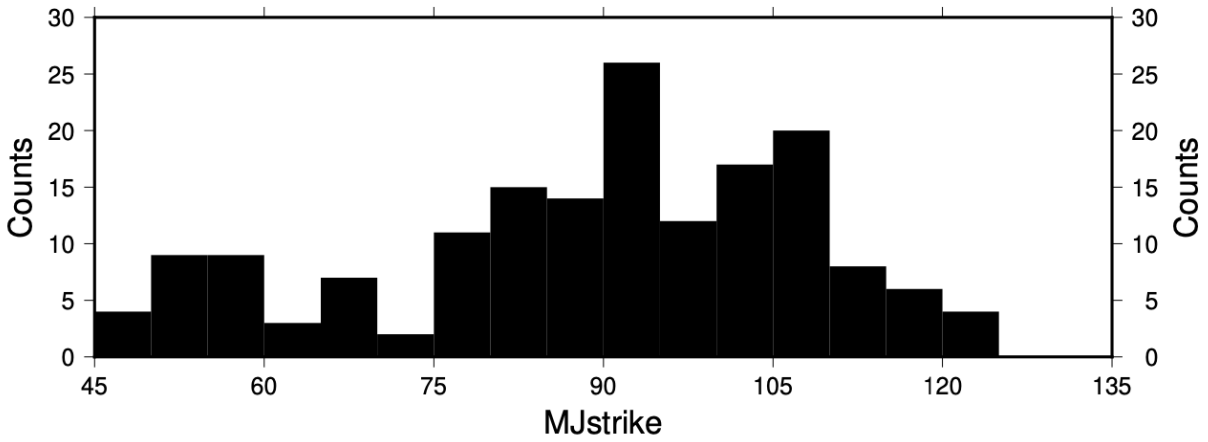

Figure 89: Histogram of strike directions for 9 sites in 3x3 stencils centred on the main site for frequencies from 1 kHz - 1 Hz.

16.3.2. *25 sites*

The local groups exercise was repeated, but with 25 sites, i.e., notionally a moving 5x5 grid footprint centred on the main site. This took 168 minimizations, each of 25 sites simultaneously of 33 frequencies. So the number of data to be fit per minimization was 25 x 33 x 8 = 6600, and the number of unknowns was 3351.

The distortion models fit the data, and we now see that there is indeed variation across the grid, with sites to the SW (Group A) preferring 60°, sites to the E (Group B) preferring 75°, and the rest preferring 90° (Figure 90).

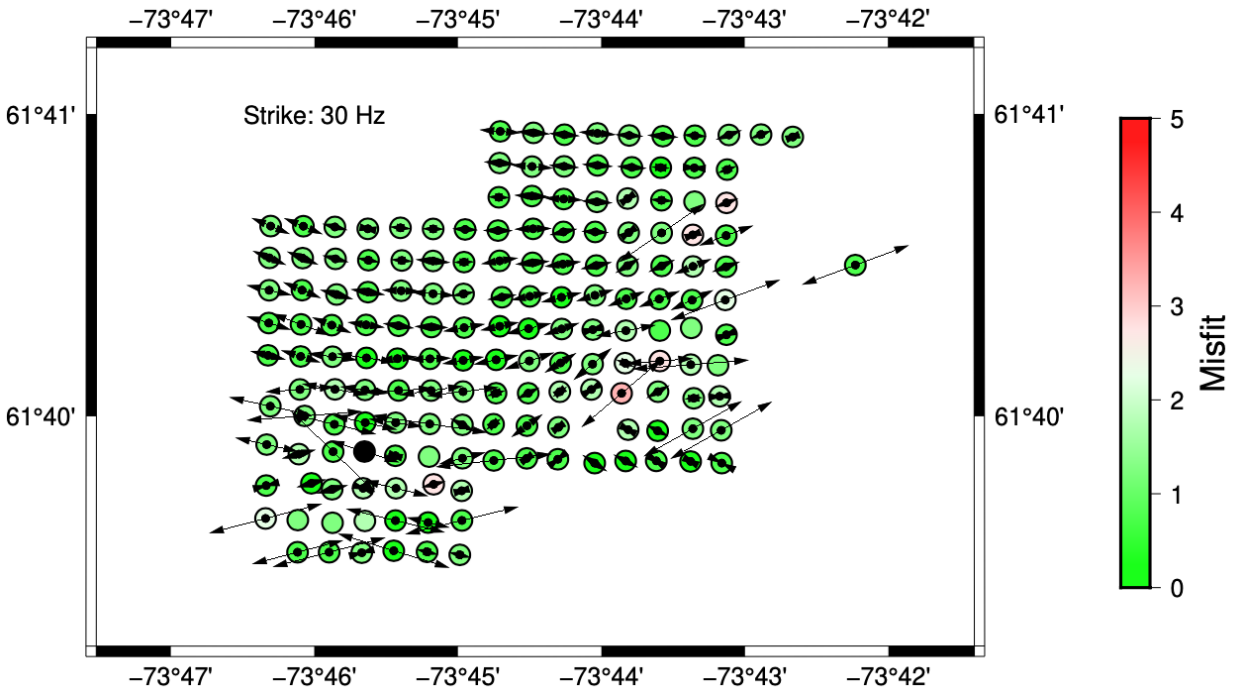

Figure 90: Strike directions in the frequency band 1 kHz - 1 Hz for local groups of 25 sites centred on the main site. The length of the arrow is the phase difference in the two orthogonal directions at 30 Hz.

These three directions are shown as distinct peaks in the strike direction histogram plot of Figure 91.

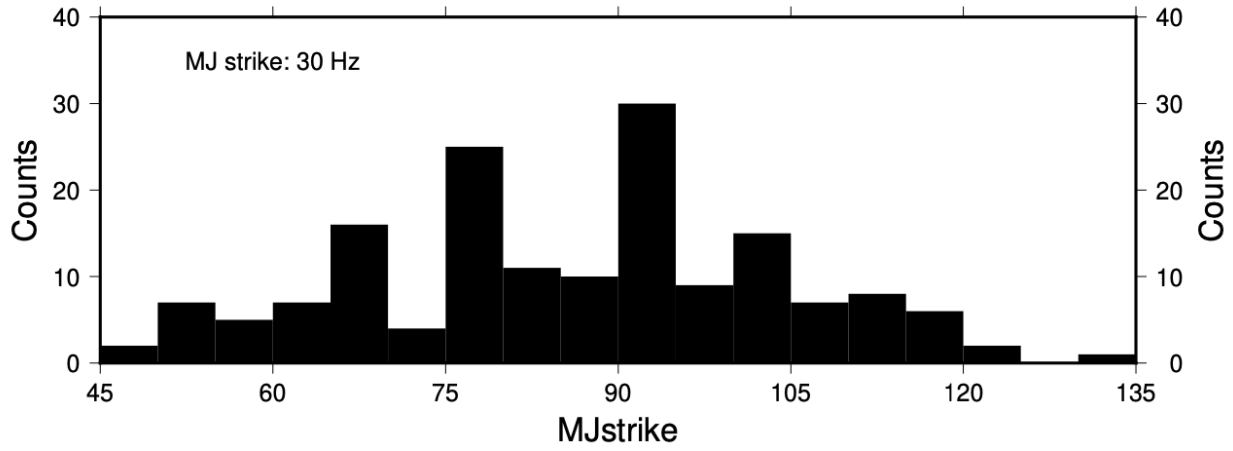

Figure 91: Histogram of strike directions for 25 sites in 5x5 stencils centred on the main site for frequencies from 1 kHz - 1 Hz.

16.3.3. *49 sites*

Finally, we perform the analyses with groups of 49 sites centred on the site of interest, i.e., for a uniform grid a 7x7 site stencil. The number of data to be fit per minimization was 12936 (49x33x8), and the number of unknowns was 6567 (1+49+49+49*33*4). Each minimization took of order 100 mins computational time, so the total computation time was 168 x 100 mins = 280 hours, which is approx. 12 days, so a wall-clock time of 3 days when run on 4 cores simultaneously.

The dominant strike direction is 85°-90°, but there is a second peak at 100°-105° and a broader peak at 60°-70° (Figure 93). There are two regions that are different from this overall strike direction (Figure 92), namely Anomaly A, with a direction consistent with the second peak of 100°-105°, and Anomaly B with a direction of 60°-70°.

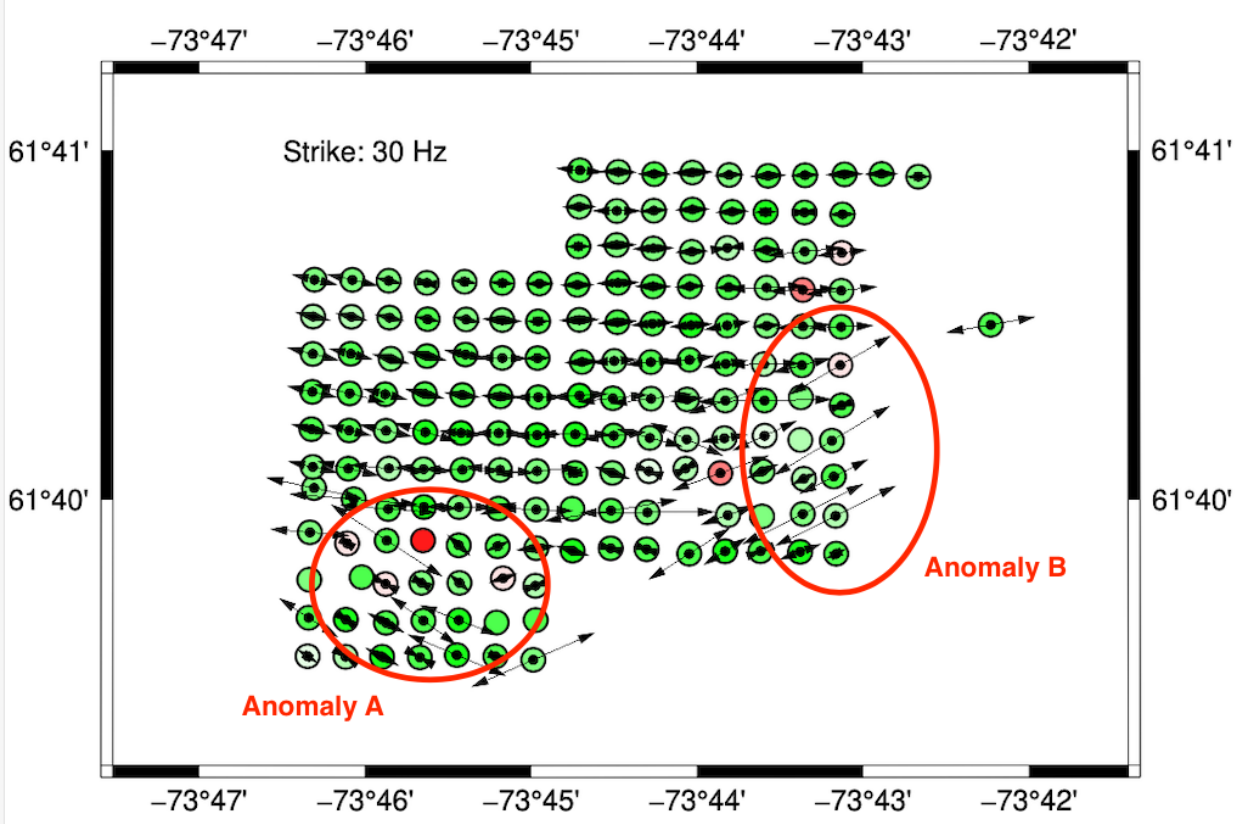

Figure 92: Strike directions in the frequency band 1 kHz - 1 Hz for local groups of 49 sites centred on the main site. The length of the arrow is the phase difference in the two orthogonal directions at 30 Hz.

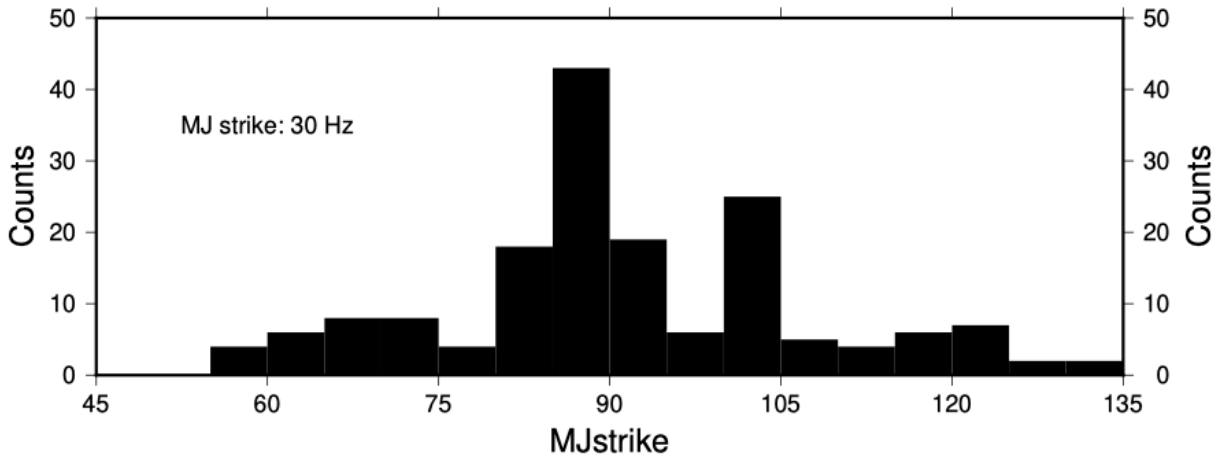

Figure 93: Histogram of strike directions for 49 sites in 7x7 stencils centred on the main site for frequencies from 1 kHz - 1 Hz.

17. Imposing a strike direction of E-W

Given that the majority of the sites favour a direction of E-W, we can ask the question "*how wrong will we be if we impose a direction of E-W?*". This is shown by the error plot of Figure 94. This plot shows that almost all sites will allow that 2D strike direction.

One site in the SW (MT1165) is inconsistent with the assumed direction, with an nRMS of 3.16. All other sites in Anomaly A are consistent with this direction.

In the east, site MT1252 (SE) is poorly fit by this direction (nRMS = 4.15); when allowed to find its own best strike direction, the analysis converges to E-W.

Three sites in Anomaly B on profiles P14 and P15 are not well fit by this direction: MT1279 on P14 (nRMS = 3.6), and MT1288 and MT1291 on P15 (nRMS = 2.6 and 2.9 respectively).

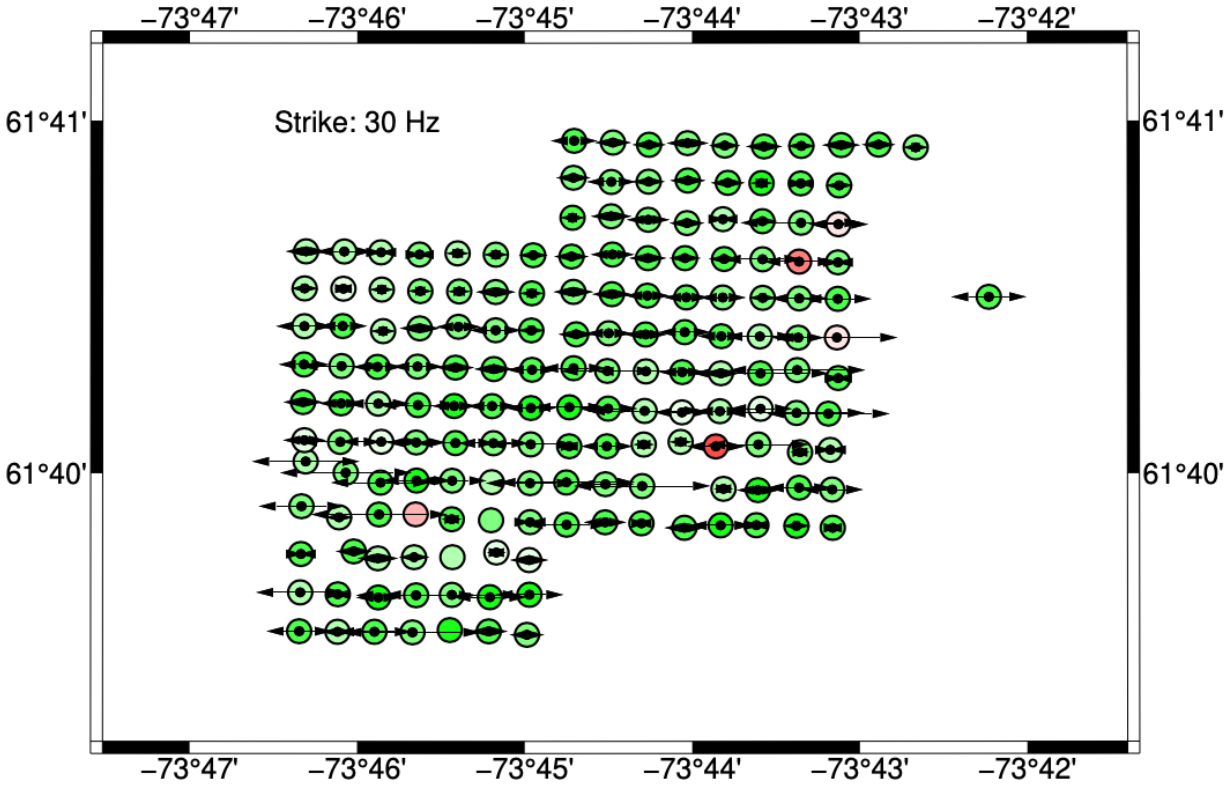

Figure 94: nRMS error at each site for a strike direction of E-W for data in the range 1 kHz -1 Hz with an adopted error floor of 3.5% in max |Z|.

Overall therefore, a generic strike of E-W is acceptable to all sites, except those discussed above, with an adopted error floor of 3.5% in max |Z|, i.e. 7.14% in RhoA and 2° in Pha. The *shear* and *twist* galvanic distortion estimates at each site are shown in Figure 95, and show high spatial correlation from site-to-site. This is possibly a sign that the angle chosen is not the most appropriate. Particularly the *twist* values, as *twist* is a rotation operator, show some grouping that can be related to the locations of Anomalies A and B.

However, when we plot the *shear* and *twist* values for decompositions where each site is allowed to choose its own best strike direction, i.e., the directions shown in Figure 71, we get the figures of Figure 96. Clearly the story here is that there is indeed strong galvanic distortions at most sites, and whatever is causing the distortion is of large extent leading to spatial correlations.

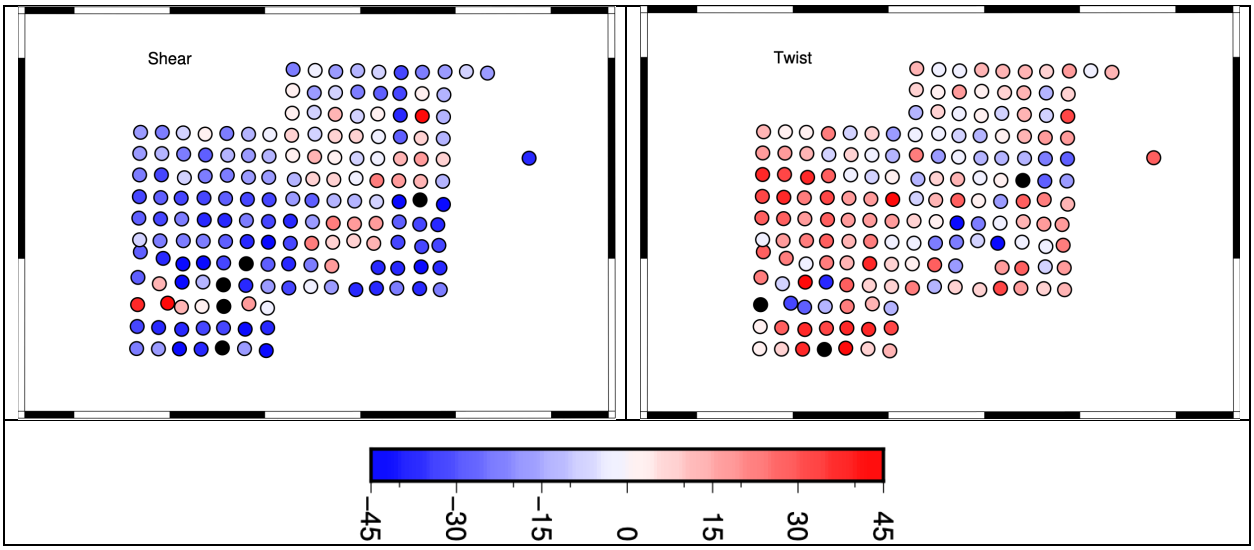

Figure 95: Shear (left) and Twist (right) values for an assumed strike of E-W for data in the frequency range of 1 kHz - 1 Hz with an adopted error floor of 3.5% in max |Z|.

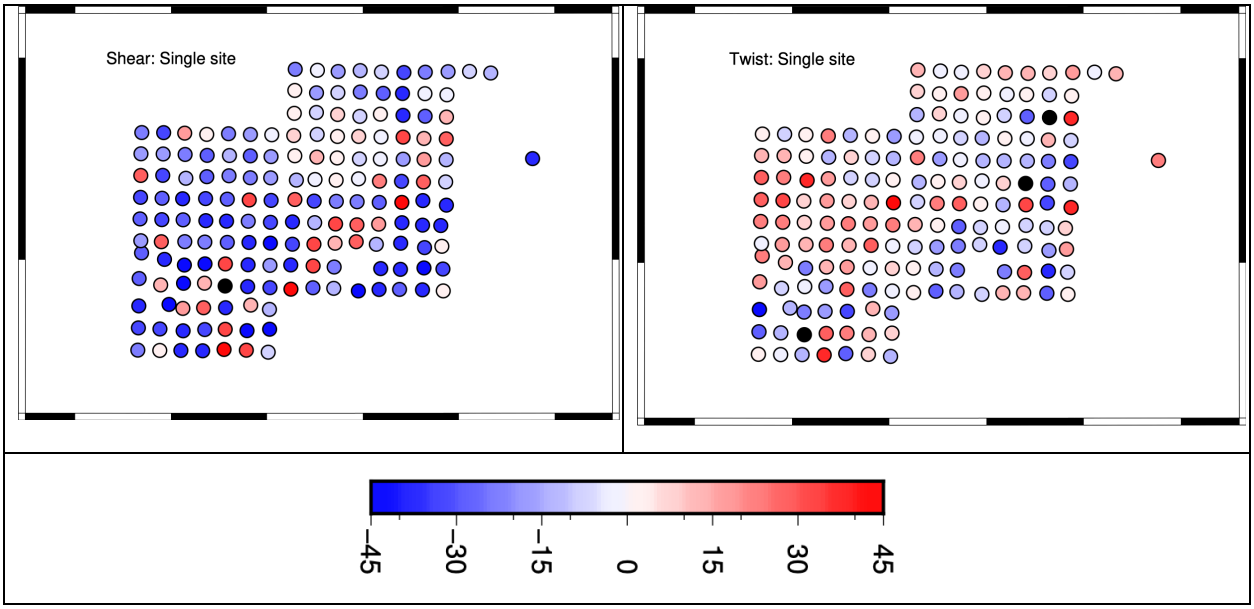

Figure 96: Shear (left) and Twist (right) values for the best strike at each site for data in the frequency range of 1 kHz - 1 Hz with an adopted error floor of 3.5% in max |Z|.

17.1. Lower error floor

A lower error floor will yield more sites than are not in agreement, and as a test these are shown in Figure 97 for floors of 1.75% in Z, which is 3.5% in RhoA and 1° in Pha. At this error level, many sites are inconsistent with the adopted E-W strike direction.

➔ These two figures, Figure 94 and Figure 97, show the essential nature of fitting models to data and the importance of precise and accurate errors.

○

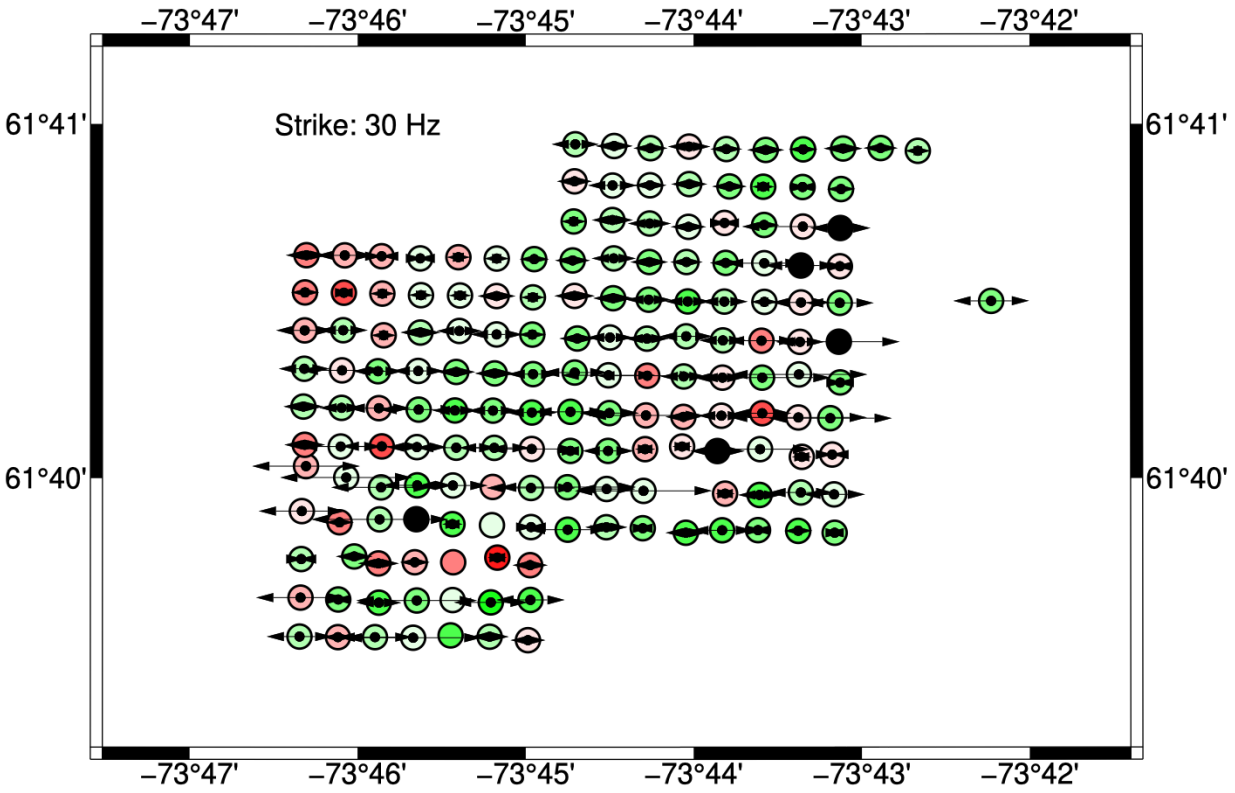

Figure 97: nRMS error at each site for a strike direction of E-W for data in the range 1 kHz -1 Hz with an adopted error floor of 1.75% in max |Z|.

When the data uncertainties are large, the data are well represented by a 1-D half-space. As uncertainties reduce, higher-dimensional structure can be resolved. The Earth is three-dimensional in general, and with sufficiently precise data a finely-gridded 3-D model is required to fit the responses.

In the case of these data, we have concerns about the veracity of the error estimates, and the Quality Factor analysis implied that a general assumption of an error floor of 3.5% in max |Z| was reasonable. When we make this assumption, we can validly model the data along all profiles in 2-D. If however the errors are better than 3.5%, then 2-D inversions along profiles may not yield accurate models.

Also, by adopting a strike direction of E-W then subtleties associated with Anomalies A and B will be lost. As illustrated in Figure 98, when the MT tensor is rotated the maximum direction, Zmax, is fairly insensitive to the precise direction and can tolerate quite a lot of difference in strike and still have close to the same value. In contrast, the Zmin value is sensitive to very sensitive to strike direction, and a wrong direction will rotate some of the Zmax information into the Zmin data.

Consequently, when modelling data in an incorrect strike direction, the Zmax data is modelled quite accurately while the correct Zmin data is inaccurately modelled. This results in the large

structures being well-imaged but the details of those structures resolved by Zmin being significantly less well-resolved.

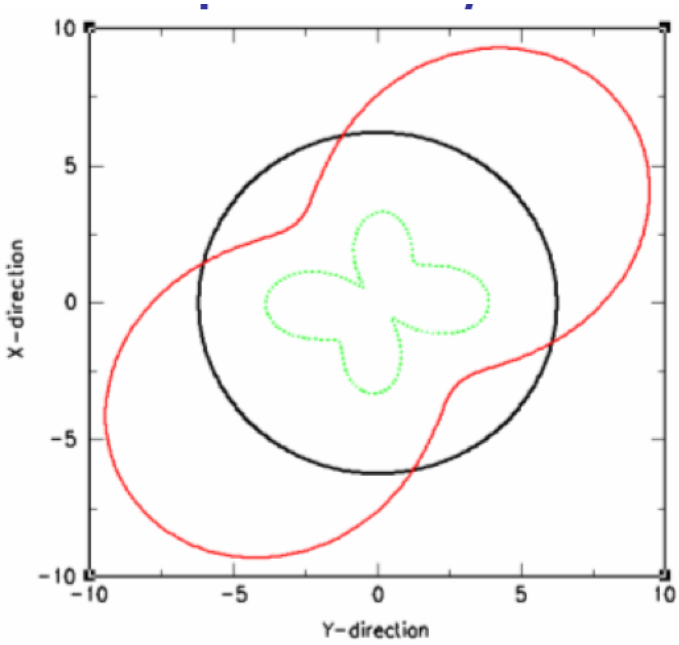

Figure 98: Rotation of an MT tensor at one frequency showing |Zxy| in red and |Zxx| in green. Black is a unit circle.

17.2. Strike directions: Conclusions

- The region generally has a strike direction of around E-W for most sites at most frequencies.
- However, the sites express some lateral heterogeneity in strike directions, with a region in the SW (Anomaly A) preferring a direction of 105° and sites on the eastern two profiles (Anomaly B) preferring around 60°-65°.
- For the purposes of 2-D inversions, the data have been distortion-decomposed with an adopted strike of E-W with an error floor of 3.5% in |Z|.
- This error floor must be used in the 2-D inversions to be consistent with this strike analysis.
- Data at all frequencies have been fit to a distortion model of E-W.

18. Correction for local data anisotropy

The final distortion correction that can be applied is for local data anisotropy, whereby the high frequency asymptotes of the two apparent resistivity curves are moved to their geometric mean values at each site. This is performed on the “dcmp” files output by the proprietary *strike* code using another proprietary code *dcmp2j*.

An example is for site MT1135. On the left in Figure 99 is a plot of the data output from the strike code. On the right is a plot of the data output from the dcmp2j code taking anisotropy of 0.514 into account. The two RhoA curves have been coalesced at their highest four frequencies.

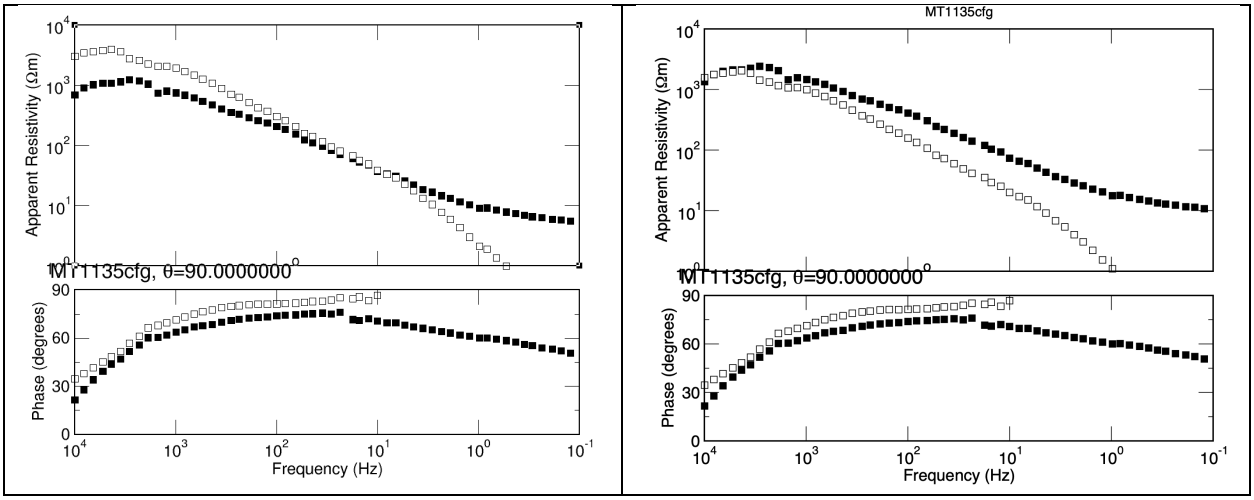

Figure 99: Example of application of anisotropy correction for site MT1135. Left: Output from "strike" code. Right: Output from "dcmp2j" code correcting for RhoA anisotropy of 0.514.

➔ The median shift for all 168 sites is 0.48, which is close to a factor of 1/2.

This is exactly the RhoXY/RhoYX separation seen at all sites and may be due to an error in the recorded layout of the E-W electrode line, a gain-setting issue, or another acquisition-side cause. The histogram of the shift factors is shown in Figure 100, and the clear peak at 0.5 is obvious. The root cause of this shift is unknown, and explanations proffered in this report are speculative in nature and should not be read as definitive.

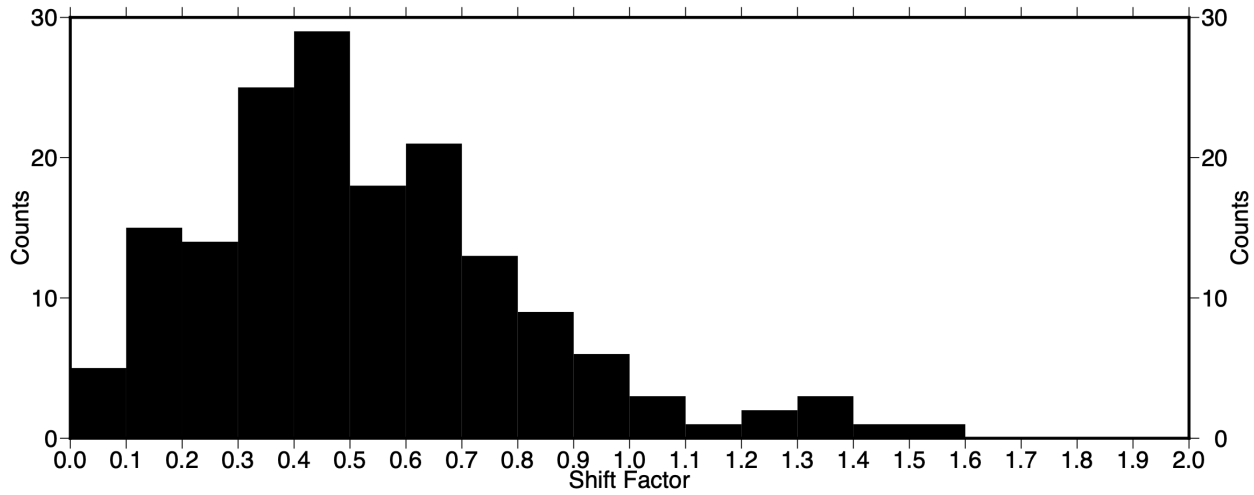

Figure 100: Histogram of the coalescing shift factors to bring the decomposed RhoXY and RhoYX data together for the first 4 frequency points.

19. Rho$^+$ consistency check

The final step is to ensure internal consistency of the RhoA and Pha curves.

Formally in 1-D [*Weidelt*, 1972] and for the TM mode in 2-D [*Weidelt and Kaikkonen*, 1994] the MT responses at a site must be internally consistent such that the apparent resistivity RhoA curve and the phase Pha curve are the Hilbert Transform of each other. There are also a number of other constraints on the nature of the impedances when expressed as impulse response functions in the time domain, but these are rarely exploited [*Jones*, 1980].

For extreme numerical models this is not upheld in the TE mode in 2D [*Parker*, 2010], but experience shows that there are few 2-D TE data for which this Hilbert Transformation relationship is not valid. It also has some merit in 3-D for testing internal compatibility the off-diagonal terms (Zxy and Zyx), but the diagonal terms (Zxx and Zyy) cannot be tested in the same manner as they are routinely "out-of-quadrant".

Parker and Booker [1996] present an algorithm, called *Rho$^+$*, which tests this compatibility between the RhoA and Pha curves. This is an extension of a previous algorithm, called *D$^+$*, of *Parker* [1980] that yields the best-fitting model possible to a 1-D MT response but operated on the real and imaginary parts of the impedances [(6)].

I have adapted the *Rho$^+$* algorithm and made it robust to outliers, that would otherwise perturb the results, using a Least Trimmed Squares approach [*P.J. Rousseeuw and Leroy*, 1987]. This iterative procedure identifies those points that are inconsistent, to within statistical error, of the Hilbert Transform relationship between the RhoA and Pha curves. The outliers are replaced by their predictions, and errors are assigned to signify the magnitude of the shift involved.

For the example of site MT1136, the data after distortion decomposition in Figure 101 (left plot), and clearly even after distortion decomposition there are problems with scatter in the AMT deadband at 5 kHz – 1 kHz. The Robust Rho$^+$ algorithm smoothed through the obvious scatter in the data, as shown in the right plot.

This is an important pre-processing step prior to inversion, as otherwise all least-squares based inversion codes will try to reduce the misfit to the largest outliers, if they are not culled before

[6] Note: All physically realizable systems do not respond before input is received. This means that the impulse response function describing the system must be zero for lags less than zero. This leads to a Hilbert Transformation relationship between the real and imaginary parts of the frequency domain response function. This was used by *Jones* [1980]. For some special systems, called "minimum phase" systems, then the amplitude and phase also form a Hilbert Transform pair.

initiation of inversion. It is important to ensure that RhoA and Pha are consistent, and that outliers are dealt with prior to inversion, or a lot of human and computer time will be wasted.

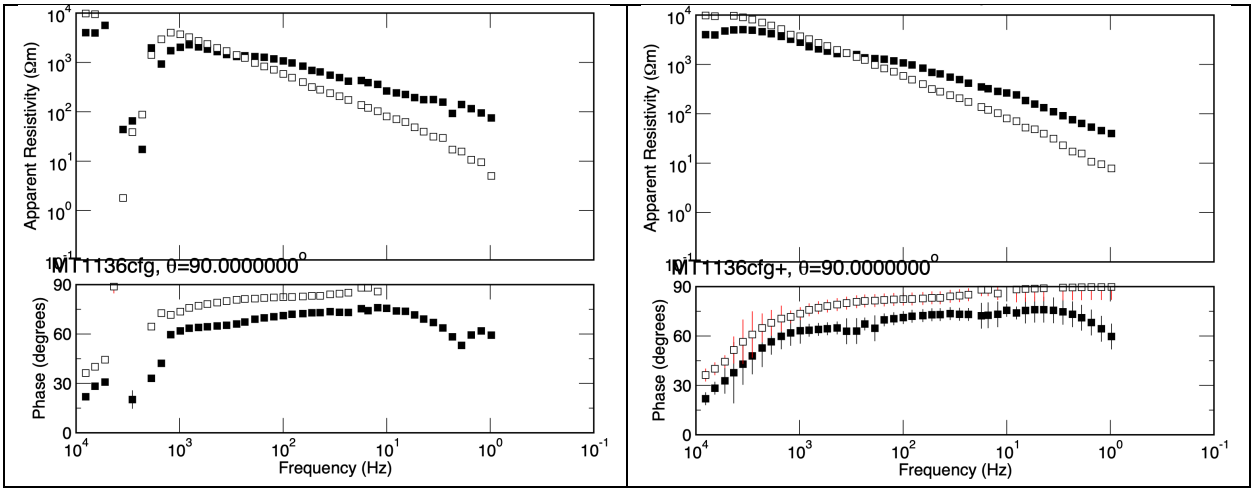

Figure 101: Site MT1136: Left plot are the distortion decomposed data (red symbols). Right plot: Rho+ corrected data. Solid symbols are XY and open symbols are YX.

Decomposition and Rho$^+$ does not necessarily result in 2-D responses that should be inverted for structure. In some cases one of the phases rolls out-of-quadrant (PROQ – phase roll out of quadrant) and the apparent resistivity curves rise or drop at >45°. Such behaviour is impossible in the TM mode in 2-D, and is only seen in the TE mode for extremely pathological and sharp structures, such as the corner of an ocean basin [*Ichihara and Mogi*, 2009], and even then the departure from the correct phase quadrant for the TE phase is less than 10°.

An example is shown for site MT1137, where the original data (not shown) and the decomposed data both exhibit phases rolling out-of-quadrant at frequencies <10 Hz (Figure 102, left). Applying the robust Rho$^+$ forces the PhaXY to stay within quadrant (Figure 102, right), but one cannot have total confidence in the YX responses below 10 Hz as the shapes of the curves have been dramatically modified. In this case the suspect data are culled prior to inversion.

To guard against this issue, visual inspection of the comparisons of before-and-after application of robust Rho$^+$ is performed for all sites prior to inversion, and suspect/inconsistent data are culled.

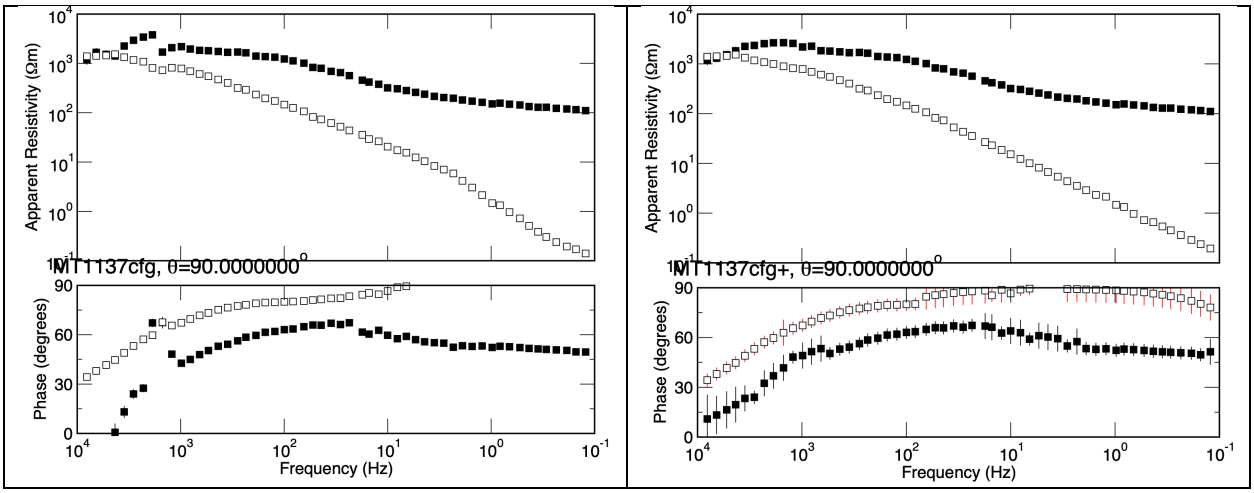

Figure 102: Site MT1137: Left plot are the distortion decomposed data (red symbols). Right plot: Rho+ corrected data. Solid symbols are XY and open symbols are YX. Note the PROQ effect for the YX component in the decomposed (and original) data.

20. Conclusions

20.1. Data Issues

There are a number of data issues highlighted in this report. One of them is that the delivered error estimates appear to underestimate the true uncertainty. Quality Factor analysis suggests a level of order 3.5% in |Z|, which is 7.14% in RhoA and 2° in Pha, is appropriate for this dataset. A second factor affecting low-frequency data quality is possibly the use of metal-plate electrodes, which may contribute additional noise at frequencies below 10 Hz due to polarization charges.

However, for these data from Raglan Zones 2-3 there are three observations of significance:

1) The mismatch between the high frequency (HF) and low frequency (LF) data at many sites is most consistent with effects in the magnetic channels. Based on the analyses presented in this report, the data are not consistent with a rotation-only mechanism. The root cause has not been conclusively identified despite extensive testing.
   ➔ A method was developed to optimally match the LF data with the HF data.

2) Significant differences are observed between the Original and Repeat occupations at the ten sites for which two EDI files are available. Simulation indicates that the observed differences can be reproduced by misalignment of multiple sensors, which is consistent with the contractor's description of the difficult magnetic-rock conditions. Some of the apparent misalignment is consistent with the electric channels, which would in turn be consistent with the electrodes having been deployed in slightly different positions for the two occupations.

➔ The better recording of the two was taken further.

3) There is a systematic difference in the original data between the high frequency asymptotes of RhoXY (with "X" pointing N) and RhoYX of close to a factor of 4. This pattern is unlikely to be an earth response over the spatial extent of the survey. Several non-exclusive mechanisms are consistent with the observation, including a discrepancy between the recorded and deployed Ey length, an unrecorded factor-of-two difference in e-field gain, or another acquisition-side effect. The data examined here do not allow these alternatives to be distinguished, and MTGS makes no finding as to which (if any) is in fact the cause.
   ➔ This was corrected during the *dcmp2j* phase. The "problem" is that now the curves may all be systematically underestimated by a factor of 2.
   ➔ This represents a meaningful interpretive uncertainty: model features found during inversion may be shallower (by a factor of $1/\sqrt{2} \approx 0.707$) than their true depths.

20.2. Dimensionality analysis

The exhaustive dimensionality analysis using the *strike* code revealed that generally the data have a strike of E-W, but there are two regions that depart significantly from that. To the SW is a region labelled Anomaly A with a strike around 105°, and to the E and SE is a region labelled Anomaly B with a strike around 60°-65°.

However, almost all sites will accept a strike direction of E-W with an adopted error floor of 3.5% in |Z|.

21. Quantec's feedback

Quantec Geoscience Ltd. was provided a draft copy of this report on 29th April, 2026 for technical comment prior to release. Roger Sharpe of Quantec provided the following feedback, recorded in full here with Quantec's permission.

On 07/05/2026 16:56, Roger Sharpe wrote:

Hello Alan,

Thank you for the opportunity to review these data prior to further publication and use.

We suggest there are other public domain data at Raglan that may be easier to use. For example, there is a 2018 survey that followed the 2017 survey where many of the complications encountered during the 2017 survey were substantially resolved. The 2018 survey focussed on Raglan Zones Esker and 58 and are available here:

https://protect.checkpoint.com/v2/r03/___https://gq.mines.gouv.qc.ca/documents/EXAMINE/GM71345/lienRapportMern.html___.YzFjOnF1YW50ZWNnZW9zY2llbmNlOmM6bzowZWFkODBlZGI1NDA5M2M4MGMwNmVlOTk5OTUyOTRjODo3OjRmOTM6NTA5MjM0YTRkMjI4MjU3MWQ3OTNhMDYyMWZmOTQxYWNkZWExMzNjZDk5ZDIxMWQzMWQxMzVkNmEyNjljN2YwZjp0OlQ6Rg

In 2017 we encountered these issues, most of which you have described in your report:

7. Winter conditions during the late September / early October survey period
8. Frozen ground
9. High impedance geomorphology
10. Difficulty with navigation and alignment due to proximity to the north magnetic pole
11. Significant and unexpected environmental noise
12. Deadband and signal issues due to daytime measurement

These problems were discussed with the client at the time with these results:

1. The daytime sites were acquired because the client requested as much data as possible in the survey window which was already skewed into winter conditions and very short.
2. The client requested we flag our electrode and coil locations so they could follow with a DGPS survey.

The first result is we reprocessed everything again once we had the DGPS survey.

1. Despite that dipole deployment errors were relatively modest (usually much less than the 15 degrees suggested in your report), the MT results improved, sometimes significantly, with the more accurate DGPS locations
2. But, the band-shift was not entirely mitigated
3. The public domain data on the Quebec website (and so presumably the data you have been reviewing) are the DGPS corrected data (we have confirmed the website data).

During the 2018 survey the following adjustments were made:

1. The survey period was skewed summer conditions in July and August.
2. The shallow part of the near surface was not frozen
3. Contact impedances were improved but having the shallow part thawed was more important
4. We used a tool called DeviSight to align the coils and direct the e-line deployment
5. The measurement noise was presumably better managed due to we were expecting it.
6. Prior to the work, we repeated 3 sites from the 2017 survey with a result of no band-shift.

So, we suggest that using the later survey for a workshop-oriented modeling exercise may be less fraught with unanswerable questions.

If the plan remains to use the 2017 data, then please remove comments about unknown dipole deployments because in fact the DGPS survey provided very accurate dipole end-points.

Regarding the manipulations to these data. We find your process very well-documented. And we recognize that inversion cannot handle the raw data without some type of mitigation. But:

1. It remains our suggestion to use the HF data only (10 kHz to 5 Hz)
    1. Alternatively, our edits are included in the Rho/Phase blocks of the impedance EDI that you have from Glencore. *However if you read an 'edited' (impedance) EDI (i.e. with edits on Rho\Phs) in CGG Geotools, then the user will see the edits as soundings … user can reverse to raw by {un-mask-ALL}.*
    2. *i.e., Geotools reads first [raw Z], then applies masking using the [RhoApp] and [Phase] block data.*
2. Regarding whether we support the manipulations we would discourage such. We can say we have on some occasions, a decade or more ago, experimented with such ad hoc manipulations (mostly associated with static-shift type corrections) but in any recent times prefer judicious editing. As contractors, we cannot manipulate the data like this.
3. Whether to deliver that way has to be your choice only, please. If the end-users understand and prefer or believe in the manipulated result then that has to be their own choice and we are glad they will realize (due to the extensive documentation) what has been done to massage the data.

For this area, we have a list of factors that should be considered by any practitioner operating in this environment:

1. Proximity to the source field may affect the MT plane wave assumption
2. There will be navigation and alignment difficulties due to proximity to pole
3. Frozen ground is a separate issue from high impedance geomorphology
4. High impedance shallow geomorphology (broken shallow outcrop and little to no soil) will be encountered nearly everywhere
5. There is significant mine or environmental noise
6. The deep geology is conductive and LF signal levels are low

Regarding some other comments in the review:

1. There is a table in the logistics report showing a list of which coils were associated with every site
2. There is usually a list of events included in the processing notes and from this, start/end acquisition times could be derived
3. Our new processing provides both these parameters and more within the EDI.

Thank you and best regards,

Roger

Roger Sharpe

VP Technical
Quantec Geoscience
144 Sparks Ave
Toronto ON M2H 2S4
CANADA

22. Limitations and Reliance

This report is based on data provided by the client and feedback from Quantec Geoscience Ltd. MTGS has not independently verified field acquisition procedures or equipment calibration.

The analysis represents a professional interpretation of the available data at the time of writing. Alternative interpretations may exist.

This report:

- Does not assess contractual compliance.
- Does not assign fault or liability to any party.
- Should not be used as the sole basis for operational or financial decisions without consideration of additional data.
- This report is provided for information purposes. ManoTick GeoSolutions Ltd. accepts no liability for any decisions made by parties relying on this report. No third party may rely on this report without written consent.
- **Scope.** This report is an analytical opinion on a dataset supplied to MTGS by the client. It is not an audit of the contractor's field acquisition, equipment calibration, processing software, or contractual performance, and it should not be read as such.
- **Opinion, not finding of fact.** Where this report ascribes observed data features to a particular cause or mechanism, those statements are opinions of MTGS based on the limited information available. They are not findings of fact and should not be relied upon as such by any party.
- **No allegation of fault.** MTGS makes no allegation of professional fault, negligence, or breach of contract by the contractor or any of its personnel. References in this report to possible mechanisms for observed data features are exploratory and intended only to support technical interpretation of the dataset.

- **Pre-release review.** A draft of this report was provided to Quantec Geoscience Ltd. on 29th April, 2026 for technical comment prior to release. Comments from Quantec Geoscience Ltd. were taken into account during revision.
- **Third-party reliance.** No party other than the client is entitled to rely on this report. MTGS expressly disclaims any duty of care to any party other than the client and any liability to any third party arising from the use of this report.
- **Limitation of liability.** To the maximum extent permitted by law, MTGS's aggregate liability arising from or in connection with this report is limited to the fees paid to MTGS for the engagement under which this report was prepared.
- **Governing law.** This report and any dispute arising from or in connection with it are governed by the laws of the Province of Ontario and the federal laws of Canada applicable therein. The courts of Ontario have exclusive jurisdiction.

23. References

Caldwell, T. G., H. M. Bibby, and C. Brown (2004), The magnetotelluric phase tensor, *Geophysical Journal International*, *158*(2), 457-469.

Chave, A. D., and A. G. Jones (1997), Electric and magnetic field galvanic distortion decomposition of BC87 data, *Journal of Geomagnetism and Geoelectricity*, *49*(6), 767-789.

Evans, S., A. G. Jones, J. Spratt, and J. Katsube (2005), Central Baffin electromagnetic experiment (CBEX): Mapping the North American Central Plains (NACP) conductivity anomaly in the Canadian arctic, *Physics of the Earth and Planetary Interiors*, *150*(1-3), 107-122.

Fasano, G., and R. Vio (1988), Fitting a straight line with errors on both coordinates, *Newsletter of Working Group for Modern Astronomical Methodology*, *7*, 2-7.

Garcia, X., and A. G. Jones (2002), Atmospheric sources for audio-magnetotelluric (AMT) sounding, *Geophysics*, *67*(2), 448-458.

Groom, R. W., and R. C. Bailey (1989), Decomposition of magnetotelluric impedance tensors in the presence of local three dimensional galvanic distortion, *Journal of Geophysical Research*, *94*, 1913-1925.

Groom, R. W., and R. C. Bailey (1991), Analytical investigations of the effects of near surface three dimensional galvanic scatterers on MT tensor decomposition, *Geophysics*, *56*(4), 496-518.

Hutton, V. R. S., and A. G. Jones (1980), Magnetovariational and magnetotelluric investigations in S. Scotland., in *Electromagnetic Induction in the Earth and Moon*, edited by U. Schmucker, pp. 141-150, Centr. Acad. Publ. Japan, Tokio and D. Reidel Publ. Co., Dordrecht.

Ichihara, H., and T. Mogi (2009), A realistic 3-D resistivity model explaining anomalous large magnetotelluric phases: the L-shaped conductor model, *Geophysical Journal International*, *179*(1), 14-17, doi:10.1111/j.1365-246X.2009.04310.x.

Jones, A. G. (1980), Geomagnetic induction studies in Scandinavia - I. Determination of the inductive response function from the magnetometer data, *Journal of Geophysics (Zeitschrift fuer Geophysik)*, *48*, 181-194.

Jones, A. G. (1983), On the equivalence of the Niblett and Bostick transformations in the magnetotelluric method, *Journal of Geophysics-Zeitschrift Fur Geophysik*, *53*(1), 72-73.

Jones, A. G. (2012), Distortion of magnetotelluric data: its identification and removal, in *The Magnetotelluric Method: Theory and Practice*, edited by A. D. Chave and A. G. Jones, Cambridge University Press, Cambridge (UK).

McNeice, G. W., and A. G. Jones (2001), Multisite, multifrequency tensor decomposition of magnetotelluric data, *Geophysics*, *66*(1), 158-173.

Parker, R. L. (1980), The inverse problem of electromagnetic induction: Existence and construction of solutions based on incomplete data, *Journal of Geophysics*, *85*(B8), 4421-4428.

Parker, R. L. (2010), Can a 2-D MT frequency response always be interpreted as a 1-D response?, *Geophysical Journal International*, *181*(1), 269-274, doi:10.1111/j.1365-246X.2010.04512.x.

Parker, R. L., and J. R. Booker (1996), Optimal one-dimensional inversion and bounding of magnetotelluric apparent resistivity and phase measurements, *Physics of the Earth and Planetary Interiors*, *98*(3-4), 269-282, doi:10.1016/s0031-9201(96)03191-3.

Rousseeuw, P. J. (1984), Least median of squares regression, *Journal of the American Statistical Association*, *79*(388), 871-880, doi:10.2307/2288718.

Rousseeuw, P. J., and A. M. Leroy (1987), *Robust Regression and Outlier Detection*, 335 pp., Wiley, doi:10.1002/0471725382.

Weidelt, P. (1972), The inverse problem of geomagnetic induction, *Geophysical Journal of the Royal Astronomical Society*, *35*(1-3), 379-379.

Weidelt, P., and P. Kaikkonen (1994), Local 1-D interpretation of magnetotelluric B-polarization impedances, *Geophysical Journal International*, *117*(3), 733-748.

York, D. (1966), Least-squares fitting of a straight line, *Canadian Journal of Physics*, *44*(5), 1079-1086.

York, D. (1969), Least squares fitting of a straight line with correlated errors, *Earth and Planetary Science Letters*, *5*, 320-324.